NUREG/CR-0855
PNL-3040-1
R 1,3,4,5

REACTOR SAFETY RESEARCH PROGRAMS

Quarterly Report
January 1 - March 31, 1979

Pacific Northwest Laboratory

Prepared for
U.S. Nuclear Regulatory Commission

NOTICE

PACIFIC NORTHWEST LABORATORY
operated by
BATTELLE
for the
UNITED STATES DEPARTMENT OF ENERGY
Under Contract EY-76-C-06-1830

Printed in the United States of America
Available from
National Technical Information Service
United States Department of Commerce
5285 Port Royal Road
Springfield, Virginia 22151
Price: Printed Copy $____*; Microfiche $3.00

*Pages	NTIS Selling Price
001-025	$4.00
026-050	$4.50
051-075	$5.25
076-100	$6.00
101-125	$6.50
126-150	$7.25
151-175	$8.00
176-200	$9.00
201-225	$9.25
226-250	$9.50
251-275	$10.75
276-300	$11.00

NUREG/CR-0855
PNL-3040-1
R 1,3,4,5

REACTOR SAFETY RESEARCH PROGRAMS

Quarterly Report
January 1 - March 31, 1979

Compiled and Edited by
J. L. Hooper

Manuscript Completed: April 1979
Date Published: May 1979

Pacific Northwest Laboratory
Richland, Washington 99352

Prepared for
Division of Reactor Safety Research
U.S. Nuclear Regulatory Commission
Under Contract No. EY-76-C-06-1830

FOREWORD

This document summarizes the work performed by Pacific Northwest Laboratory from January through March 1979, for the division of Reactor Safety Research within the Nuclear Regulatory Commission. Each program is considered separately and is discussed according to major tasks or topics, depending on the nature of the project.

CONTENTS

ULTIMATE HEAT SINK PERFORMANCE MEASUREMENTS*

R. K. Hadlock, Project Manager

SUMMARY

Efforts are being directed toward proceeding with cooling pond measurements and initiating spray pond measurements at the Raft River Geothermal Site. Some of this effort is involved with resolution of the discrepancy between available program funding and EG&G, Idaho estimated costs for the upgrading and installation of necessary facilities.

INTRODUCTION

Presently defined scope of the Ultimate Heat Sink Program at Pacific Northwest Laboratory (PNL) includes continuation of cooling pond measurements, initiation of spray pond measurements, completion of both measurement modes, and formulation of data volumes and suggestions for model improvements. The availability of genuinely hot water and control and the ability to survey experimental facilities at Raft River provide opportunity to obtain the data requisite to understanding and model improvement. This opportunity has not been found elsewhere. The cooling pond measurements have proceeded since 1977 and further measurements are required for worst-case conditions, i.e., worst-case combinations of meteorological influences that inhibit heat transfer from the pond to its surroundings. Complementary spray pond measurements are of primary importance, and it is especially appropriate that they be conducted at the same site and integrated with the cooling pond measurements.

The procurement and installation of a spray system at the geothermal site is necessary to obtain the required complementary and integrated data. It has recently been determined that cost estimates for such a facility substantially exceed available programmatic funding. This situation is being resolved by

---

*RSR Fin. Budget No: B2081-8; RSR Contact: R. F. Abbey, Jr.

the NRC and PNL in order to permit continued measurements on the geothermal pond--an analog to Ultimate Heat Sinks of Emergency Core Cooling Systems.

TECHNICAL PROGRESS

Several tasks have been accomplished during the past quarter which provide progress toward defined goals:

1. Results from the 1977 measurement episodes were presented in a paper delivered at the American Meteorological Society Fourth Symposium on Turbulence, Diffusion, and Air Pollution in Reno, Nevada, January 1979. Additionally, preliminary results from the 1978 measurements on the sealed pond were presented.

2 As a result of increasing program visibility, inquiries have been received from other interested organizations. Information has been provided to the Massachusetts Institute of Technology and to the Electric Power Research Institute in response to their interest in evaporation from a sealed thermally hot pond.

3. The Principal Investigator visited the NRC and provided a seminar presentation on results to date. In addition, attention was initiated toward resolution of the discrepancy between available funding and estimated cost of spray system procurement and installation.

4. Preliminary analyses have been accomplished for the 1978 data obtained from the sealed cooling pond. These will form part of the data base and analyses for final reporting; more data, it is determined, are required for conditions of worst-case combinations of meteorological influences. Preparations are complete for anticipated resumption of the cooling pond measurements with the exception of repair work to the pond. Definition of instrumentation requirements for spray measurements has been accomplished. Some preliminary consideration of modeling requirements has been completed.

FUTURE PLANS

Much is contingent on resolution of the discrepancy between the EG&G, Idaho-proposed costs for necessary work at the Raft River site and the funding currently available. Presently available funding would enable completion of the cooling pond effort but none of the spray pond effort described in the program brief.

EXPERIMENTAL VERIFICATION OF STEADY STATE CODES: TASK A - IRRADIATION RESULTS*

C. R. Hann, Program Manager
D. D. Lanning, Project Manager
E. R. Bradley
M. E. Cunningham
R. E. Williford

SUMMARY

Two heavily instrumented six-rod assemblies, IFA-431 and IFA-432, have been irradiated at Halden, Norway. A third assembly, IFA-513, jointly sponsored by the Nuclear Regulatory Commission (NRC) and the Halden Project, began irradiation in late November. This quarter, analysis of IFA-432 and IFA-513 data has proceeded as planned. The work is now divided into four subtasks 1) project management, 2) coordination of irradiation tests, 3) data processing and data reporting, and 4) data analysis. Several Pacific Northwest Laboratory and NRC documents are nearly complete.

INTRODUCTION

The objectives of the Experimental Verification Program are to obtain well-characterized data on fuel temperatures, pellet-clad interaction and gas release on typical light water reactor (LWR) fuel. These data are to be used by NRC to verify steady-state fuel performance computer codes.

Two heavily instrumented six-rod assemblies, IFA-431 and -432, have been irradiated under the program. The rods contain fuel pellets of U.S. boiling water reactor size (BWR) and fuel type with some variations. The variations include: 1) gap size (range to include instantaneous relocation to instantaneous densification), 2) fill gas (a xenon-filled rod was included), and

---

*RSR Fin. Budget No: B2043; RSR Contact: H. H. Scott

3) fuel density type (92% dense pellets with stable and unstable fuel relative to densification). The instrumentation included: fuel centerline thermocouples in each end of each rod, one cobalt and six vanadium neutron detectors, cladding elongation detectors on all six rods, and pressure transducers on three of the six rods.

A third assembly, IFA-513, began irradiation November 1978. The six rods of IFA-513 are each 0.8 m in length versus 0.58 m for IFA-431 and -432. There are thermocouples in each end of each rod and bellows-type pressure transducers and cladding extensometers on each rod. The assembly includes four replicate rods of BWR design (one with pressurized fill gas) and two rods with Xe-He gas mixtures. The latter will provide data at known gas composition on the degradation effect of fission gas on rod thermal performance. Some data on the possibility of gas segregation in a typical fuel rod may also be gained. The replicate rods will provide statistical information on the behavior of identical rods that are operated identically.

The scope of Task A (Irradiation Results) has been to attempt to collate and analyze these data, which are normally taken every 15 min while the reactor is running. The activities related to data reporting and analysis are described below.

SUBTASK A-3 - DATA PROCESSING

Data from the first month of operation for IFA-513 has been received, checked, translated, and plotted in various ways. This applies to data from numerous transient runs as well as the steady-state (TFDR) data. An informal startup data report is in preparation.

In general the startup was successful. The calibration went smoothly and most instrumentation is functioning reliably. Two upper position fuel thermocouples, one cladding elongation detector, and two pressure transducers failed on or before startup.

SUBTASK A-4 - DATA ANALYSIS

Activities of Subtask A-4 have included: 1) estimation of fuel relocation from fuel thermocouple data, 2) analysis of transient data, 3) analysis of fission gas release (pressure transducer) data, 4) analysis of xenon rod data, and 5) error analysis of code calculations.

FUEL RELOCATION ANALYSIS

A draft report of the inferred relocation in IFA-431 and -432 is undergoing internal review. An algorithm (a small collection of computer subroutines) has been written which links the thermal effects of fuel cracking and relocation together with the concommitant mechanical effects on fuel compliance. Our plan is to feed this algorithm measured power and temperature data and match the simultaneous measurement of cladding elongation. The adjusted algorithm will be the primitive "relocation model" that will be used in FRAPCON-2.

Preliminary estimates of fuel relocation in IFA-513 confirm previous conclusions on similar rods in IFA-431 and -432: the relocation is significant, but not complete, at beginning-of-life; and the relocation at the upper location quickly exceeds that at the lower location of thermocouples.

ANALYSIS OF TRANSIENT DATA

The major effort on transient data in the past quarter has dealt with IFA-513. Both the cobalt neutron detector and most of the thermocouples in IFA-432 are beginning to behave erratically, and formal transient data analysis for IFA-432 may cease.

The data from the single beginning-of-life "linear" power decrease for IFA-513 was adequate, and the thermocouple readouts were confirmed within experimental error (±6%) at 95% confidence.

The data from the 20% "step" decreases for IFA-513 have proven to be extremely interesting. Most thermocouples, except for those operated below 1100°C peak, show strong evidence that the fuel cannot shrink upon power

decrease, as simplistic models would presume. The assumption of shinkage affects the feedback calculated between fuel temperatures and gap conductance and has a strong effect on the calculated transient temperatures. It is not unreasonable that cracked outer fuel, once driven outward during power increase by the hotter inner fuel, might not shrink inward very effectively upon power decrease. The data actually point to a thermal strain threshold beyond which the fuel appears incapable of recovering its original dimensions. The validity and implications of these ideas are being explored currently.

ANALYSIS OF XENON ROD DATA

During the past quarter, a draft report was prepared on the life history behavior of the xenon-filled rod (Rod 4) in IFA-431. This report discusses the thermal and mechanical behavior of Rod 4, based on the steady-state and transient temperature data, cladding elongation data, and post-irradiation examination (PIE) data.

Observation and analysis of the data has lead to several conclusions:

- The thermal resistance for the upper fuel region (concentric fuel-cladding geometry) decreased during the irradiation (Figure 1). The equilibrium resistance value corresponds to gap closure and full effective fuel relocation.
- Because of the eccentric fuel-cladding geometry built into the lower region of Rod 4, the thermal resistance for this region remained constant throughout the irradiation (Figure 1).
- Figure 2 shows the in-reactor permanent elongation of Rod 4 compared to two helium-filled rods (of differing initial gap sizes). It has been concluded that the permanent elongation for the helium rods was due only to irradiation growth (Hann and Marshall 1977). Therefore, the additional permanent elongation of Rod 4 was due to fuel-cladding interaction produced by the combined effects of oversize fuel pellets and high fuel temperatures.

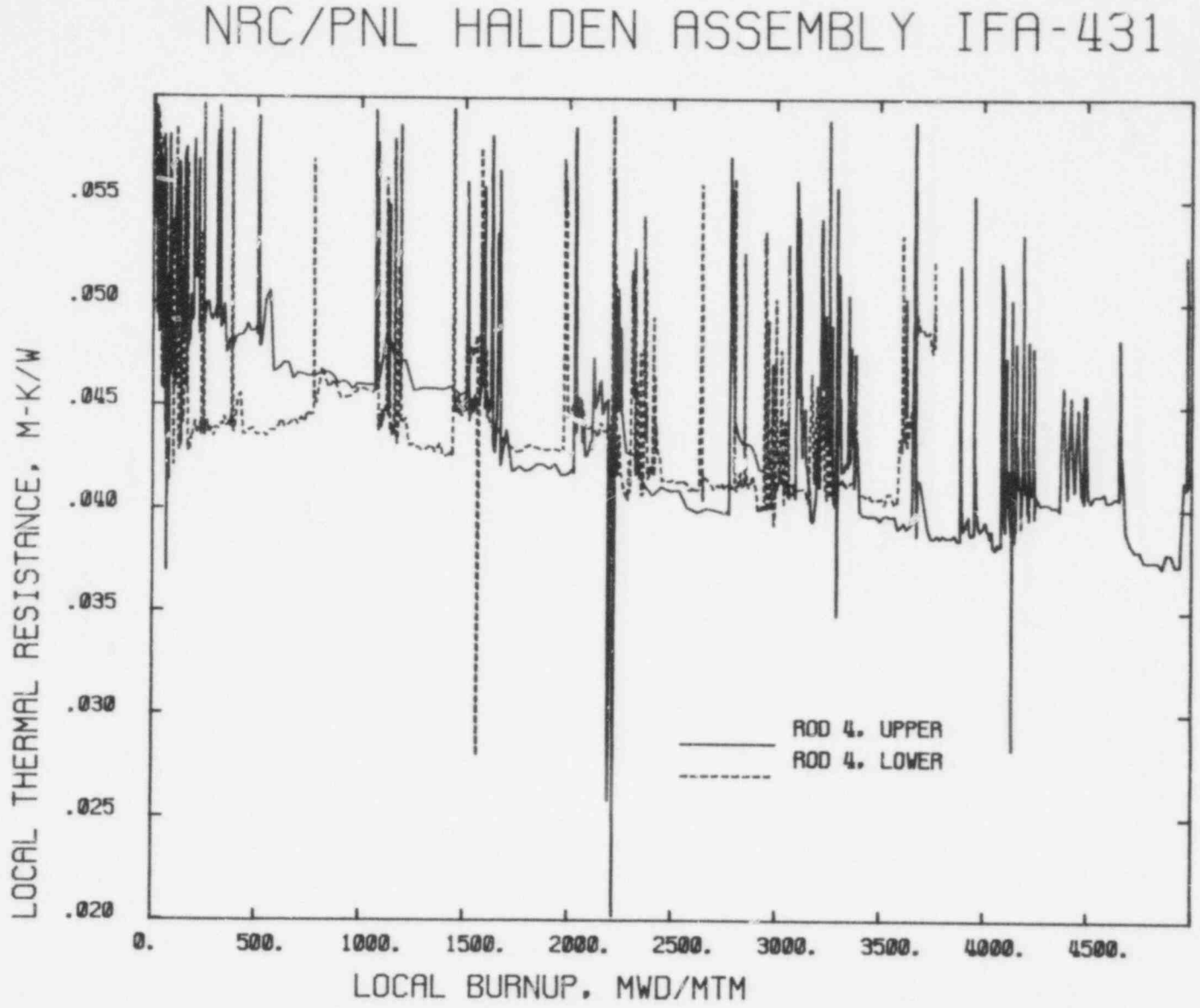

FIGURE 1. Thermal Resistance History of Rod 4, IFA-431

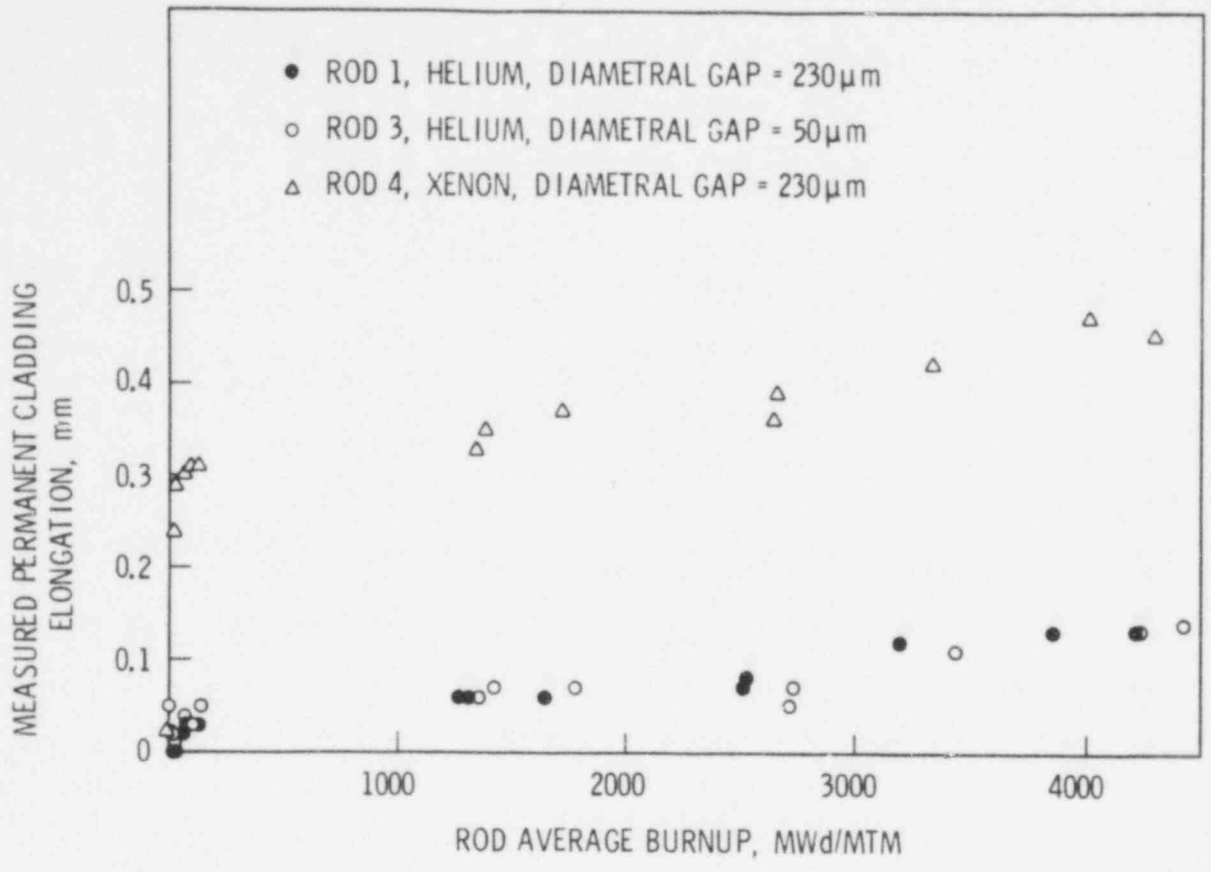

FIGURE 2. Measured In-Reactor Permanent Cladding Elongation for IFA-431

- Thermal simulation of moderate-to-high burnup (>15,000 MWd/MTM) typical BWR rods may be obtained from xenon-filled rods subjected to relatively short irradiations (~3000 MWd/MTM).

ANALYSIS OF FISSION GAS RELEASE DATA

Fission gas release is being deduced from internal fuel rod pressure measurements in three of the six rods from test assembly IFA-432. The measurements are obtained from diaphragm pressure transducers that use a null-balance method for determining the internal pressures. This type of transducer requires manual pressurization which has limited the amount of data available. The pressure transducers in IFA-432 have worked well throughout most of the irradiation period, i.e., December 1975 to present. However,

recent pressure data suggest that the pressure transducer in Rod 6 is not operating correctly.

To obtain data more frequently, bellows-type pressure transducers were used in test assembly IFA-513. This type of pressure transducer allows continuous pressure measurements and the data can be directly related to measurements from the other instrumentation. However, these advantages over the diaphragm-type pressure transducer are partially offset by a loss of sensitivity. The decreased sensitivity is primarily due to an increased free volume in the rods fitted with the bellows-type transducers. The internal free volumes for the fuel rods in IFA-513 are ~8.7 cm^3 as compared to ~4.7 cm^3 for the similarly designed fuel rods in IFA-432. Thus, for the same instrument sensitivity, the change in volume, gas content or temperature that can be detected is almost twice as large for the bellows-type pressure transducers.

The initial pressure data from IFA-513 has been received and examined. Two of the six pressure transducers, Rods 1 and 3, failed early in the first irradiation cycle. The other four pressure transducers appear to be operating correctly, but the absolute pressures that are reported may be in error. The potential error arises because the internal volumes associated with the pressure transducers were not considered in determining the conversion from relative to absolute pressures. However, the differences are expected to be small and can be easily corrected when information regarding the internal volume of the transducers is obtained.

The initial pressure measurements from IFA-513 are currently being evaluated to determine the sensitivity of the bellows-type pressure transducers. The results of these evaluations will be reported at a later date.

ERROR ANALYSIS FOR FUEL THERMAL PERFORMANCE PREDICTIONS

A journal article discussing the analysis of uncertainty for fuel performance codes was written. This article will be submitted to Nuclear Technology.

Work will be resumed next quarter on expanding and improving the uncertainty analysis of fuel thermal performance calculations. One area of particular interest will be an attempt to evaluate the bias between analytical predictions and fuel rod data from well-characterized experiments.

REFERENCES

Hann, C. R., and R. K. Marshall. 1977. Comparative Analysis of Pellet-Cladding Interaction from IFA-431 and IFA-432 Halden Reactor Tests. Tech. Rpt. No. BNWL-2240, Pacific Northwest Laboratory, Richland, Washington.

EXPERIMENTAL VERIFICATION OF STEADY STATE CODES: TASK B - EX-REACTOR DETERMINATION OF GAP AND CONTACT CONDUCTANCE*

C. R. Hann, Program Manager
J. E. Garnier, Project Manager
S. Begej

SUMMARY

Modified Pulse Design (MPD) H_g measurements on an ISM II sample pair under light contact conditions (Dmp $\approx$ 4.2 μm) were initiated. Data has been acquired as a function of pressure to 7 MPa under helium, helium-argon, and argon atmospheres at 293 K. The results conform to anticipated behavior on the basis of decreasing temperature jump distance with increasing gas pressure. However, an anomalous decrease in H_g for helium at gas pressures greater than ~1 MPa is observed.

PROGRAM OBJECTIVES

The objectives of this research program are to provide well-characterized H_g and H_c data to test existing theories for predicting gap and contact heat transfer and to extend measurements of H_g and H_c to higher temperatures and gas pressures than obtained in previous ex-reactor investigations. The determination of the sensitivity of the interface conductance to changes in temperature, gas pressure, gas composition, interfacial contact pressure, gas separation, surface characteristics, and time would allow a further refinement of computer programs such as COMETHE (Roberts, et al. 1978), GAPCON-THERMAL (Beyer, et al. 1975 and GAPCON-THERMAL-3 1978), FRAP-S (Dearien, et al. 1977), and IAMBUS (Wordsworth 1974), which predict the effects of gap and contact conductance in oxide fuel elements.

---

*RSR Fin. Budget No: B2043; RSR Contact: H. H. Scott

STAGE II and III: HIGH GAS PRESSURE STUDY

Data have been obtained on an ISM II sample pair in light contact (Dmp $\approx$ 4.2 μm) in helium, helium:argon (50:50), and argon atmospheres at 283 K at pressures ranging from 0.1 to 7.0 MPa. These results are shown in Figure 1. According to the ideal gap conductance expression

$$H_g = \frac{K_{gas}}{d + g_1 + g_2} \tag{1}$$

where

$$g_{i,2} = \frac{0.2174\ K_{gas}\ \sqrt{TM}}{P}\left(\frac{2-a}{a}\right) \tag{2}$$

H_g will increase with increasing gas pressure (P) due to decrease in the temperature jump distance (g_1 and g_2) until $g_1 + g_2 \ll d$. However the thermal gas conductivity (K_{gas}) will increase with increasing gas pressure due to the very small pressure dependence character of K_{gas}. Therefore, at gas pressures such that $g_1 + g_2 \ll d$ and $H_g \approx K_{gas}/d$, H_g is predicted to increase with increasing gas pressure. The results in Figure 1 conform to this predicted behavior at lower gas pressures, where H_g is seen to increase with increasing gas pressure between 0.1 MPa and 1 MPa in accordance with the decrease in the temperature jump distance. However, at higher gas pressures where $H_g \approx K_{gas}/d$, the gap conductance is seen to decrease with increasing gas pressure for helium but remains essentially constant for the helium:argon and argon gases.

Several accounts of this anomalous behavior with helium are being considered:

1. It is known that adsorption of molecules on a surface will depend on surface temperature and pressure of the gas. As the pressure is increased, additional layers of gas will become weakly bound to the surface. This interface may act as an insulating layer and cause a decrease in the gap conductance even though K_{gas} will increase.

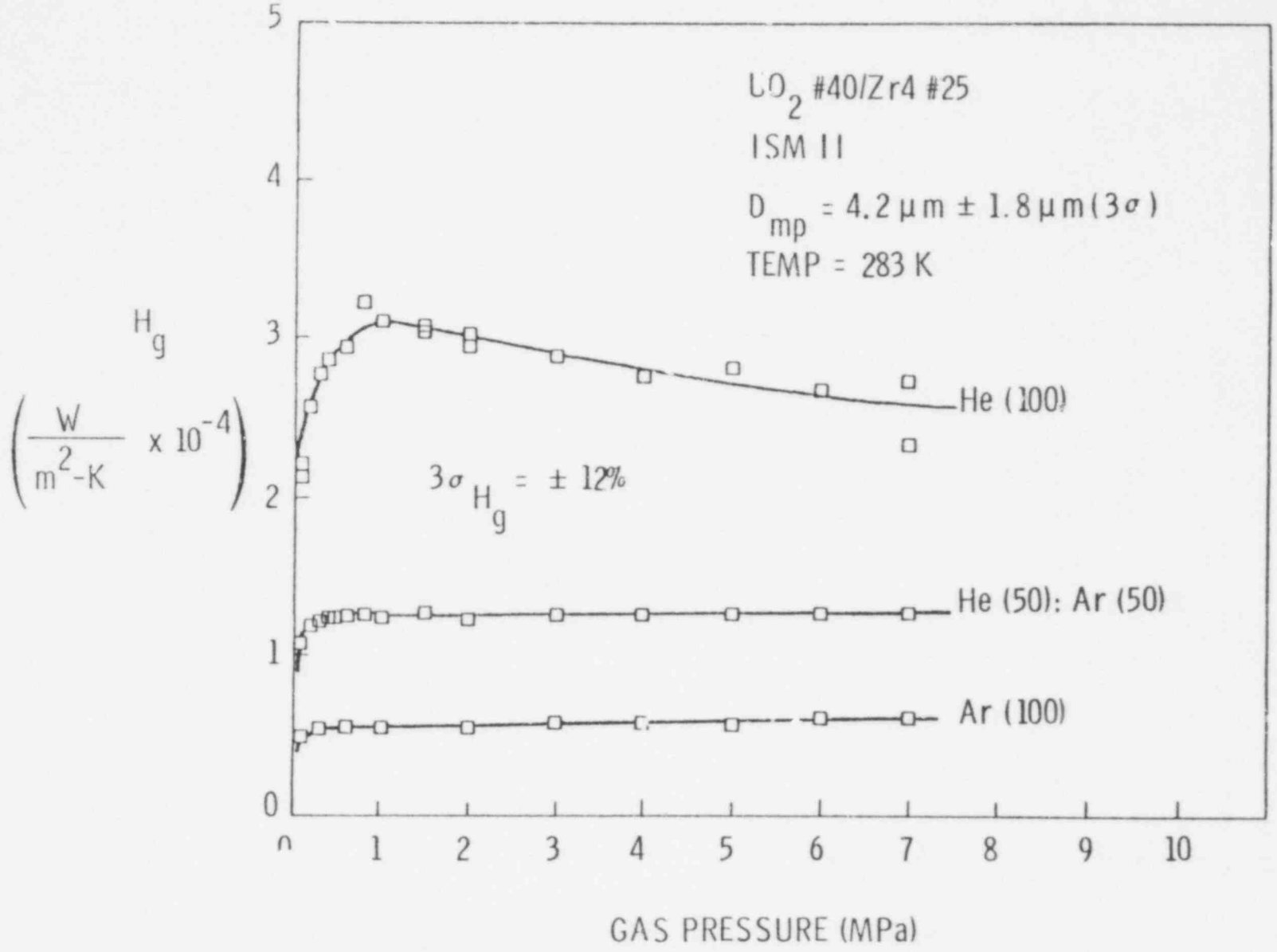

FIGURE 1. H_g Versus Gas Pressure for Helium (100), Helium (50):Argon (50), and Argon (100) at 283 K.

If this effect is real, it would be expected to be more pronounced in an atmosphere of lower thermal resistance (helium) than an atmosphere of high thermal resistance (argon).

2. The anomaly may occur as a result of experimental deviation from the mathematical boundary conditions associated with the analytical model, e.g., the requirement that the time delay of the thermal pulse across the gas interface should be "negligible."

Additional data at high temperatures and larger gap widths will further illuminate the problem regarding the anomalous behavior in helium gas.

Preliminary tests have been conducted at elevated temperatures and reveal that gas convection currents at high temperatures (>473 K) and high gas pressures (>1 MPa) constitute a noise problem due to the direct contact between the currents and the fast response thermocouple on the back of the Zr-4 specimen. The problem is expected to be alleviated by redesign of the specimen sample holder.

FUTURE PLANS

Future plans include acquiring data in the high-pressure gas regime (0.1 to 7.0 MPa) at high temperatures (up to 673 K) and at larger gap separation distances (~15 μm).

REFERENCES

Beyer, C. E., et al. 1975. GAPCON-THERMAL II: A Computer Program for Calculating the Thermal Behavior of an Oxide Fuel Rod. BNWL-1898, Pacific Northwest Laboratory, Richland, Washington.

Dearien, J. A., et al. 1977. FRAP-52: A Computer Code for the Steady State Analysis of Oxide Fuel Rods. TREE-NUREG-1107, U.S. Nuclear Regulatory Commission, Washington, D.C.

GAPCON-THERMAL-3: Code Description. 1978. PNL-2434, Pacific Northwest Laboratory, Richland, Washington.

Roberts, J. T. A., et al. 1978. Planning Support Document for the EPRI LWR Fuel Performance Program. EPRI-NP-737-SR, Electric Power Research Institute, Palo Alto, California.

Wordsworth, J. 1974. "IAMBUS-1: A Digital Computer Code for the Design, In-Pile Performance Prediction and Postirradiation Analysis of Arbitrary Fuel Rods." Nuclear Science and Engineering 31:309.

EXPERIMENTAL VERIFICATION OF STEADY STATE CODES: TASK C - CODE DEVELOPMENT*

C. R. Hann, Program Manager
C. L. Mohr, Project Manager
W. D. Bennett
M. E. Cunningham
F. E. Panisko
W. N. Rausch
R. E. Williford

SUMMARY

The final version of FRAPCON-1 has been received from Idaho Nuclear Energy Laboratory (INEL). This version is operational at PNL and is being used in developing FRAPCON-2. The interface requirements between INEL models and PNL models being developed for FRAPCON-2 have been worked out jointly between the two laboratories. The mechanical analysis package PELET has been placed in FRAPCON and is operational in the code. Conceptual development work is continuing on a relocation model that ties the thermal, mechanical and material behavior for the fuel together in a consistent manner.

INTRODUCTION

The code development effort associated with the verification of steady state codes has the overall objective of providing analysis models and techniques for FRAPCON, in cooperation with INEL, that can be used in evaluating the experimental results associated with the program. Three subtasks have been defined that include code coordination with INEL, mechanical model development for FRAPCON, and relocation model development for FRAPCON.

---

*RSR Fin. Budget No: B2043; RSR Contact: H. H. Scott

TECHNICAL PROGRESS

The code coordination effort, which includes activities related to code operation, evaluation and modification has received the major emphasis this period. As a result of this effort on familiarization with FRAPCON, significant progress has been possible in incorporating the PELET mechanical analysis package into the FRAPCON structure.

SUBTASK 1 - CODE COORDINATION

The third version of FRAPCON-1 was received and has been implemented at PNL. This code forms the basis for developing the FRAPCON-2 models and will be expanded by both EG&G and PNL as needed.

The interface requirements between the more important fuel performance models and the code structure were worked out jointly between PNL and EG&G. The configuration that has been defined will allow the user to select the models that are available. The core requirements will be expanded or contracted depending on both mesh size as well as on the models that have been selected.

The ANS 5.4 stable high-temperature gas release model has been implemented in FRAPCON and is currently being evaluated. The development of this model has been funded by the CORE Performance Branch of the Division of Systems Safety.

SUBTASK 2 - MECHANICAL MODELING

The mechanical analysis package PELET has been placed in FRAPCON and is operational in this code. The results have been compared with those from GAPCON-THERMAL-3 (GT3) and are identical for similar input. This comparison of PELET, which was developed for GT3, has shown that the PELET subcode is operating correctly in FRAPCON and that major problems in implementing it have been solved.

SUBTASK 3 - RELOCATION MODEL DEVELOPMENT

The relocation model development is being developed using fuel crack-patterns, Halden test data and fuel compression test data. The crack patterns in the fuel give a basis for evaluating the possible rigid body motions associated with the fuel compliance or compression. The Halden data provide a boundary condition on evaluating the combined thermal and mechanical stack interaction behavior. Ex-reactor tests of fuel stack compliance give a controlled basis for estimating the effects of fuel movement on effective relocation and effective elastic modulus.

The preliminary relocation model that is planned for FRAPCON will be used to relate the incremental fuel elastic compliance and effective fuel thermal conductivity to available void space in the fuel. The model is currently under development.

FUTURE WORK

The major emphasis will be on the continued development of the relocation model and integration of this model into the mechanics analysis subcode PELET in FRAPCON.

GRAPHITE NONDESTRUCTIVE TESTING*

W. C. Morgan, Project Manager

SUMMARY

Preliminary investigations have shown that eddy current measurements of electrical conductivity of graphite are sensitive to the density of oxidized samples.

INTRODUCTION

This is a continuation of previous work which demonstrated the feasibility of monitoring changes in the compressive strength of oxidized graphite by measuring changes in the velocity of an ultrasonic wave propagated through the graphite. The FY-1979 scope of this project is to:

- continue investigation of sonic velocity technique as applied to PGX and ATJ graphites
- investigate potential for other sonic measurements, such as attenuation data, to provide useful information
- investigate potential of other techniques such as eddy current devices for providing interpretable indications of graphite strength.

The objective of this investigation is to demonstrate feasibility of nondestructive testing (NDT) techniques for determination of structural graphite strength.

TECHNICAL PROGRESS

Oxidized samples of Stackpole graphite grade 2020 (a fine-grained, high-strength, isotrophic graphite, which is similar to Union Carbide graphite

---

*RSR Fin. Budget No: B2101-9; RSR Contact: R. D. Schamberger

grade ATJ) have been used to demonstrate that the eddy current measurements of electrical conductivity are sensitive to the density changes produced by oxidation.

General Atomic Co. has been requested to provide a supply of Union Carbide grade PGX graphite (the core support block graphite for the Fort St. Vrain Reactor) for use in our investigations.

FUTURE PLANS

The primary emphasis during the next quarter will be placed on obtaining PGX graphite and preparing samples, both for use as density-conductivity standards for the eddy current work and for oxidation to develop various oxidation-depth profiles for use in the sonic and eddy current investigations.

ACOUSTIC EMISSION-FLAW RELATIONSHIP FOR IN-SERVICE MONITORING OF NUCLEAR PRESSURE VESSELS*

P. H. Hutton, Project Manager
E. B. Schwenk
R. J. Kurtz

SUMMARY

Fatigue load cycle rate effects on acoustic emission (AE) from room temperature fatigue crack growth and AE characteristics of fracture from a surface notch flaw tested at 550°F were investigated using laboratory specimens. Also, pattern recognition has been examined for potential to characterize AE signals or distinguish from noise. Finally, testing of high-temperature AE sensors was continued.

Testing to examine load cycle rate effects on AE during room temperature fatigue crack growth showed no discernable difference between 0.1 and 2.0 Hz. This data suggests that it may be possible to extend a load cycle based AE-fatigue crack growth correlation to a time basis, thus improving the potential for structural flaw monitoring where "load cycles" have less direct meaning.

Detailed computer analysis of AE-fatigue crack growth signal properties from the load cycle rate specimen provided some initial insight into the effects of cycle rate, R-ratio and fatigue crack growth rate upon load position, AE energy, pulse height and peak time. Partitioning of AE signals with respect to position on the cyclic load waveform (i.e., load position) showed that the distribution of AE signals appeared to be independent of changes in cycle rate and R-ratio. In addition, the average AE energy to pulse height ratio was nearly constant over a large range of fatigue crack growth rate indicating that the two parameters appear to be dependent of each other. Furthermore, the percentage of AE count in a given energy range also seems to be

---

*RSR Fin. Budget No: B2088; RSR Contact: J. Muscara

independent of cyclic frequency and R-ratio. Lastly, the average peak time per count showed no consistent trend with respect to cyclic frequency, R-ratio or crack growth rate.

Results from fracture testing at 550°F using a surface notch flaw produced a relationship between AE and crack opening displacement which was similar in form to earlier data obtained from fracture testing 6-in. wall HSST vessels.

Initial investigation of pattern recognition techniques as a method of distinguishing AE signals from similar noise signals showed a correct classification on 95% of the signals in a sample of 223 signals.

High-temperature AE sensor response tests after 5400 hr exposure to 550°F (288°C) showed that one surface mount sensor, in addition to a metal waveguide sensor, continued to have adequate sensitivity and be unaffected by the temperature exposure.

INTRODUCTION

The purpose of this program is to provide an experimental evaluation of the feasibility of detecting and analyzing flaw growth in reactor pressure boundaries on a continuous basis using AE. Type A533B, Class 1 steel is being used in all experimental testing. The objectives of this program are:

- characterize AE from defects under material property conditions recognized as being of primary concern to reactor pressure vessel integrity and characterize acoustic signals from representative innocuous sources
- develop criteria for distinguishing significant flaw AE from innocuous acoustic signals
- develop an AE-flaw damage model to serve as a basis for relating in-service AE to pressure vessel integrity
- make available a characterized high-temperature AE sensor
- develop a continuous surveillance AE data acquisition and analysis system.

Progress relative to these objectives is discussed in the following sections by topics based on the NRC Program Brief. These will include AE/fracture mechanics testing, AE signal characterization, high-temperature AE sensor testing, and reports. The final section will describe the work planned for next quarter.

AE/FRACTURE MECHANICS TESTING

This section describes the experimental procedure used in fatigue crack growth and fracture testing plus a discussion and analysis of the test results.

FATIGUE CRACK GROWTH TEST PROCEDURE

Room temperature (RT) fatigue crack growth (FCG) testing and analysis of a single edge notch (SEN) base metal specimen (1-1A-3B) has been completed. The purpose of the test was to investigate the effect of fatigue cycle rate upon the AE response. Specimen preparations prior to FCG testing consisted of: (1) a stress relief heat treatment at 1150° ± 25°F for 40 hr, (2) removal of any oxide scale by grit blasting, (3) sawing an approximately 0.030-in. wide by 1.1-in. long notch into one edge of the specimen, (4) polishing the specimen surfaces near the notch to facilitate optical crack length measurements, (5) drilling small holes to allow attachment of an LVDT for measuring the crack opening displacement (COD), and (6) mounting and calibrating the AE transducers. The drawing in Figure 1 shows the specimen geometry, notch dimension, and the location of the AE transducers relative to the center-line of the specimen. The AE acceptance zone was restricted to a region about 0.5-in. wide on each side of the notch. The COD gage mounting apparatus was located outside of the acceptance zone. The AE monitoring system's effective sensitivity was about 0.12 μbar (Hutton, et. al 1978c).

Specimen 1-1A-3B was sinusoidally fatigue cycled between fixed maximum and minimum loads at 0.1 and 2.0 Hz cycle rates. The fatigue loading conditions employed are listed in Table 1 along with crack growth data.

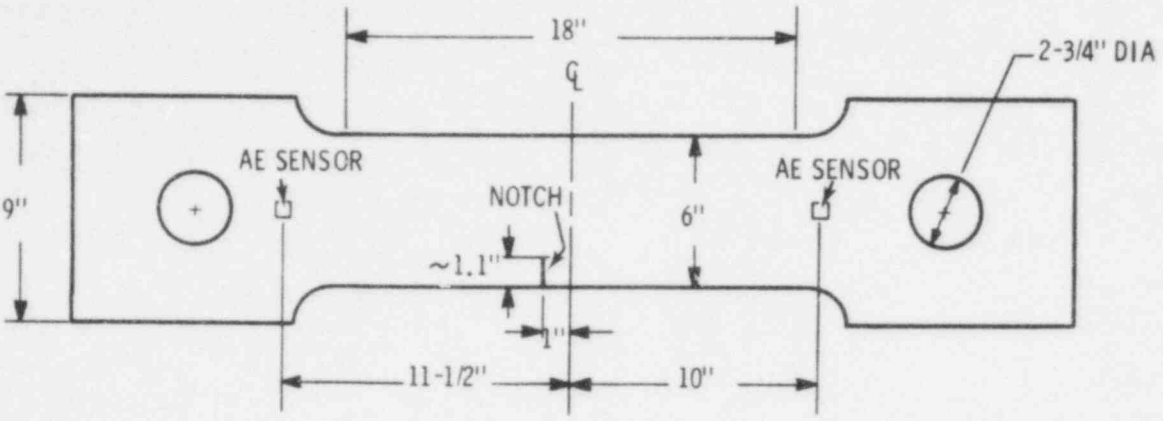

FIGURE 1. Specimen Geometry, Notch Dimensions, and AE Sensor Locations for SEN Specimen 1-1A-3B

FRACTURE TEST PROCEDURE

Elevated temperature (550°F) fracture testing and analysis of a surface notch (SN) base metal specimen (1-2A-4A) was completed during this reporting period. The plate tension specimen shown in Figure 2 was similar to one used in a previous RT-SN fracture test (2-1A-2B) (Hutton, Schwenk, and Kurtz 1978a). Pretest preparations for this specimen were essentially the same as for the above FCG test except that a 0.03-in. thick by 3-in. diameter metal slitting saw was used to machine a part-circular notch into the specimen surface. In addition, four chromel-alumel thermocouples were spot welded to the specimen. There were two thermocouples on each side of the specimen and each thermocouple was located a distance of 3 in. from the notch (see Figure 2). The AE sensors were mounted with a high-temperature adhesive (HYSOL EA 934) and acoustic couplant (PYRO GEL 60). Heat dissipation shields and forced-air cooling of the specimen near the AE sensors were used to protect the sensors from the heat. Room temperature calibration data indicated that the effective sensitivity of the AE monitor system was about 0.1 μbar.

To sharpen the notch root radius prior to fracture testing, the specimen was subjected to fatigue loading. Table 2 lists the fatigue precracking conditions employed. The specimen was fatigue loaded until the surface crack

TABLE 1. Fatigue Loading Conditions for SEN Specimen 1-1A-3B

LOAD, KIPS		CYCLE RATE, Hz	LOAD CYCLE INCREMENT, Δn	CRACK GROWTH INCREMENT, Δa, in.	COMMENTS
MAX	MIN				
80	8	2	15,852	0.0289	Crack initiation
		2	6,117	0.0362	
		2	4,268	0.0269	
		2	4,557	0.0484	
		2	5,060	0.0492	No AE data
		2	5,341	0.0562	
		2	5,180	0.0607	No AE data
		0.1	550	0.0077	No AE data
		0.1	310	0.0029	No AE data
		0.1	4,932	0.0641	
		0.1	3,700	0.0499	
		0.1	3,521	0.0537	
		0.1	3,485	0.0583	
		0.1	3,041	0.0544	
		0.1	3,015	0.0583	
		0.1	2,337	0.0504	
		0.1	2,596	0.0610	
		2	1,814	0.0497	
		2	2,012	0.0542	
		2	2,006	0.0569	
		2	1,820	0.0592	No AE data
		2	1,397	0.0522	
		0.1	947	0.0350	
		0.1	1,178	0.0511	
		0.1	1,030	0.0460	
		0.1	994	0.0486	
		0.1	989	0.0527	

TABLE 1. (Contd)

LOAD, KIPS		CYCLE RATE, Hz	LOAD CYCLE INCREMENT, Δn	CRACK GROWTH INCREMENT, Δa, in.	COMMENTS
MAX	MIN				
80	8	2	875	0.0460	
		2	855	0.0464	
		2	818	0.0550	
		2	901	0.0667	
		2	796	0.0560	
		0.1	684	0.0622	
		2	630	0.0503	Accidental overload to 90 kips prior to this crack growth increment. No AE data
		0.1	595	0.0428	
		0.1	594	0.0412	
		0.1	539	0.0488	
		0.1	585	0.0603	
80	48	2	2,660	0.0562	
		2	2,430	0.0591	
		2	2,375	0.0488	
		2	2,167	0.0640	
		2	2,105	0.0585	
		2	1,994	0.0657	
		2	1,757	0.0624	
		2	1,611	0.0651	
		2	1,384	0.0572	

NOTE: Inital crack length was 1.1440 in.

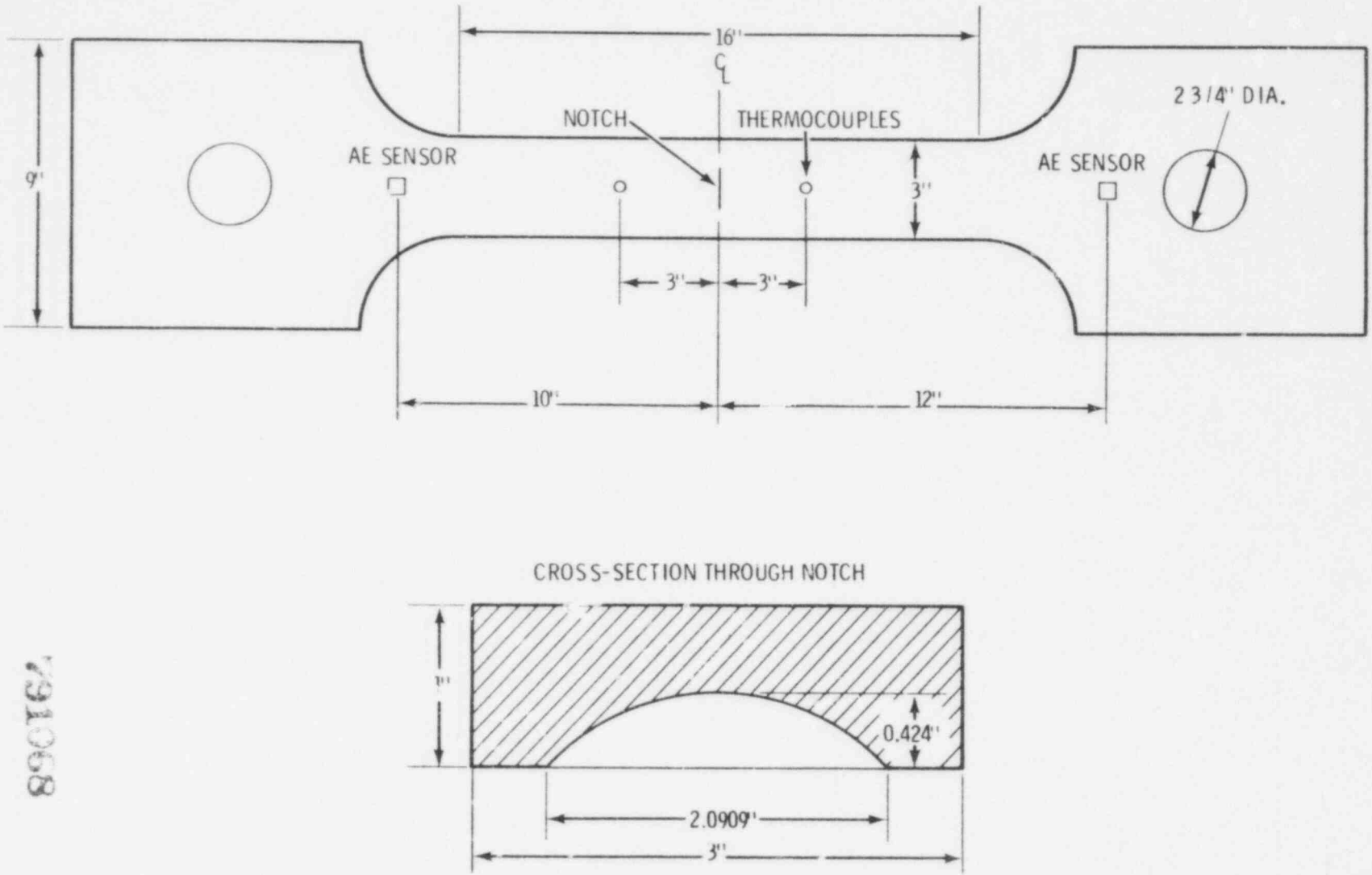

FIGURE 2. Specimen Geometry, Notch Dimensions, and AE Sensor Locations for SN Specimen 1-2A-4A

TABLE 2. Fatigue Loading Conditions for Precracking of Specimen 1-2A-4A

LOAD, KIPS		CYCLE RATE, Hz	LOAD CYCLE INCREMENT, Δn	CRACK GROWTH INCREMENT, (SURFACE) $\Delta 2c$, in.	CRACK GROWTH INCREMENT (THICKNESS) Δa, in.	COMMENTS
MAX	MIN					
80	8	1	15,845	0.0137		
80	8	1	4,675	0.0266	0.121	
NOTE: Initial surface crack length was 2.0909 in. and initial crack depth was 0.424 in.						

791063

length measured 2.1312 in. Following precracking, the specimen was relocated to 440-kip Baldwin tensile test machine for fracture testing. During fracture testing the specimen gage section was radiantly heated, with equal numbers of heat lamps on each side. Pretest temperature distribution measurements indicated that the fraction of the specimen bounded by the AE acceptance zone was at 550° ± 10°F when the thermocouple readings were approximately ')0°F. The fracture test was accomplished by ramping the load at a rate of approximately 12 kips/min until failure of the specimen occurred.

FATIGUE CRACK GROWTH TEST EXPERIMENTAL RESULTS

Condensed experimental results for FCG testing of SEN specimen 1-1A-3B are listed in Tables 1, 3, and 4. The AE data in Table 3 were condensed from digital cassette tapes, which were processed by a computer. The intent was to produce a data set of manageable proportions to facilitate comparisons with previous testing in which the AE data were acquired on digital memories.

A plot of crack length as a function of load cycles is shown in Figure 3. The open squares in Figure 3 represent the average of two crack length measurements made with 32X traveling stage microscopes on opposite sides of the specimen. The points in Figure 3 are calculated values of crack length based upon a semi-empirical relationship between specimen compliance and the crack length/specimen width ratio. Compliance measurements were taken after each crack growth increment by manually ramping the load from zero to the maximum value applied during that crack growth increment. Compliance was

then defined as: $$C(^{in}/lb) = \frac{\delta_{max} - \delta_{min}}{P_{max} - P_{min}} \qquad (1)$$

where δ_{max} and δ_{min} are the maximum and minimum values of the COD, respectively, and P_{max} and P_{min} are the maximum and minimum values of the applied load.

The compliance versus crack length/specimen width data were then fit with a curve estimated using least mean square methods to an equation of the following form:

$$C = \left(\frac{a}{W}\right) \sec \left(\frac{\pi a}{2W}\right) \quad A \sec \left(\frac{\pi a}{2W}\right) - B \qquad (2)$$

TABLE 3. Acoustic Emission Test Data for Room Temperature Fatigue Crack Growth Testing of SEN Specimen 1-1A-3B

LOAD CYCLE INCREMENT	INCREMENTAL AE COUNT DATA								INCREMENTAL AE ENERGY DATA
	VALID COUNT	PEAK TIME - μSEC			SIGNAL AMP. - VOLTS				
		0-3	4-6	>6	<1.15	1.15-2.2	2.2-4.2	>4.2	
15,852	-	-	-	-	-	-	-	-	-
6,117	787	764	6	17	1	171	600	15	51,486
4,268	1,189	911	160	118	7	568	401	213	81,520
4,557	699	513	19	167	25	418	117	139	83,392
5,060	-	-	-	-	-	-	-	-	-
5,341	2,636	1,568	131	937	13	1,241	1,332	50	173,626
5,180	-	-	-	-	-	-	-	-	-
550	-	-	-	-	-	-	-	-	-
310	-	-	-	-	-	-	-	-	-
4,932	5,965	4,215	561	1,189	14	1,300	1,592	3,059	654,890
3,700	4,381	3,119	298	964	39	1,781	1,675	886	302,364
3,521	3,597	2,172	333	1,092	18	1,331	1,528	720	260,878
3,485	3,693	2,149	252	1,292	20	1,369	1,372	932	300,632
3,041	2,450	1,678	294	478	12	1,179	743	516	168,806
3,015	2,309	1,738	133	438	39	621	1,474	175	139,278
2,337	3,679	2,698	192	789	41	1,839	1,156	643	218,712
2,596	5,678	4,702	289	687	73	1,173	1,420	3,012	492,060
1,814	7,257	4,524	621	2,112	38	2,201	1,875	3,143	698,662
2,012	4,321	2,634	391	1,296	26	1,347	2,112	836	315,296
2,006	5,646	3,743	780	1,123	29	2,977	2,774	766	388,834
1,820	-	-	-	-	-	-	-	-	-
1,397	4,587	3,378	253	956	21	1,742	1,857	967	348,972
947	3,448	1,578	282	1,588	9	808	1,868	763	262,808
1,178	3,560	1,717	425	1,418	24	1,366	1,592	578	234,982
1,030	3,092	1,628	318	1,146	14	1,559	1,050	469	195,772
994	4,568	2,478	398	1,692	25	1,732	1,782	1,029	313,176
989	4,301	2,447	380	1,474	13	1,344	1,233	1,711	406,378
875	3,782	2,206	295	1,281	21	1,363	1,322	1,076	345,784

TABLE 3. (Contd)

LOAD CYCLE INCREMENT	INCREMENTAL AE COUNT DATA								INCREMENTAL AE ENERGY DATA
	VALID COUNT	PEAK TIME - μSEC			SIGNAL AMP. - VOLTS				
		0-3	4-6	>6	<1.15	1.15-2.2	2.2-4.2	>4.2	
855	4,685	3,176	220	1,289	39	1,602	1,815	1,229	373,514
818	5,026	3,167	354	1,505	31	1,879	2,060	1,056	427,252
901	4,101	2,273	499	1,369	16	1,299	2,091	735	339,254
796	4,355	2,376	333	1,646	13	1,644	1,857	841	339,480
684	3,506	1,548	323	1,635	11	762	1,231	1,502	460,282
630	-	-	-	-	-	-	-	-	-
595	1,768	694	132	942	3	509	604	652	173,584
594	2,393	1,057	155	1,181	3	736	878	776	253,262
539	2,982	1,323	209	1,450	6	767	1,157	1,052	268,380
585	6,154	2,536	472	3,146	2	1,184	2,069	2,899	679,746
2,660	-	-	-	-	-	-	-	-	-
2,430	1,392	555	181	656	5	448	480	459	138,482
2,315	1,743	753	85	905	6	470	612	655	147,632
2,167	1,032	522	108	402	3	272	387	370	96,748
2,105	1,263	504	125	634	1	301	637	324	107,506
1,994	291	129	27	135	2	67	136	86	23,028
1,757	185	63	5	117	0	46	38	101	28,378
1,611	306	115	20	171	0	92	122	92	24,652
1,384	532	279	41	212	1	44	120	367	96,322

TABLE 4. Crack Opening Displacement Measurements for Fatigue Crack Growth Testing of SEN Specimen 1-1A-3B[a]

CRACK LENGTH, IN.	APPLIED LOAD, KIPS				
	0	20	40	60	80
1.1440	3.100	4.327	5.609	6.906	8.219
1.1729	3.218	4.508	5.907	7.373	8.743
1.2091	3.238	4.577	6.057	7.551	9.040
1.2360	3.243	4.644	6.181	7.721	9.256
1.2844	3.260	4.751	6.380	7.990	9.593
1.3335	3.261	4.854	6.534	8.244	9.925
1.3897	3.258	4.934	6.725	8.540	10.339
1.4504	3.311	5.062	7.012	9.004	10.905
1.4581	3.337	5.145	7.132	9.104	11.053
1.4610	3.310	5.095	7.065	9.026	10.993
1.5251	3.379	5.370	7.487	9.590	11.705
1.5256	3.428	5.356	7.468	9.578	11.692
1.5749	3.421	5.498	7.728	9.999	12.174
1.6286	3.428	5.656	7.991	10.342	12.686
1.6868	3.538	5.830	8.342	10.807	13.273
1.7412	3.566	5.970	8.589	11.219	13.809
1.7995	3.621	6.174	8.971	11.737	14.490
1.8498	3.579	6.300	9.253	12.175	15.048
1.9108	3.653	6.509	9.622	12.718	15.763
1.9108	3.653	6.509	9.622	12.718	15.763
1.9605	3.740	6.680	9.985	13.212	16.419
2.0147	3.765	6.894	10.359	13.799	17.189
2.0715	3.843	7.160	10.825	14.485	18.032
2.1307	3.880	7.394	11.278	15.099	18.888
2.1829	3.987	7.688	11.748	15.762	19.745
		COD GAGE CHANGE			
2.2179	3.017	3.631	4.315	5.002	5.675
2.2690	3.033	3.690	4.407	5.130	5.843

TABLE 4. (Contd)

CRACK LENGTH IN.	APPLIED LOAD, KIPS				
	0	20	40	60	80
2.3150	3.064	3.740	4.492	5.246	6.002
2.3635	3.074	3.800	4.592	5.374	6.167
2.4162	3.099	3.853	4.687	5.514	6.341
2.4622	3.119	3.895	4.756	5.628	6.487
2.5086	3.137	3.962	4.874	5.787	6.701
2.5636	3.156	4.045	5.008	5.971	6.932
2.6303	3.208	4.148	5.164	6.187	7.216
2.6863	3.261	4.247	5.333	6.418	7.506
2.7485	3.309	4.396	5.543	6.701	7.870
2.7485	3.942	5.105	6.282	7.458	8.646
2.7988	3.939	5.114	6.303	7.518	8.736
2.8416	3.944	5.111	6.358	7.630	8.888
2.8828	3.949	5.117	6.433	7.747	9.070
2.9315	3.965	5.160	6.556	7.946	9.370
2.9918	4.032	5.323	6.833	8.335	9.865
3.0480	4.100	5.437	7.012	8.581	10.230
3.1071	4.200	5.631	7.297	8.962	10.712
3.1559	4.334	5.917	7.682	9.470	11.386
3.2198	4.570	6.296	8.194	10.093	12.127
3.2783	4.884	6.769	8.786	10.839	13.065
3.3440	5.374	7.436	9.585	11.786	14.235
3.4064	6.063	8.263	10.575	12.932	15.589
3.4714	6.975	9.376	11.826	14.368	17.240
3.5286	8.336	10.912	13.580	16.360	19.671

(a) All LVDT readings in the table are in volts. The following calibration equations apply:

1) For crack lengths between 1.1440 and 2.1829 in.
(COD) in.= 8.199×10^{-4} [(COD) volts - 3.100]- 8.017×10^{-5}.

2) For crack lengths between 2.2179 and 3.5286 in.
(COD) in. = 4.997×10^{-3} [(COD) volts - 3.005] +5.177×10^{-4}.

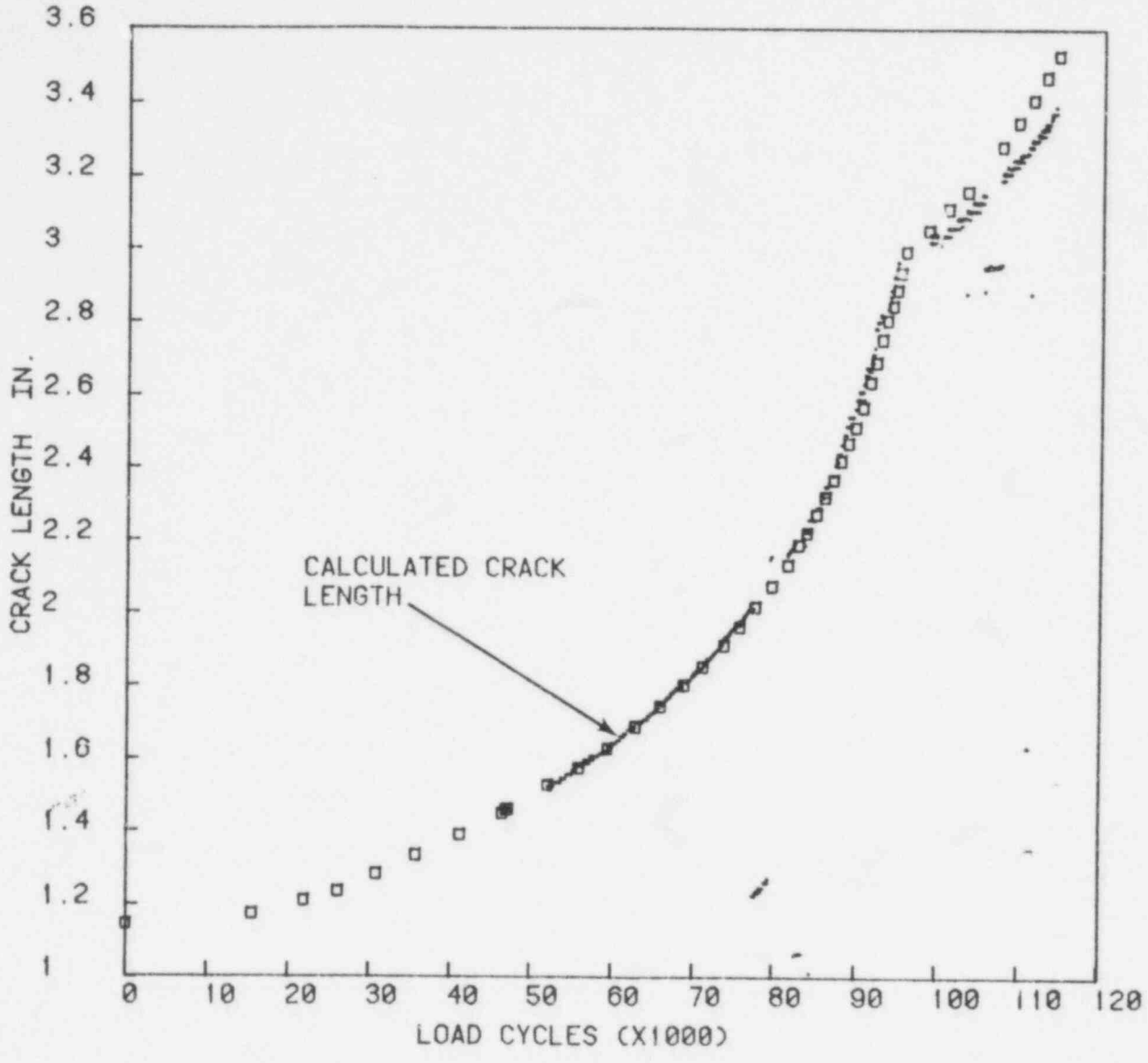

FIGURE 3. Measured and Calculated Crack Lengths as a Function of Load Cycles for SEN Specimen 1-1A-3B

where a is the crack length, W is the specimen width and A, B are constants. Equation (2) is similar to the analytical expression derived by Tada (Paris and Irwin 1973). A plot, given in Figure 4, shows the raw data and the two equations obtained for the different R-ratios employed. The points in Figure 3 were then computed by using COD readings recorded every 100 load cycles by the AE monitoring equipment and iteratively solving Equation (2) for the crack

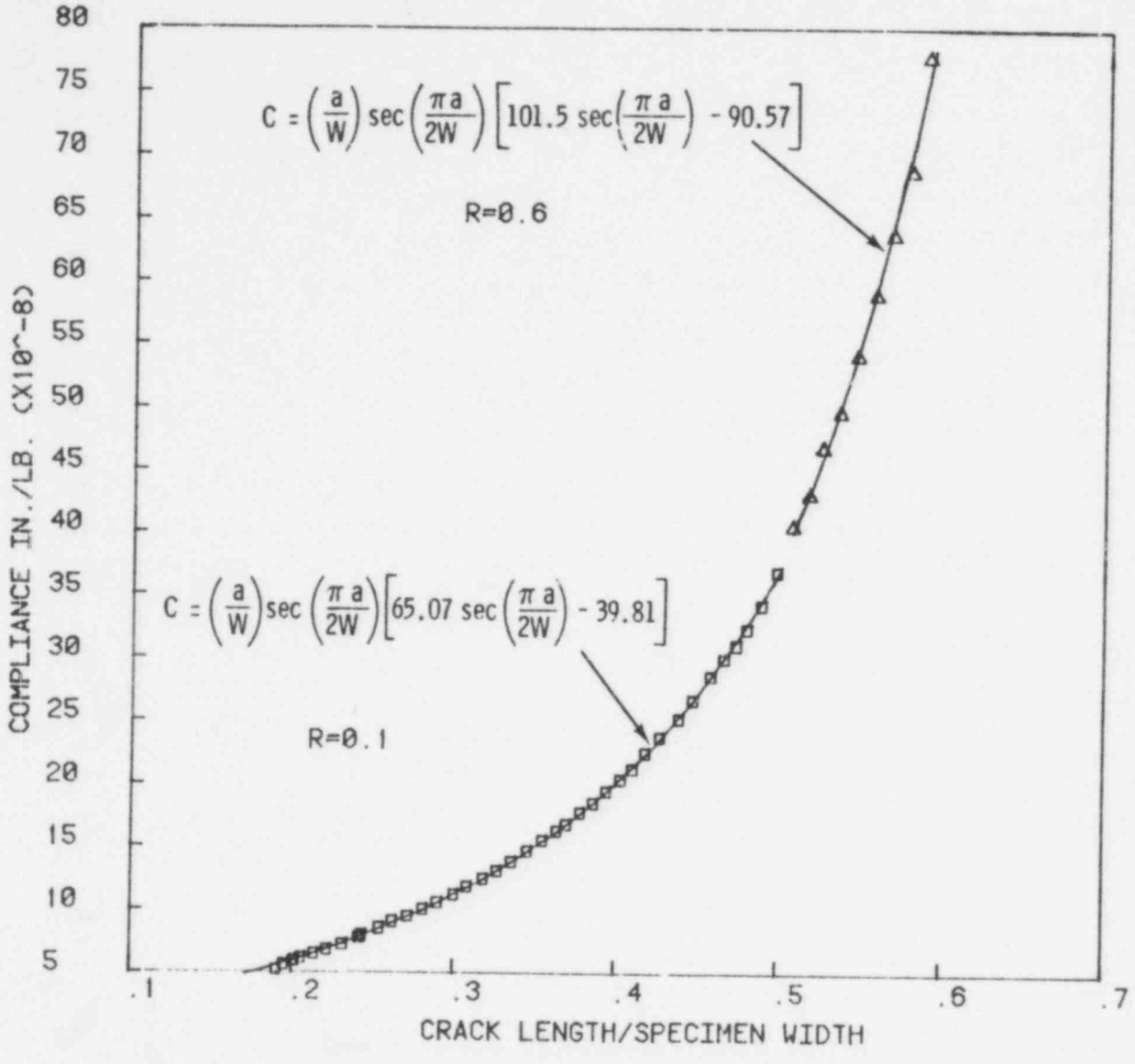

FIGURE 4. Compliance as a Function of Crack Length/Specimen Width Ratio for SEN Specimen 1-1A-3B

length. The reason for selecting 100 load cycle increments was to obtain sufficient crack length resolution without overwhelming the data processing capability of the computer. The results shown in Figure 3 indicate that for R=0.1 reasonably good agreement between measured and calculated crack lengths was obtained, but at R=0.6 significant deviations were observed. No explanations for these deviations has been formulated at this time.

The intent of this work was to develop a method for determining whether the mechanism for FCG in A533B steel is a continuous or discontinuous process, since the AE response tends to be essentially discontinuous over 100 load cycle increments. Scanning electron microscopy of FCG fracture surfaces does not provide many answers to this question, because this material tends not to exhibit fatigue striations. Improvements to the AE monitoring equipment to enhance the resolution of the COD measurements are currently in progress to aid in resolving this issue.

FRACTURE TEST EXPERIMENTAL RESULTS

Experimental results for fracture testing of SN specimen 1-2A-4A are listed in Table 5 and a plot of the load, COD, and AE count as a function of time as shown in Figure 5.

FATIGUE CRACK GROWTH TEST ANALYSIS

Figure 6 shows the FCG rate ($\frac{da}{dn}$) versus stress intensity factor range (ΔK) for specimen 1-1A-3B tested at RT. The equation:

$$\frac{da}{dn} = 4.14 \times 10^{-9} (\Delta K)^{2.21} \qquad (3)$$

is a least mean squares curve fit to the 42 data points with ΔK values greater than 33 Ksi in. (above "knee" in curve). The data points used to compute Equation (3) were obtained at three distinct conditions: (1) 13 data points at ν (cyclic frequency) = 2.0 Hz, R(P min/Pmax) = 0.1; (2) 20 data points at ν = 0.1 Hz, R=0.1 and (3) 9 data points at ν = 2.0 Hz, R=0.6. The equation is essentially the same, within experimental scatter, as equations obtained from other specimens with through-wall notch geometries (Hutton, Schwenk, and Kurtz 1978b,c). Additionally there was no observable effect of R-ratio or cyclic frequency upon the crack growth rate in air at RT. The other equation plotted in Figure 6 (below the kneed) was not computed from data points obtained on specimen 1-1A-3B, but was obtained from data taken on similar specimens

791077

TABLE 5. Acoustic Emission - Mechanical Data for 550°F Fracture Testing of SN Specimen 1-2A-4A

TIME, SEC	LOAD, KIPS	COD, IN.	COUNT	ENERGY
0	0	0	0	0
16	3.2	0	1	90
56	4.8	0	2	178
76	6.2	0	2	178
96	9.4	0	2	178
116	13.4	0	2	178
136	18.0	0	2	178
156	25.0	0	2	178
176	27.4	0	2	178
196	32.1	0	2	178
216	36.7	.002	3	214
236	40.7	.002	3	214
256	43.9	.002	5	414
276	48.5	.002	5	414
296	52.5	.002	5	414
316	56.3	.002	5	414
336	61.1	.002	5	414
356	65.7	.002	6	462
376	71.3	.002	6	462
396	76.7	.003	7	538
416	83.1	.003	8	636
436	87.7	.003	8	636
456	90.9	.005	10	778
476	94.9	.005	10	778
496	98.7	.005	10	778
516	102.7	.005	10	778
536	106.5	.005	10	778
556	110.5	.005	10	778
576	114.5	.007	10	778
596	119.1	.007	10	778

TABLE 5. (Contd)

TIME, SEC	LOAD, KIPS	COD, IN.	COUNT	ENERGY
616	123.1	.008	10	778
636	126.9	.008	10	778
656	131.6	.008	10	778
676	135.4	.010	10	778
696	140.2	.012	11	810
716	143.4	.012	12	928
736	147.2	.014	12	928
756	150.4	.016	12	928
776	154.4	.017	12	928
796	157.4	.019	12	928
816	161.4	.019	12	928
836	164.6	.021	12	928
856	167.6	.024	12	928
876	170.8	.026	12	928
896	174.0	.029	13	1002
916	177.0	.031	13	1002
936	179.4	.035	13	1002
956	182.6	.038	13	1002
976	184.8	.042	13	1002
996	187.2	.045	15	1334
1016	188.8	.049	15	1334
1036	191.2	.052	15	1334
1056	192.8	.057	17	1596
1076	195.0	.063	21	2376
1096	196.6	.068	22	2648
1116	197.4	.071	23	2862
1136	199.0	.078	24	2962
1156	199.8	.084	24	2962
1176	199.8	.089	26	3170

TABLE 5. (Contd)

TIME, SEC	LOAD, KIPS	COD, IN.	COUNT	ENERGY
1196	199.8	.096	29	3470
1216	199.8	.103	31	3718
1236	199.8	.110	31	3718
1256	199.8	.119	31	3718
1276	199.0	.139	38	4512
1296	167.6	.194	54	7324

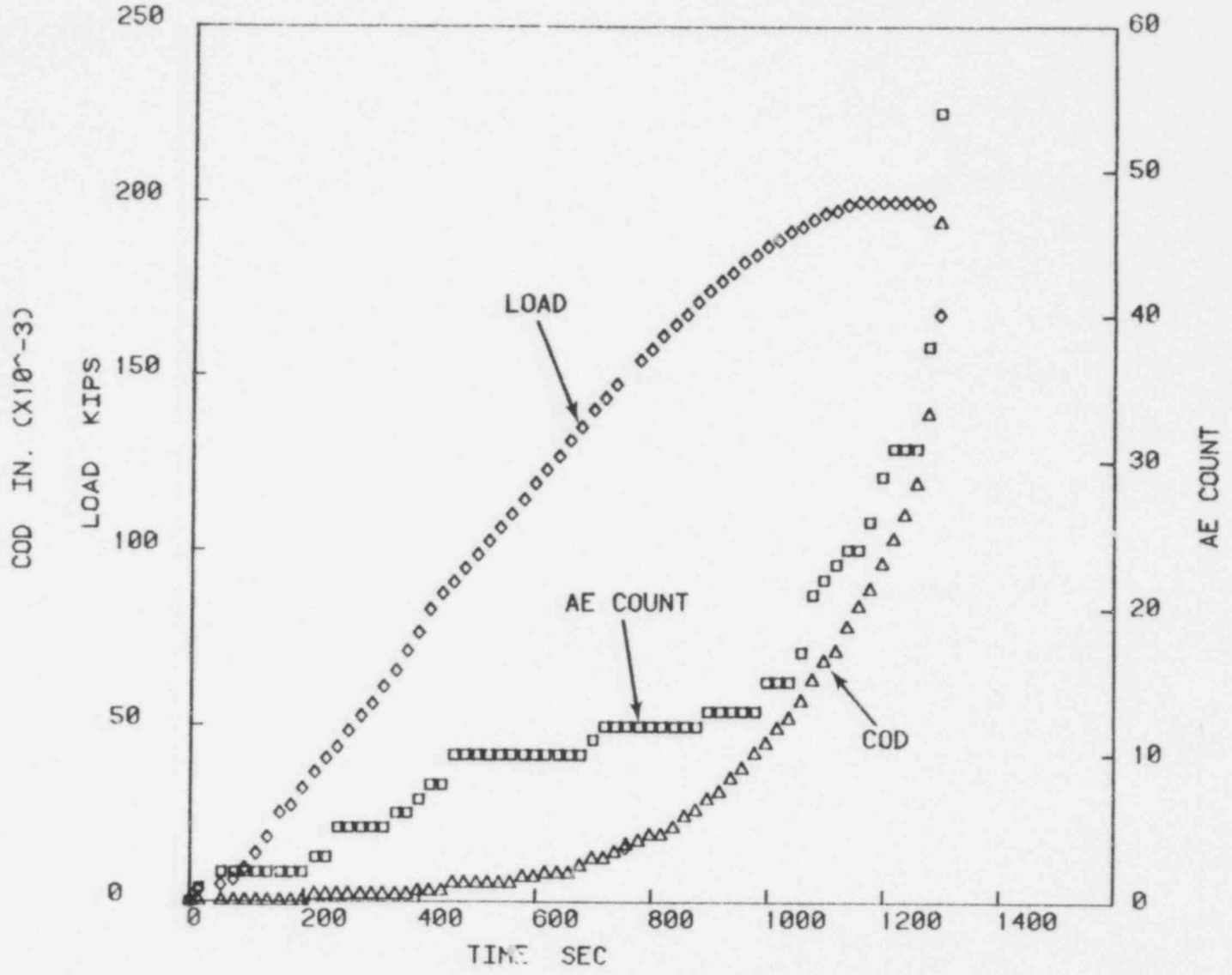

FIGURE 5. Load, COD, and AE Count as a Function of Time for SN Fracture Specimen 1-2A-4A

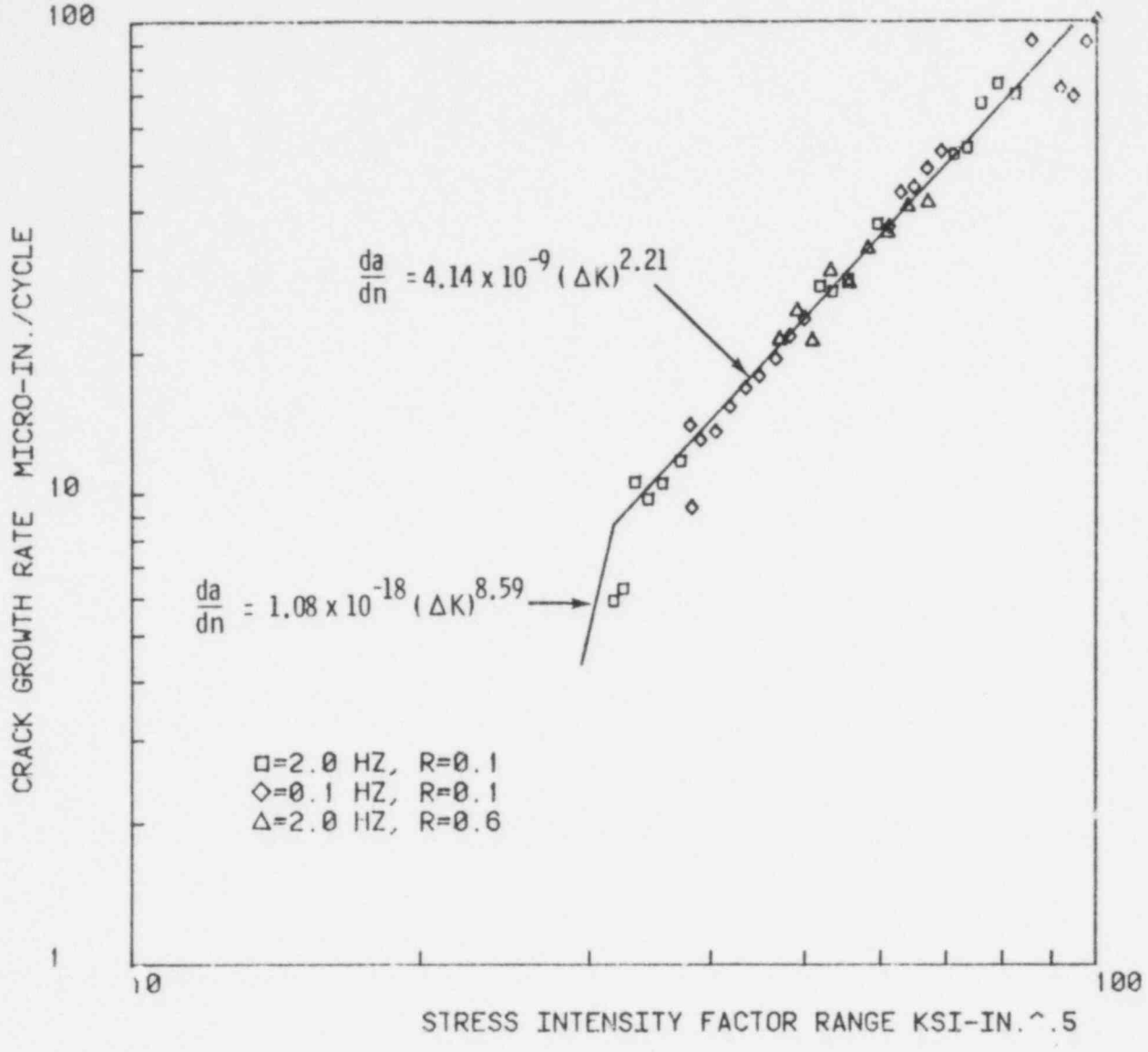

FIGURE 6. Fatigue Crack Growth Rate as a Function of Stress Intensity Factor Range for SEN Specimen 1-1A-3B

(Hutton, Schwenk, and Kurtz 1978b,c). The latter equation is included for reference purposes.

A plot of the AE event count/cycle as a function of FCG rate is shown in Figure 7. The open symbols in Figure 7 corresponds to AE data collected over the entire load waveform, whereas the filled points represent that fraction of the AE data obtained during 80 percent of the rising portion of the load

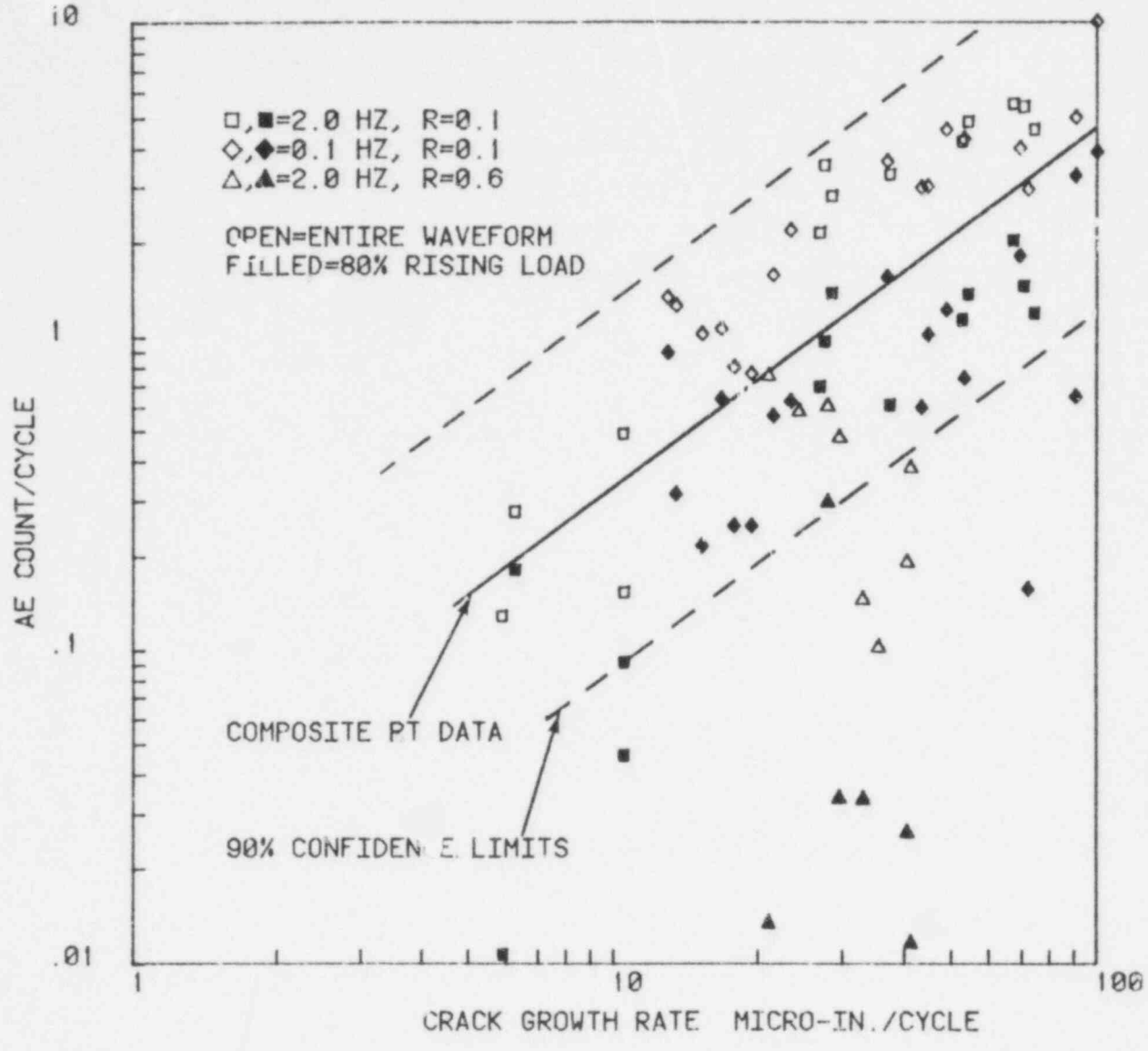

FIGURE 7. AE Count/Cycle Versus Fatigue Crack Growth Rate for SEN Specimen 1-1A-3B

waveform. These latter results will be discussed below. In general the non-load waveform partitioned data show no statistically significant effect of cycle rates investigated, when compared within the same data set or with RT data obtained previously (Hutton, Schwenk, and Kurtz 1973c) (note solid and dashed lines in Figure 7). The dashed lines represent the 90 percent confidence limits for the composite RT data. This result is significant from a

practical AE monitoring standpoint. On a reactor the notion of a "load cycle" has limited physical meaning, because the operational thermal and mechanical vessel loadings are probably not constant amplitude or constant frequency. Thus the empirical rate model developed so far $dN/dn = C(\Delta K)^m$, does not represent a practical basis for reactor monitoring. Because the AE response was independent of load cycle rate, for the cycle rates used in specimen 1-1A-3B, it may be feasible to substitute time for load cycles in the rate equation. This type of relationship (dN/dt instead of dN/dn) would then be more useful for field application.

To more closely simulate reactor loadings, data were also collected at R=0.6, as shown by the triangles in Figure 7. For equal values of the FCG rate, there was a considerable decline in the number of event counts/cycle for high R (0.6) in comparison to low R (0.1) data. However, this might have been influenced by the increasing state of net section plasticity since these data were obtained near the end of the test. This same type of behavior has been observed previously on other SEN test specimens (Hutton, Schwenk, and Kurtz 1978a).

Additional analyses of the data from specimen 1-1A-3B were performed this past quarter to see if load position partitioning (in concert with additional AE signal analysis) would aid in reducing the inherent scatter in the unpartitioned AE results. Plots of percent AE count as a function of position on the load waveform are given in Figures 8 to 10. The plots were constructed by partitioning the load waveform into 20 equal regions, with each region consisting of five load position "units" (0-4, 5-9, 10-14, etc). For each crack growth increment, the percent of the total AE count for that increment was determined for each region. Then the average for all crack growth increments of similar loading frequency and R-ratio were plotted in Figures 8 to 10 along with the maximum and minimum readings. The results were most interesting in that the trend of the data was the same regardless of loading frequency or R-ratio. Furthermore, it was surprising that very little AE response was obtained at either maximum or minimum load. Also, there was an extensive range of the data during the descending portion of the load cycle. This broad range may, in part, have been responsible for the tremendous scatter observed in the rate

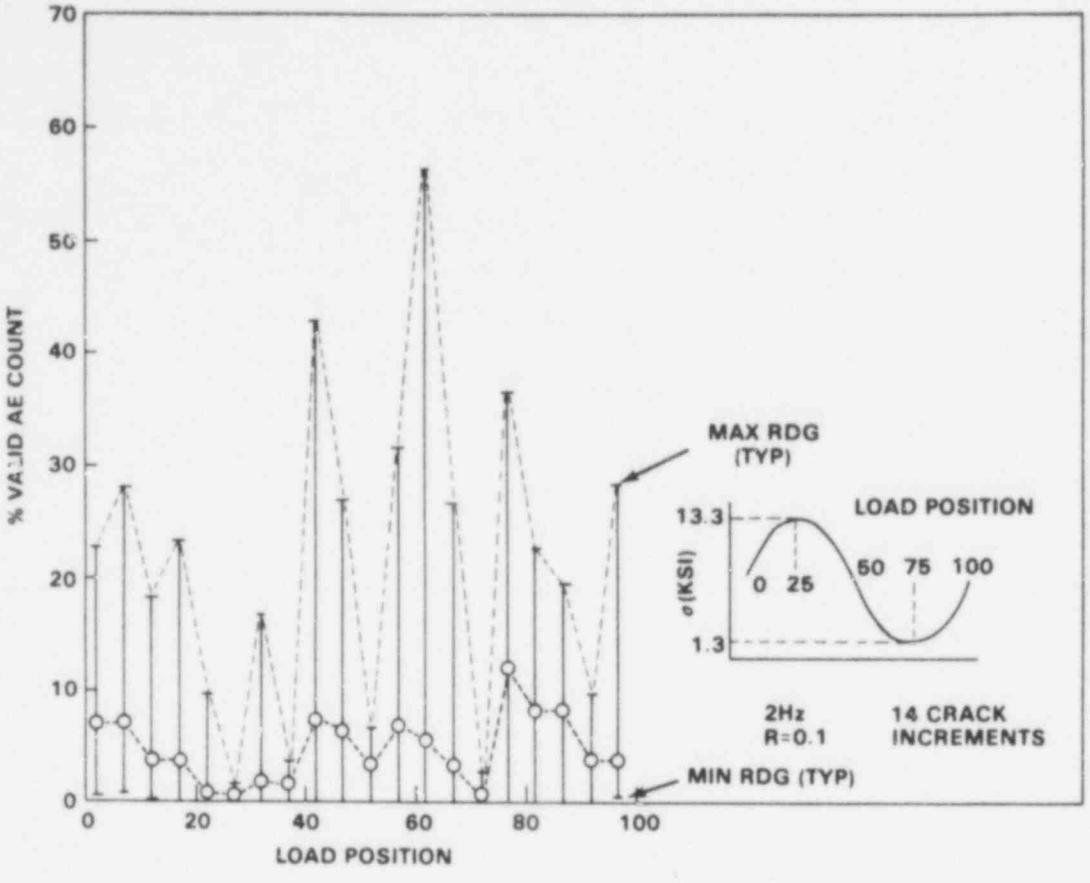

FIGURE 8. Percent AE as a Function of Load Position R=0.1, 2 Hz

data. To test this hypothesis the AE data were partitioned so that a given count was accepted if and only if it occurred during 80 percent of the rising portion of the load waveform. The influence of this type of partitioning on the rate data is shown in Figure 7. Notice that the effect of partitioning was to shift the rate plot downward and to the right of the unpartitioned data. The slopes of the two curves (excluding R=0.6 data) were nearly the same, with the unpartitioned data yielding a slope of about 1.3 and the partitioned data a slope of 1.2. Moreover, the effects of cycle rate and R-ratio were not significantly altered. Unfortunately, partitioning with respect to the load waveform did not reduce the scatter appreciably.

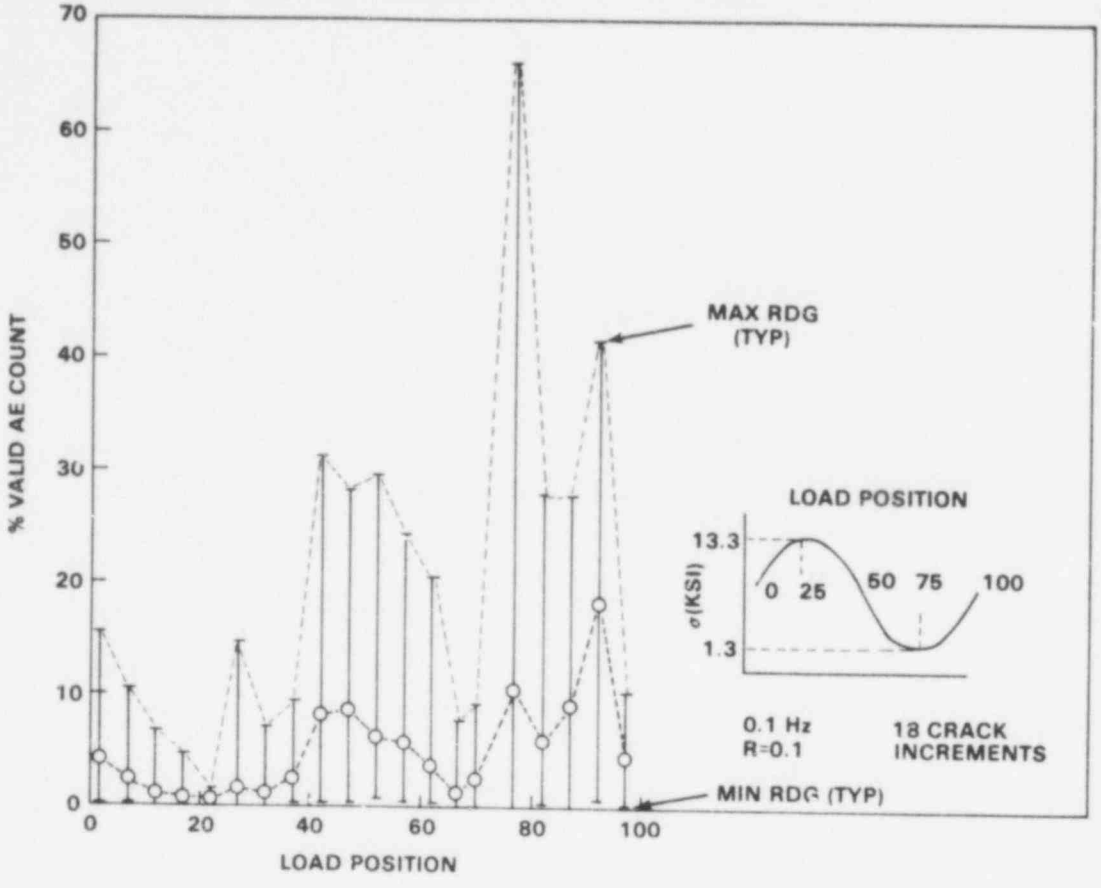

FIGURE 9. Percent AE as a Function of Load Position, R=0.1, 0.1 Hz

Other work this past quarter has concentrated on learning more about the characteristics of the AE signals obtained during FCG. Figures 11 to 16 show the results of these analyses. All of the graphs show an AE parameter plotted against load cycles. The total number of load cycles shown in the plots does not correspond to the total number of cycles applied to specimen 1-1A-3B, since some of the AE data was lost due to equipment malfunction (see Table 3 for the specific crack growth increments). Nevertheless, each plot is subdivided into regions of constant mechanical loading conditions. These regions are defined as follows:

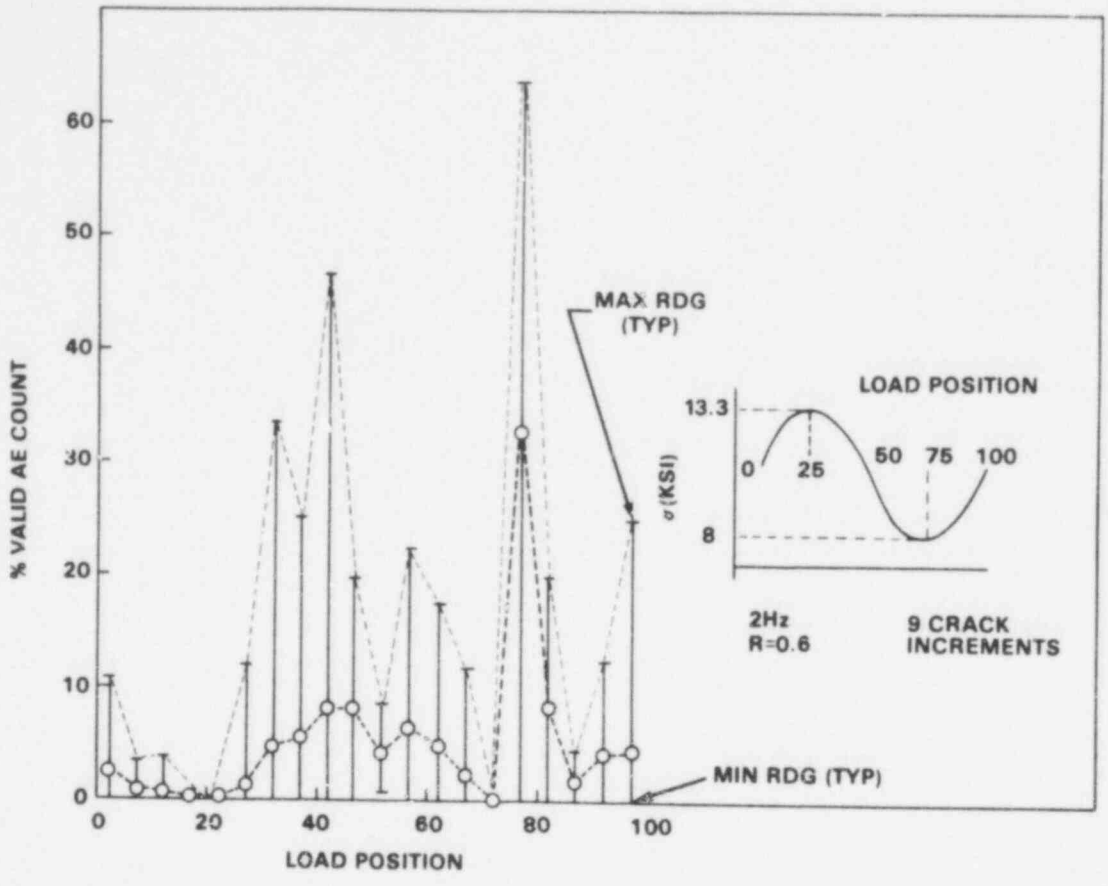

FIGURE 10. Percent AE as a Function of Load Position, R=0.6 2 Hz

Region	Loading Conditions
A	2.0 Hz, R = 0.1
B	0.1 Hz, R = 0.1
C	2.0 Hz, R = 0.6

The first graph (Figure 11) shows the average AE energy/count (averaged over a 100 load cycle increment) as a function of load cycles. The purpose of this effort was to determine if AE energy could be used as a rational means for partitioning the AE data. Note that the average energy/count does not appear to depend upon cyclic frequency or R-ratio, but does seem to be influenced by crack growth rate. In the early (0 to 46,000 cycles) and late

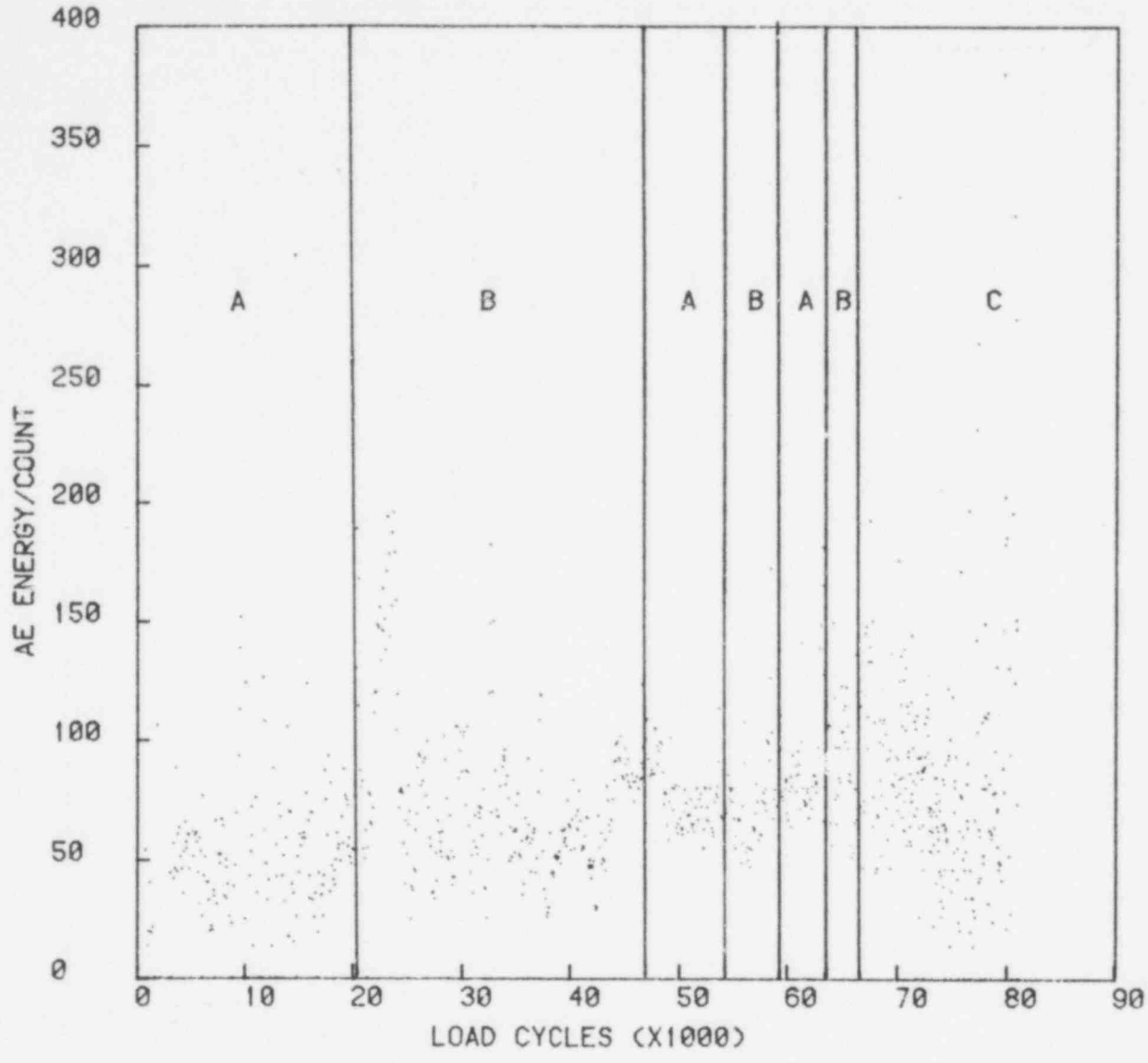

FIGURE 11. Average AE Energy/Count (100 Cycle Increment) Versus Load Cycles for SEN Specimen 1-1A-3B

(>66,000 cycles) stages of the test, when the crack growth rate was less than approximately 5×10^{-6} in./cycle, the average energy/count shows much more scatter than when the crack growth rates were greater than approximately 5×10^{-6} in./cycle (46,000 to 66,000 cycles). Interestingly, on an average basis, the predominate energy/count was in the range 30 to 150 energy units. To investigate this trend further and to separate the possible bias that a few

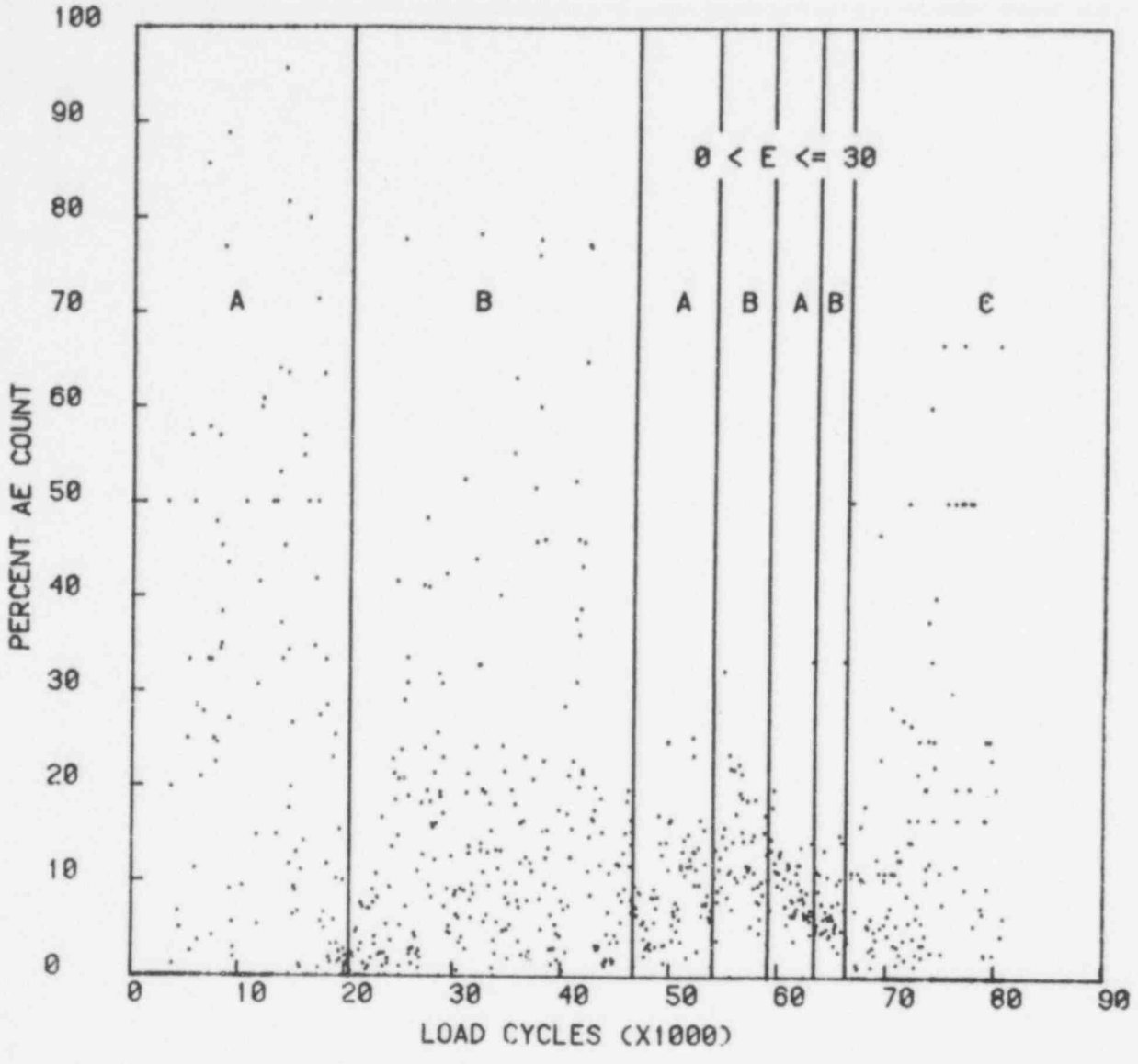

FIGURE 12. Percent AE Count Versus Load Cycles for SEN Specimen 1-1A-3B, $0 < E \leq 30$

high energy counts may have imparted to the average energy/count analysis, the AE data were partitioned into three energy ranges. Plots of the percent AE count obtained for each energy range were made over 100 load cycle increments. The results are given in Figures 12 to 14 with the following energy ranges used for partitioning: 1) $0 < E \leq 30$ (Figure 12); 2) $30 < E \leq 150$ (Figure 13); and 3) $E > 150$ (Figure 14). These data show that at crack growth rates

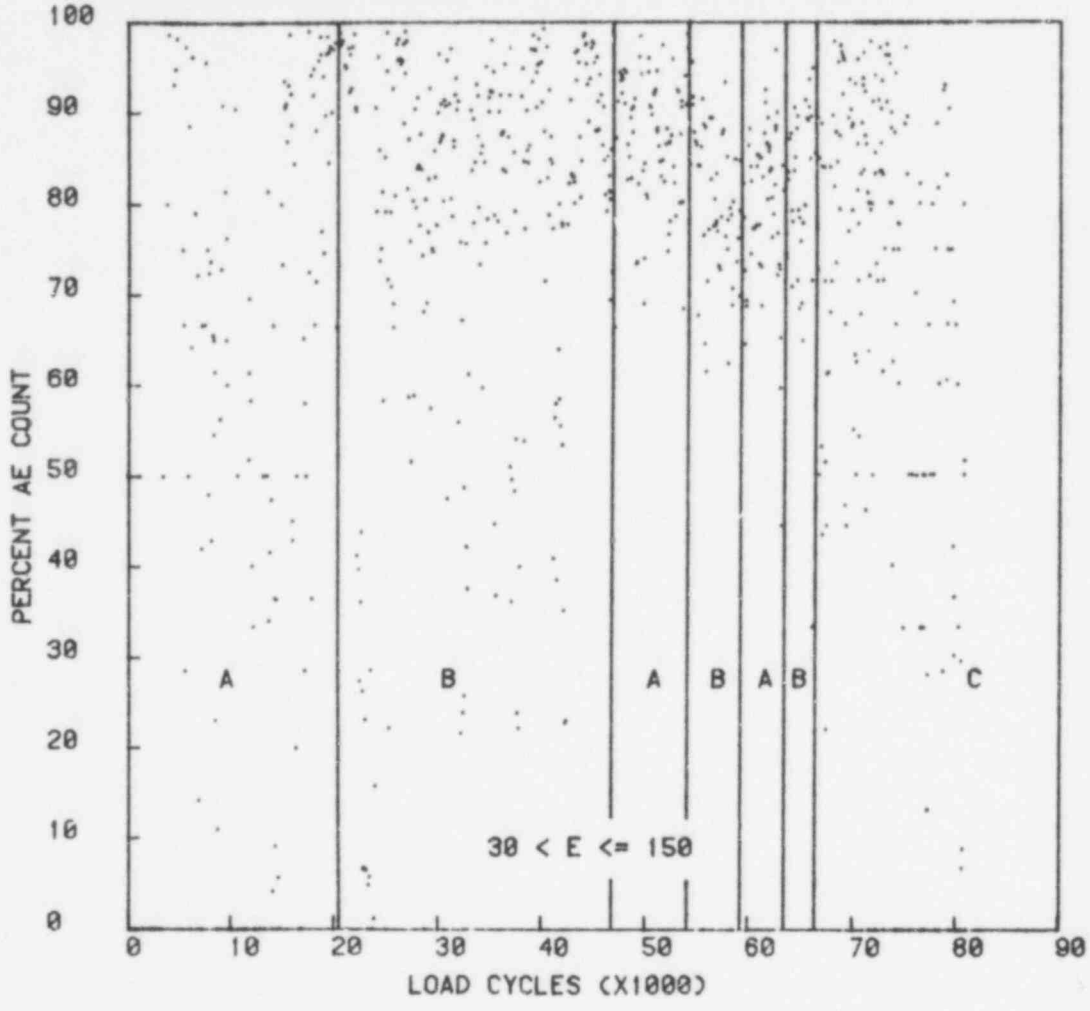

FIGURE 13. Percent AE Count Versus Load Cycles for SEN Specimen 1-1A-3B, $30 < E \leq 150$

greater than approximately 5×10^{-6} in./cycle the percentage of low energy ($E \leq 30$) and high energy ($E > 150$) signals is quite low relative to count with energies between 30 and 150 energy units. On the other hand, at the lower crack growth rates, there does not appear to be any consistent pattern. As with the data plotted in Figure 11, there does not seem to be any influence of cyclic frequency or R-ratio upon the distribution of signals within the various energy ranges.

Figure 15 shows the AE energy/pulse height averaged over 100 load cycle increments. This work was performed in an effort to determine the degree to

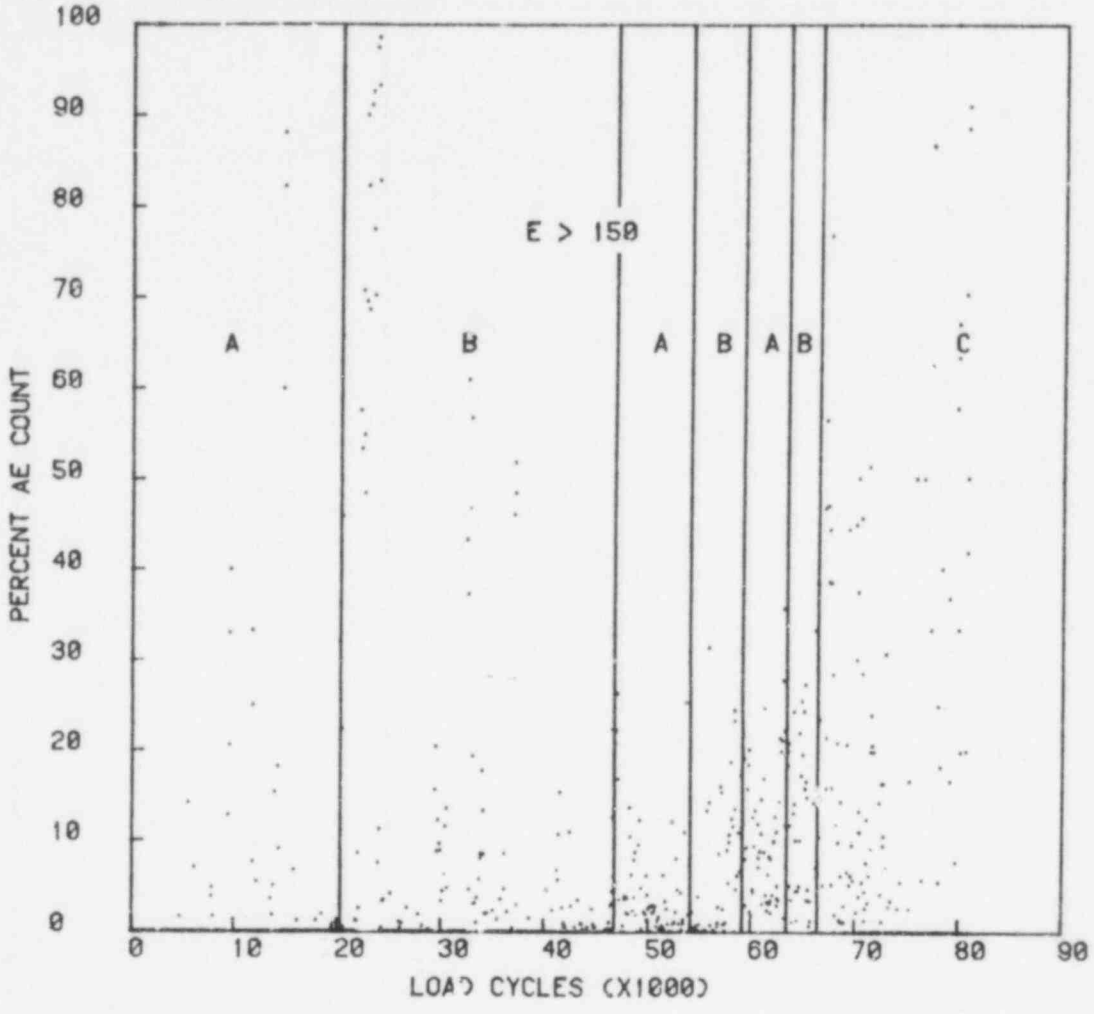

FIGURE 14. Percent AE Count Versus Load Cycles for SEN Specimen 1-1A-3B, E > 150

which the energy and pulse height measurements were independent of each other. The results show that the average energy/pulse height falls within a fairly narrow band, except at low crack growth rates. This suggests that AE signals produced during RT-FCG do not vary much in aspect ratios, and that a measure of signal pulse height may yield a reasonable representation of the signal energy.

The results of a 100 load cycle average peak time/count analysis are plotted in Figure 16. The lack of a discernable trend in the data suggests that peak time along is not suitable for AE signal classification. This is

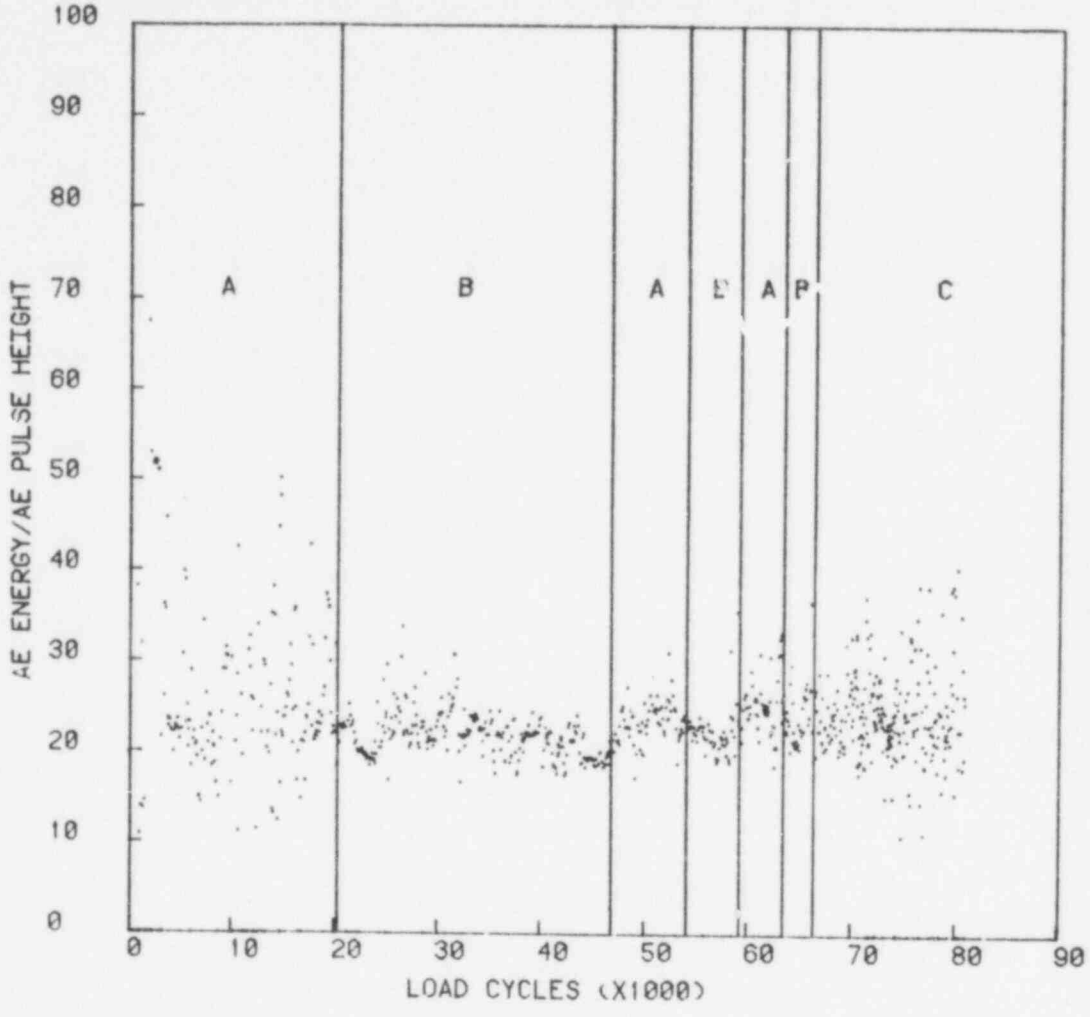

FIGURE 15. Average AE Energy/AE Pulse Height Versus Load Cycles for SEN Specimen 1-1A-3B

supported by results observed with AE data from other through-wall notch specimens, where the rate equation correlations have not improved much through peak-time partitioning of the data. In addition, an analysis of the average peak-time/pulse height as a function of load cycles did not reveal any consistent trends.

In summary, the effort to evaluate energy, pulse height, and peak time as AE signal characterization parameters has shown that:

1) the trend in AE data with respect to load position appears to be independent of cyclic frequency and R-ratio;

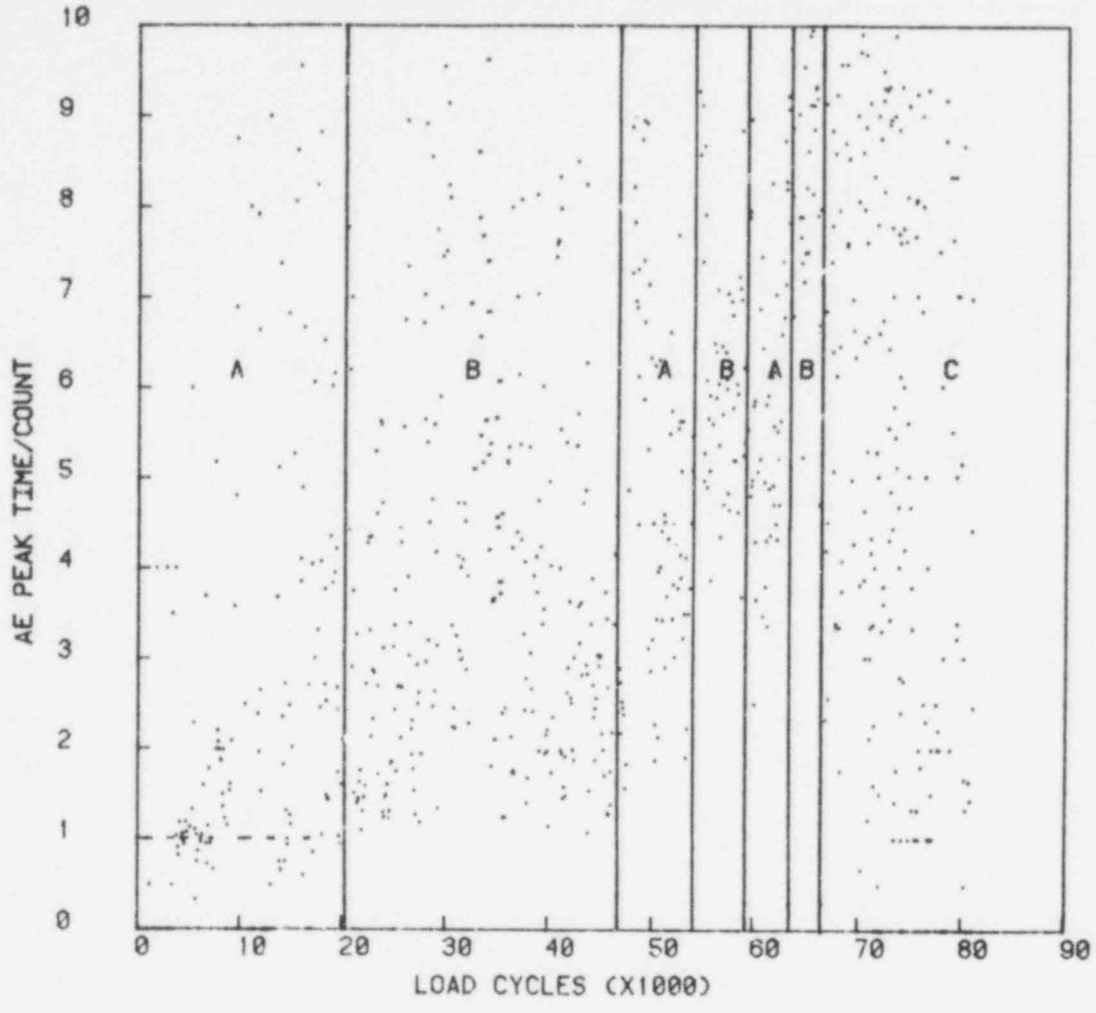

FIGURE 16. Average AE Peak Time/Count Versus Load Cycles for SEN Specimen 1-1A-3B

2) the average energy/count doesn't appear to depend upon cyclic frequency or R-ratio, but may depend on fatigue crack growth rate;

3) the percentage of AE count observed in a given energy range seems to be independent of cyclic frequency and R-ratio, but may depend on crack growth rate;

4) the AE energy and pulse height appear to be dependent on each other; and

5) the average peak time/count does not show any consistent trend with respect to cyclic frequency, R-ratio or crack growth rate.

FRACTURE TEST ANALYSIS

A graph of the load and AE count versus COD is given in Figure 17. The results from test 1-2A-4A are very similar to results obtained from an earlier RT test (2-1A-2B) (Hutton, Schwenk, and Kurtz 1978a). In both of these tests, AE was detected both before and after general yielding with linear AE versus COD curves up to general yielding followed by a smaller slope but still linear curves to failure. These results were analogous to the HSST vessel tests in the following ways: 1) The general shapes of the AE-COD plots were similar; 2) both the lab and vessel data displayed negligible effect of temperature (between -5° and 200°F levels) on the AE response; and 3) the crack and

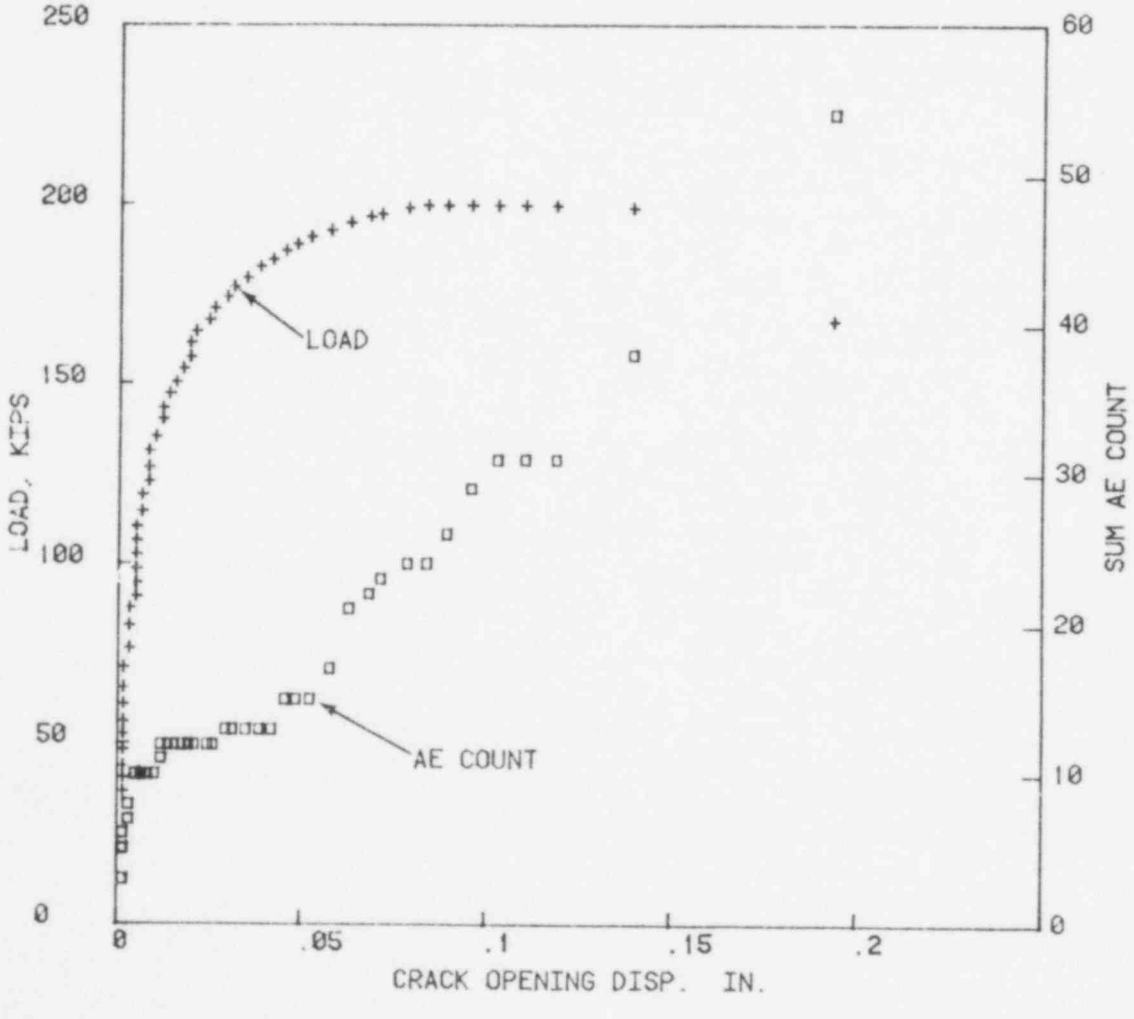

FIGURE 17. Load and AE Count Versus COD for SN Specimen 1-2A-4A at 550°F

loading geometries were similar. The form of the SN fracture data suggests that relationships developed from laboratory specimens (having crack and loading geometries which simulate the structure) will be beneficial to modeling of full-scale structures.

AE SIGNAL CHARACTERIZATION

Pattern recognition analysis is being investigated as a means of characterizing AE signals from crack growth to distinguish them from other acoustic signals (transient noise signals, slag inclusion cracking, etc.). Pattern recognition is the generic term for statistical techniques that classify objects described by multiple parameters. Examples of signal waveform parameters in the time domain include:

- peak amplitude
- rise time
- moments
- autocorrelations

In the frequency domain, via the fast Fourier Transform (FFT), possible parameters include:

- maximum frequency response
- energy in selected bandwidths
- power spectrum parameters
- cepstrum parameters

This technique is being developed for application in interpreting data in several other nondestructive examination areas. Adaptronics (1978a) has used the Adaptive Learning Network (ALN) method to analyze ultrasonic data to size flat bottom holes in steel test blocks and identify cracks in stainless steel pipe welds. With eddy-current data, Adaptronics (1978b) has used ALN to size two types of flaws in steam generator tubing. Bryan of the Air Force Office of Scientific Research (1977) used ultrasonic waveform features to classify different sizes of flat bottom holes in aluminum test blocks. Other such uses of pattern recognition have been documented (Mech 1978, Rose 1977, Ultrasonic

International 1978). Thus, it appears reasonasble to consider applying the technique to acoustic emission analysis.

Pattern recognition techniques are based on statistical probability theory and can be classified into two broad categories: feature reduction and classification. Feature reduction is necessitated by the often high degree of redundancy of information contained in the many features. This redundancy causes mathematical problems for the classification techniques, so feature reduction is a means of removing the redundancies.

The classification techniques perform decision-making functions analytically. One example of a classification technique that we have applied to the AE data is the least-squares decision rule. Let Z_1, ... Z_N be the observed values of N features obtained from a waveform (rise time, moments, etc.) and Y be the property of interest (say Y = 1 for noise and Y = 2 for valid AE). The function $Y = A_o + A_1Z_1 + A_2Z_2 + \ldots + A_NZ_N$, is fit by a least-squares minimization, where A_o, ..., A_N are parameters. The estimates of the parameters A_o, ..., A_N are inserted into the function to obtain an estimate of the property for each waveform as follows:

$$Y_i = A_o + A_1Z_{1i} + A_2Z_{2i} + \ldots A_NZ_{Ni} \qquad (4)$$

On the basis of these Y_i values, a value of Y (Y*), called the decision rule, is chosen which minimizes the number of misclassifications. A misclassification is defined as classifying a valid AE signal as noise and conversely.

EXPERIMENTAL RESULTS

For the initial evaluation of pattern recognition for AE characterization, waveform samples were digitized and recorded during test 1-1A-3B (FCG to study cycle rate effects). The waveforms were generated by our multiparameter AE monitor system operating in a normal manner. Using the source isolation system, only signals originating from the vicinity of the flaw were declared valid crack-growth AE signals. The load pattern applied to the specimen can be represented as a sine wave as shown in Figure 18. The period of the wave

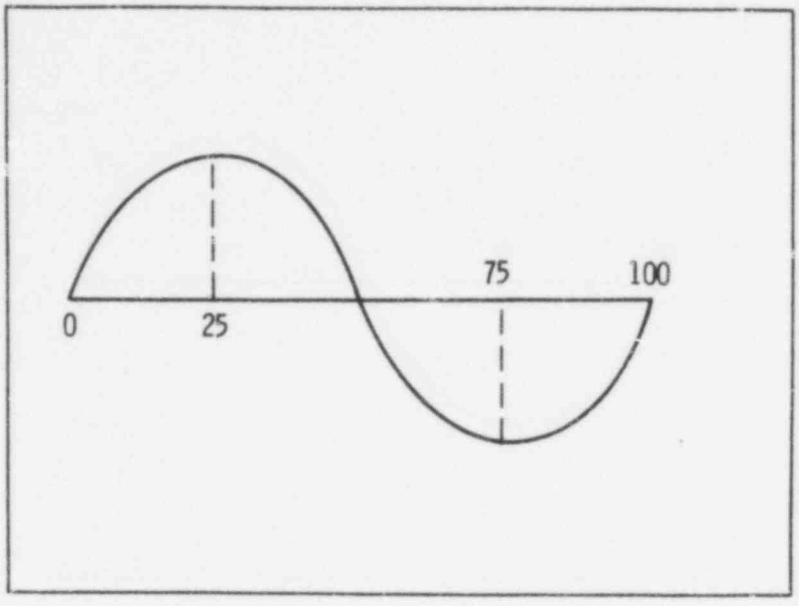

FIGURE 18. Fatigue Test Load Waveform

was arbitrarily divided into 100 parts. During the test, the position on the load curve (LC) was available as each valid AE waveform was recorded. The AE signals were then described as belonging to two groups: one corresponding to an increasing load (LC < 25 or LC > 75) and the other to a decreasing load (25 < LC < 75). This distinction was made because it was felt that AE signals generated in the two phases of the load cycle may show different characteristics.

Noise data from various sources were also generated in the area of the crack with the specimen in a static unloaded condition. The sources included:

- tapping the specimen with the blade and handle of a screwdriver
- rubbing the specimen with the hand and with cotton thread
- attaching a C-clamp on the specimen to simulate noise from pipe hangers, pipe brackets, or other friction-coupled devices
- turning the recording equipment off and on to produce electrical spikes
- breaking a Pentel pencil lead (0.5 mm by 0.25 in.) on the surface of the specimen at an angle of 30°.

The waveforms were dignitized using a Biomation 8100 transient waveform recorder with a sampling rate of 20 MHz. The digitized waveforms were read

out of the Biomation under computer control and recorded on magnetic storage medium.

The number of waveforms obtained for each classification are given in Table 6.

The Pentel signals saturated the monitor system so that none of those waveforms were usable. The electric noise waveforms were not used because the sample was too small to be significant.

For purposes of the preliminary analysis a subset of the data representing a complete cross-section of types of waveforms were chosen: 48 were noise and 50 were valid AE waveforms. An example of these waveforms is shown in Figure 19. The noise waveforms consisted of three types of noise: tapping, rubbing and clamp, in roughly equal numbers. The valid AE waveforms in the subset from each portion of the LC reflected the proportions seen in the complete data set. To avoid the problem of the overfitting of the decision function to the data, the 98 waveforms were divided into two groups: a training and a test set. The waveforms were randomly assigned to the two sets under the constraint that there should be an equal representation of each class of waveform (valid AE-increasing load, valid AE-decreasing load, tapping, rubbing, clamp) in each set. The purpose of this was to ensure that the two

TABLE 6. Number of Waveforms from Various Noise Sources and AE Signals

Source	Number
Valid AE	148
LC<25, LC>75	57
25<LC<75	91
Noise	81
Tapping	31
Rubbing	28
Clamp	16
Electric	6
Pentel	Saturated

NO. 40
NOISE
(COTTON THREAD RUBBING)

NO. 75
VALID AE

FIGURE 19. Sample Digitized Waveforms in Pattern Recognition Study

sets were as alike as possible. Decision analyses were performed on the training set and then validated on the test set.

Time Domain

Time domain features were examined first. In the time domain, we calculated the first four moments of the waveform. They are defined below, where X_i, i=1, ..., 2048 is the value of the digitized waveform:

$$\mu_1 = \frac{1}{N} \sum_i X_i$$

$$\mu_2 = \frac{1}{N} \sum_i (X_i - \mu_1)^2$$

$$\mu_3 = \frac{1}{N} \sum_i (X_i - \mu_1)^2$$

$$\mu_4 = \frac{1}{N} \sum_i (X_i - \mu_1)^4$$

We then produced four functions of the above moments and used them as features in the analysis. They are:

mean: μ_1 skewness: $\alpha_1 = \mu_3/(\mu_2)^{3/2}$

Standard Deviation: $\sigma \quad \sqrt{\frac{N}{N-1} \cdot \mu_2}$ kurtosis: $\alpha_2 = \mu_4/\mu_2^2$

Plots of the mean and standard deviation for the data in the training set are shown in Figure 20. The 0's on the plots correspond to valid AE waveforms, and the 1's, 2's and 5's represent, respectively, the feature values for clamp, tapping, and rubbing signals. If the feature of interest is a good differentiator of valid AE from noise, we would expect to see a definite value shift between the two groups. We do not see that for either feature.

The skewness and kurtosis values are shown in Figure 21. Again, there is no clear-cut differentiation between the two groups for these features. The plots of these four features for the test set showed the same behavior, so they are not given here.

The second type of time-domain feature we observed is the auto-correlation function. It is defined as:

$$C_k = \frac{\frac{1}{N} \sum_i (X_i-\mu_1)(X_{i+k}-\mu_1)}{\frac{1}{N} (X_i-\mu_1)^2}$$

$k = 0$

where k (called the lag) is the separation between two points of the digitized waveform. The feature C_k is simply the correlation between points of the waveform k distance apart. The mechanical properties of C_k are that $C_o = 1$ and $-1 \leq C_k \leq 1$. Figures 22 and 23 show the plot of the average of $C_k (k = 0, \ldots, 100)$ for, respectively, clamp, tapping, rubbing, and their average with the average auto-correlation for the valid AE signals. Although the curves start out the same, they diverge with the maximum differences occurring at around lags 48 and 69. This suggests that features based on auto-correlations have very good discrimination potential.

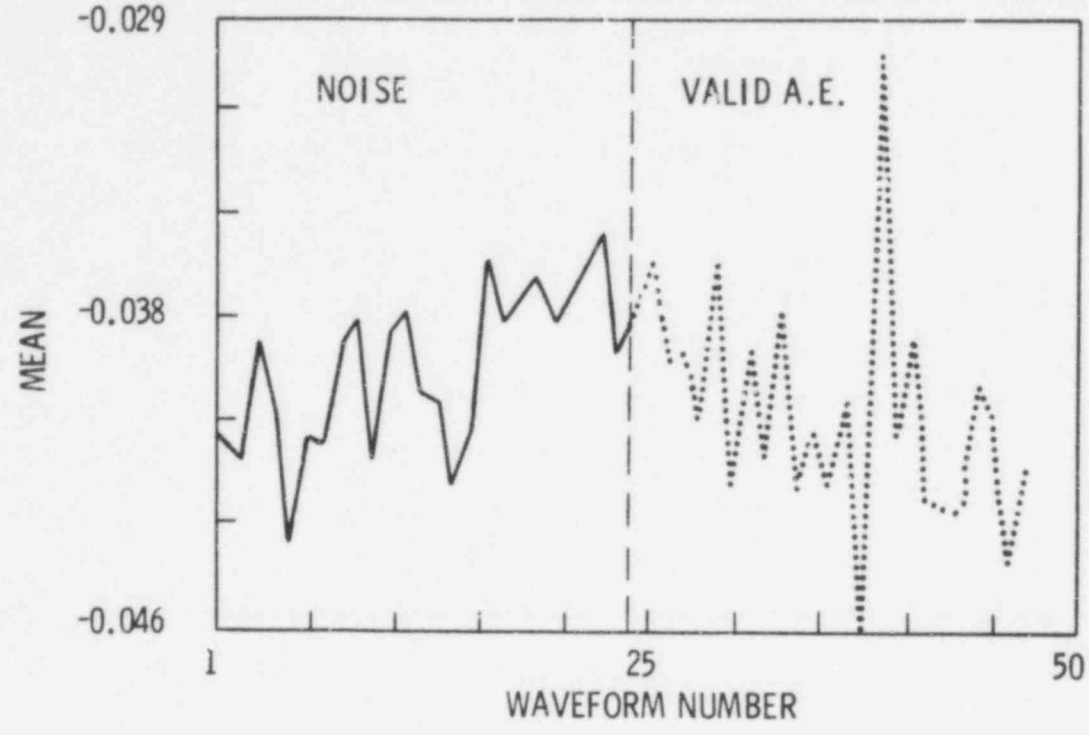

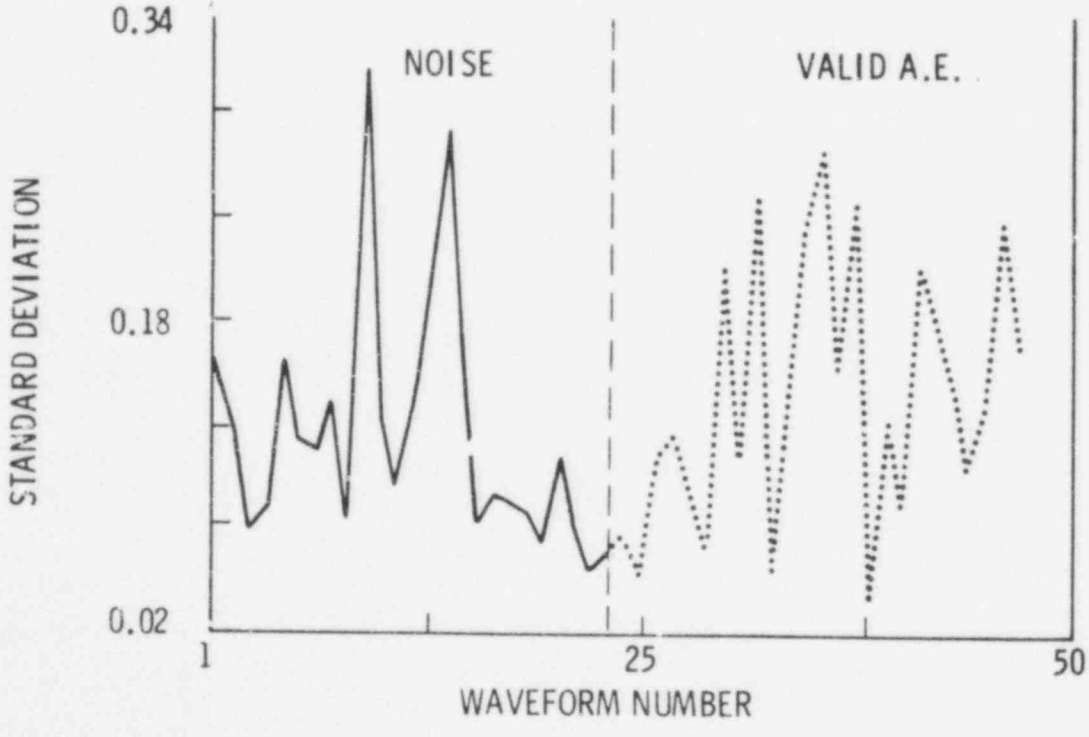

FIGURE 20. Mean and Standard Deviation - Training Data Set

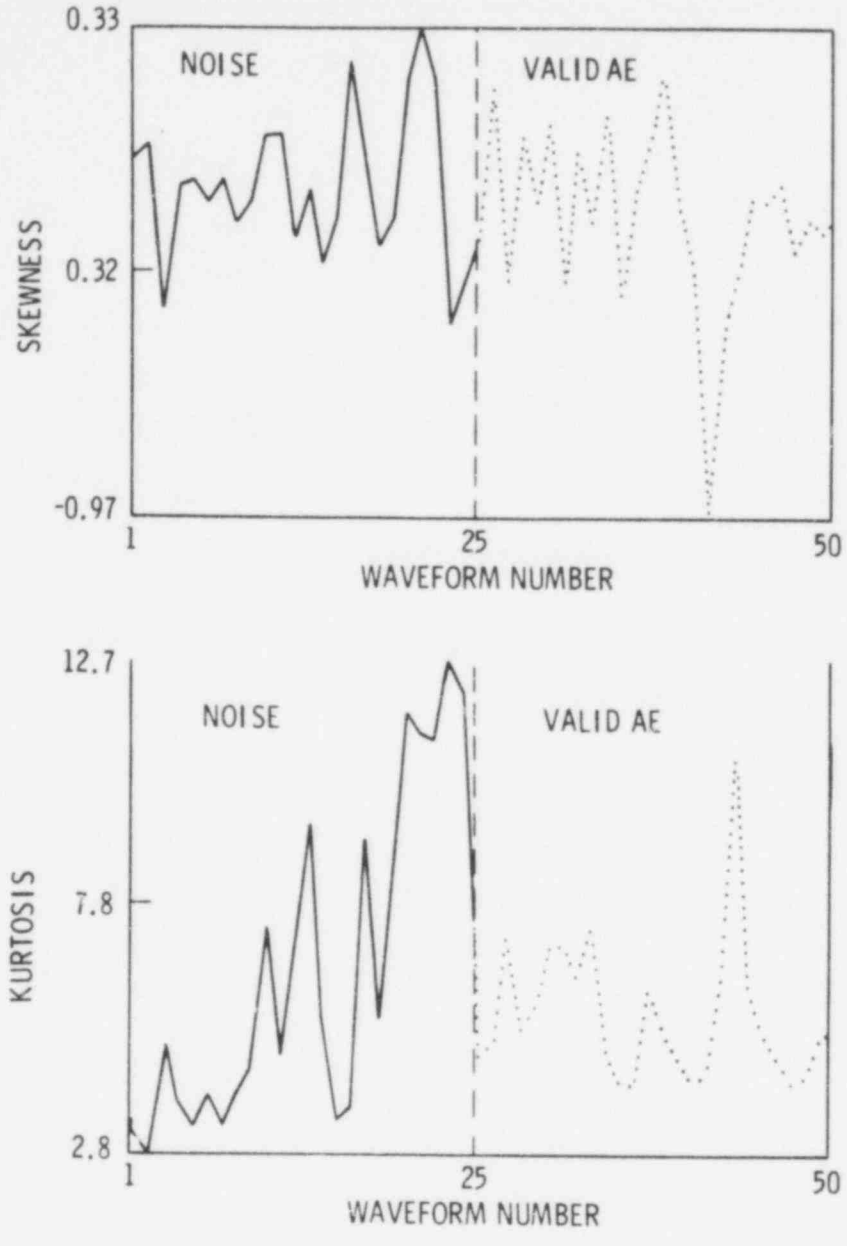

FIGURE 21. Skewness and Kurtosis - Training Data Set

Additional time domain features that were examined are the signal maximum and minimum and the times to maximum and minimum (Figures 24 and 25). They appear to have less separation potential than the moment features. The decision analysis was performed for the training and test sets separately and then both sets combined for the 10 features listed below.

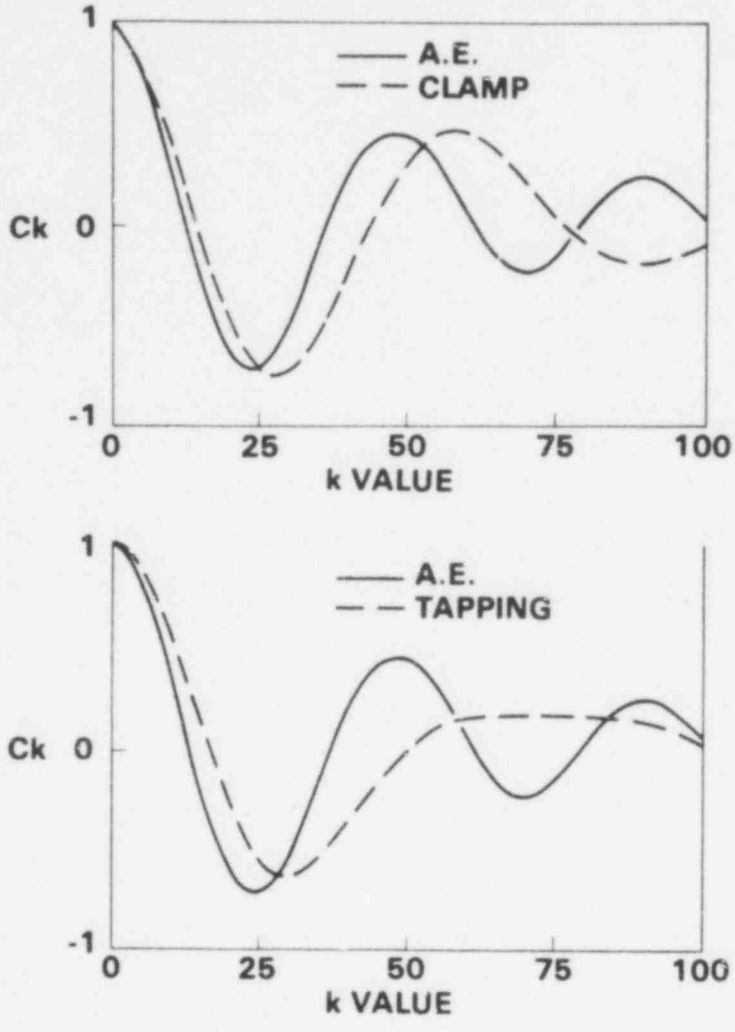

FIGURE 22. Auto-correlations for AE and Noise Waveforms

mean	lag 9
standard deviation	lag 11
skewness	lag 19
kurtosis	lag 48
auto-correlation (lag 8)	lag 69

It is informative to see the structure among the 10 features, which is shown in terms of interfeature correlations in Figure 26. The astericks represent product moment correlations significantly different from 0. This shows that there are two distinct clusters of features: the moments and the

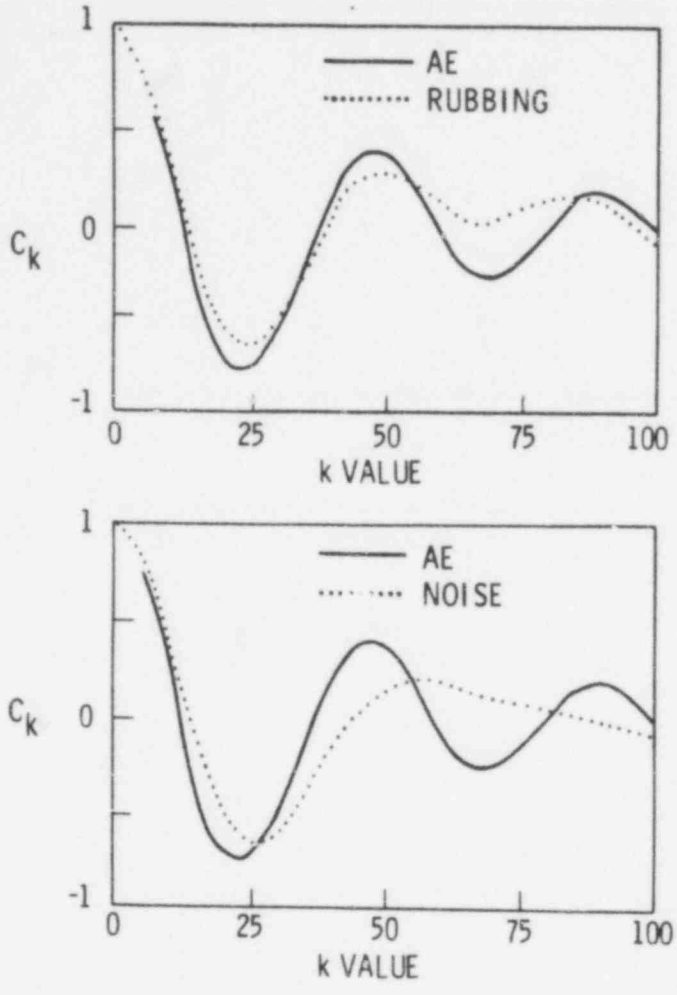

FIGURE 23. Auto-correlation for AE, Rubbing Noise and Average Noise

auto-correlation, and that the two sets of features provide different types of information.

The results of a least-squares decision analysis are given in Figure 27. The locations of dots represent the value of the decision function for noise waveforms and the x's the value of the decision function for valid AE waveforms. The line represents the Y* value (1.50) of the decision function, which minimizes the number of misclassifications. The circled points are misclassifications: there was only one misclassified noise signal compared to three for valid AE. In practice this is often not a desirable mix of the two types of misclassifications; however, the decision rule could be altered to

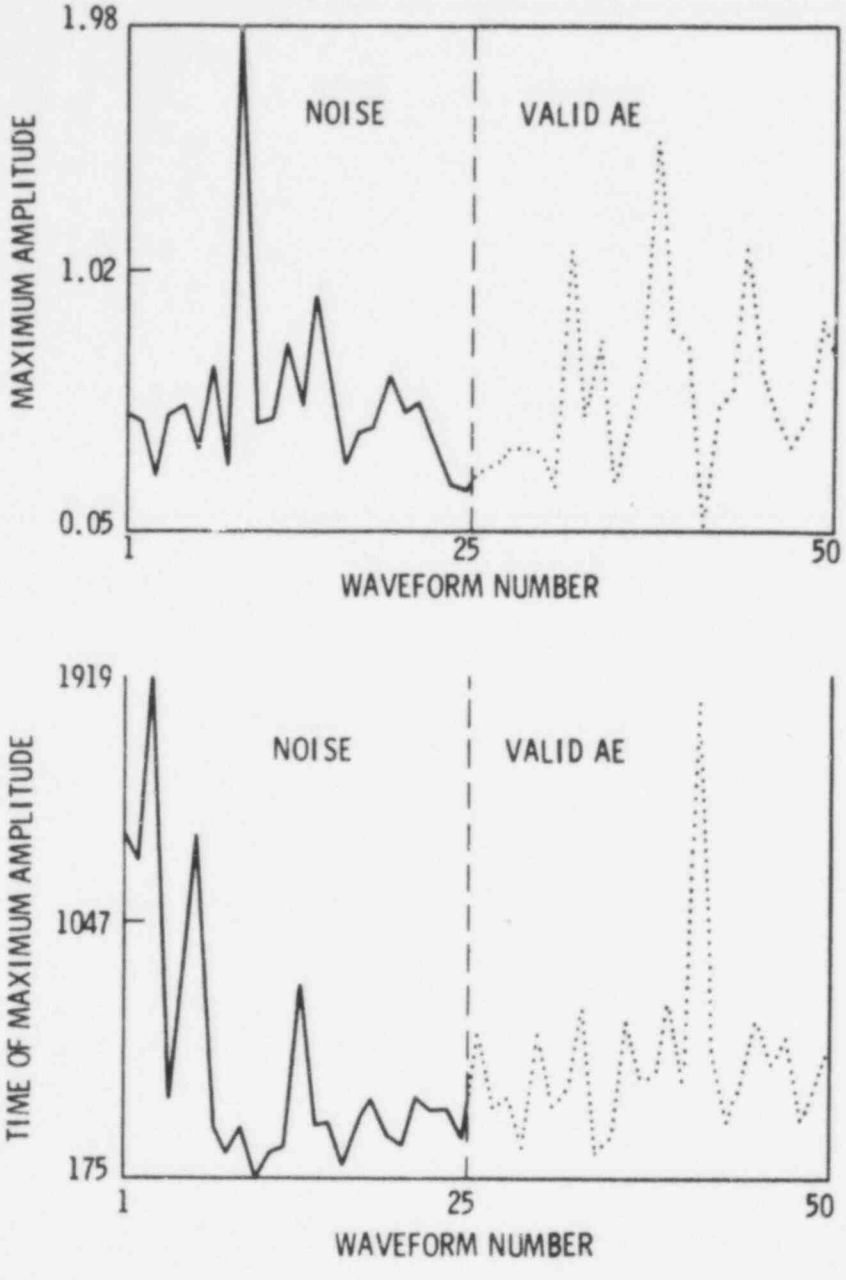

FIGURE 24. Signal Maximum and Time to Maximum

reflect a different emphasis in misclassifications. Overall there were 96 percent correct classifications. The two sample waveforms shown in Figure 19 are identified in Figure 27 by the two boxed points.

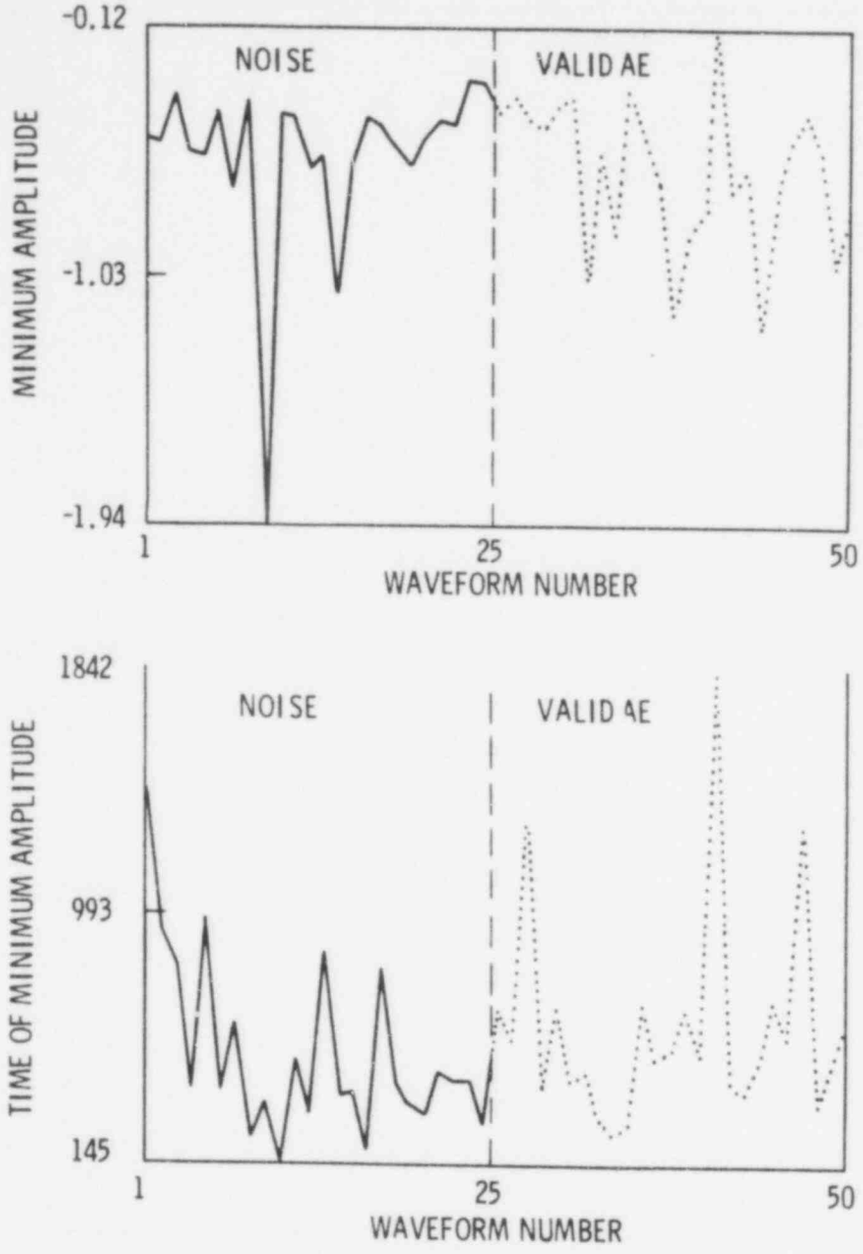

FIGURE 25. Signal Maximum and Time to Minimum

Frequency Domain

The investigation of AE characterization by pattern recognition has also included preliminary examination of the frequency domain. Figure 28 shows the averaged power spectrum of the 148 valid AE waveforms. The spectrum of each waveform was obtained using the fast Fourier transform (FFT) algorithm. Prior

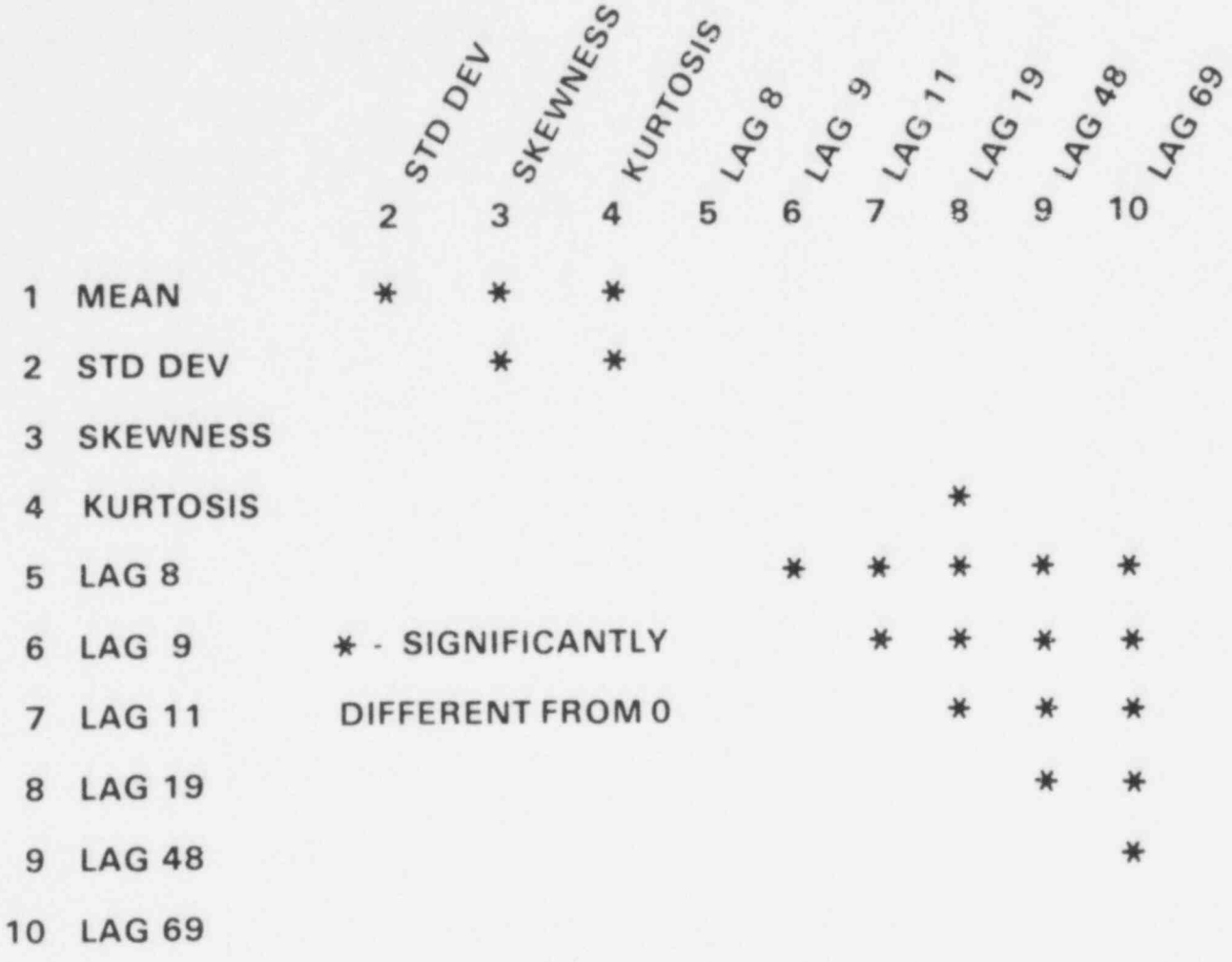

FIGURE 26. Interfeature Correlations

to computing the FFT, the mean of the waveform was removed by subtraction and the Hanning window applied. Two characteristics of this averaged power spectrum are worth mentioning. First, the maximum frequency response occurs at about 425 KHz. Secondly, the build up to this maximum is interrupted by a jagged plateau. Figure 29 shows the averaged power spectrum for the 75 noise waveforms. For this power spectrum, the maximum occurs at about 260 KHz and the rise to the maximum is smooth. Also, a jagged plateau follows the maximum. In comparing the spectra for valid AE and that of the noise sources, two differences are apparent: first, the location of the maximum response, 425 KHz for valid AE versus 260 KHz for noise; second, the location of the plateau with respect to the peak.

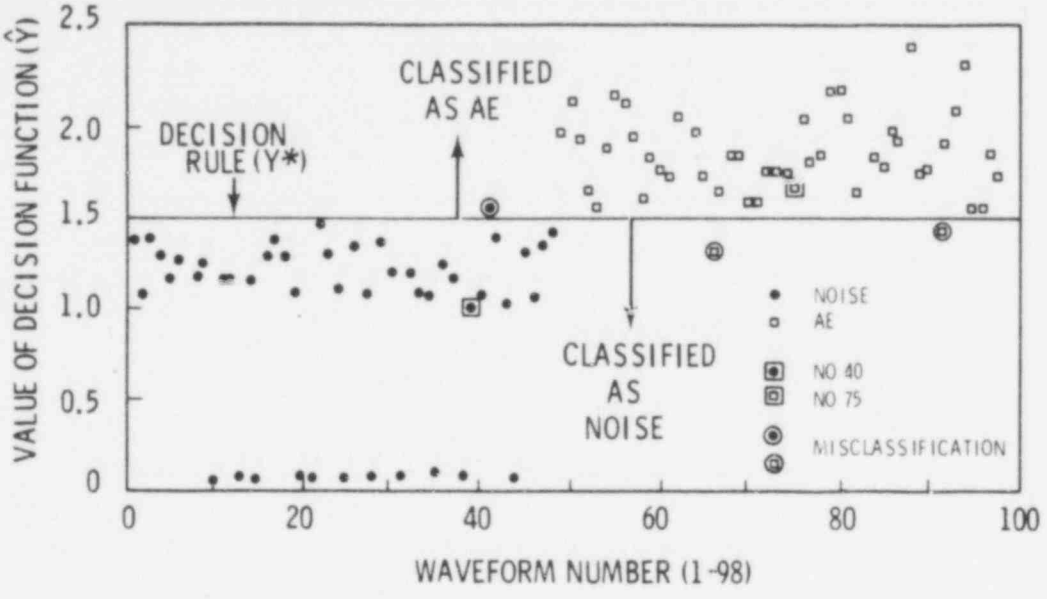

FIGURE 27. Preliminary Results of Pattern Recognition Analysis of Valid AE and Noise (96% Successful Classification)

Another feature calculated is the frequency of the maximum frequency response. We have calculated this feature for all 223 waveforms. The results of these calculations are plotted in Figure 30. Here we have again identified the feature by the number 0 if it corresponds to valid AE and by 1, 2 or 5, if it was computed from a noise waveform. Using only this single parameter to define our classification rule, we could pick the frequency which results in the least misclassification. Every waveform with the feature greater than this frequency would be classified as valid AE and those for which the calculated feature is less than the frequency would be classified as noise. With this approach, we can correctly classify 78 percent of the waveforms. This success rate is achieved without resorting to any pattern recognition algorithms. Combining frequency domain information with the features discussed under time domain should result in improved classification.

The pattern recognition results are encouraging but they must be tempered by recognizing that they are derived from one data sample. Additional input using data collected from a stress corrosion cracking test should do much to clarify the more general applicability of these results. This should provide

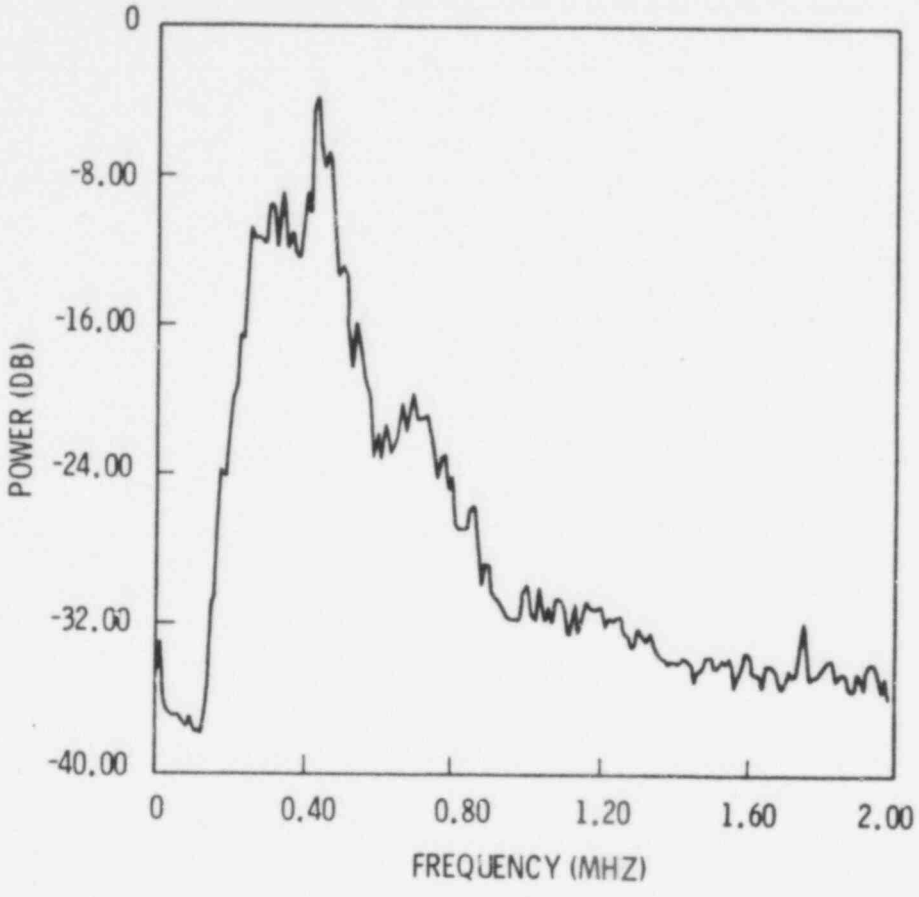

FIGURE 28. Average Power Spectrum - 148 AE - Waveforms

an interesting camparison between properties of AE signals generated by two significantly different failure mechanisms.

HIGH-TEMPERATURE AE SENSOR TESTING

Laboratory testing of high-temperature AE sensors in an oven at 550°F (288°C) continued through this report period. The sensors are being heated in an oven at 550°F (288°C) 24 hr a day Monday through Friday and then the temperature is dropped to RT through Saturday and Sunday. This cycle is repeated weekly. Accumulated test hours to March 31 are:

550°F (288°C) - 5400 hr
500°F (260°C) - 480 hr
320°F (160°C) - 194 hr
Room Temp. - 4500 hr

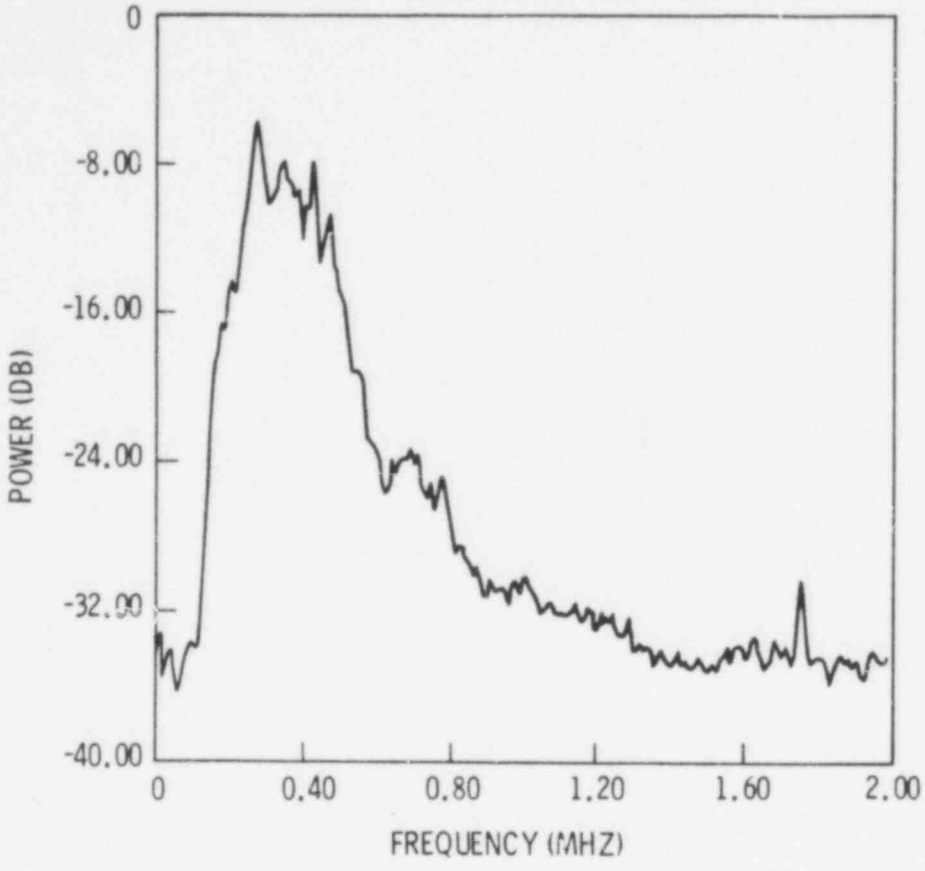

FIGURE 29. Average Power Spectrum - 75 Noise Waveforms

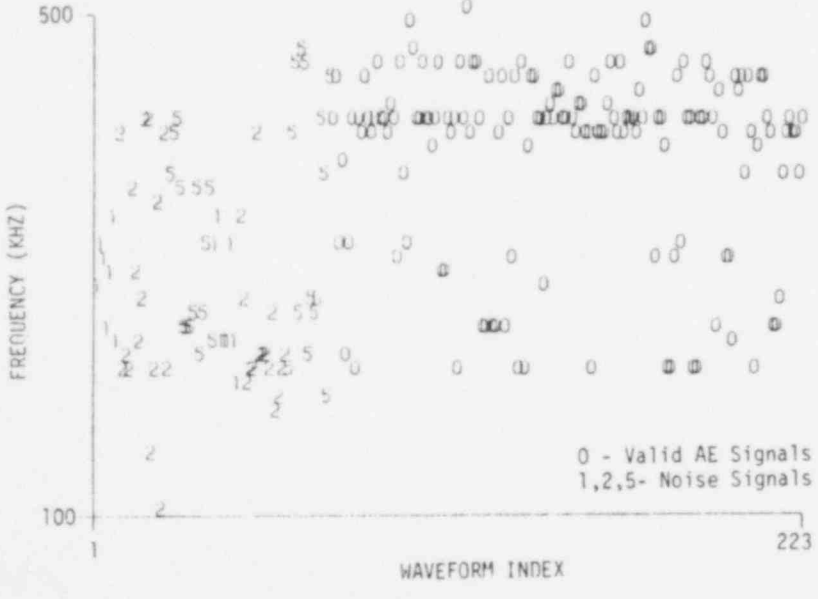

FIGURE 30. Point of Maximum Frequency Response for 148 Valid AE Signals and 75 Noise Signals

Sensors response was tested March 30 using a pulser input to the plate on which the sensors are mounted. Results of this are shown in Figure 31. Sensor A has been dropped from testing due to lack of sensitivity. The same identification format is used as in previous quarterly reports (Hutton, Schwenk, and Kurtz 1978c). Tables 7 and 8 show sensor response in μV and signal-to-noise (S/N) ratio respectively.

Sensor B is showing continued good response characteristics and they have not changed appreciably after nearly 5900 hr exposure to 500° to 550°F (260° to 288°C) temperature. Table 7 shows evidence of a more uniform response relative to frequency for sensor B, i.e., less change going from a 100 to 400 KHz high-pass filter. This is desirable because it helps reduce the ratio between lower frequency noise response compared to higher frequency AE response. Table 8 shows that both sensor B and the wave guide exhibit good signal to noise ratios above 400 KHz.

Installation of high-temperature sensors on the discharge face of Hanford's N-Reactor for environmental testing still awaits an appropriate outage. The necessary development test document has been submitted. We hope this can be accomplished during the summer maintenance outage.

REPORTS

The following reports were prepared during this period:

- quarterly progress report for the October 1 to December 21, 1978 period
- mid-year review report
- test program revision in response to mid-year review agreements.

WORK PLANNED FOR NEXT QUARTER

Work plans for the period April 1 to July 1, 1979 include:

- fracture test of weld metal at 550°F using a SN specimen
- FCG testing of weld metal at RT and 550°F using a SEN specimen
- initiation of a slag inclusion test

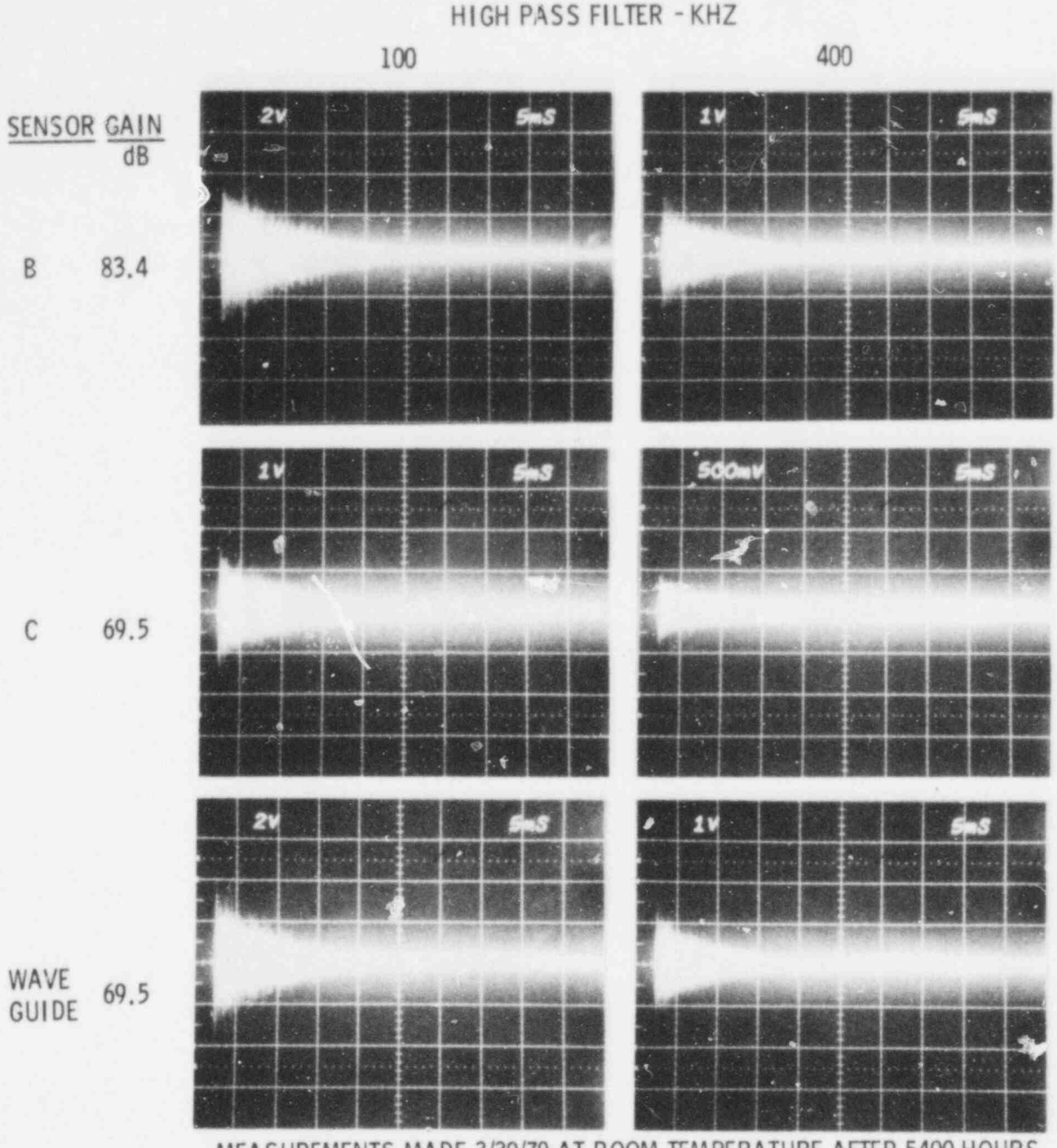

MEASUREMENTS MADE 3/30/79 AT ROOM TEMPERATURE AFTER 5400 HOURS AT 550°F (288°C)

FIGURE 31. HIGH TEMPERATURE SENSOR RESPONSE TO CONSTANT PULSE INPUT TO TEST PLATE

FIGURE 31. High-Temperature Sensor Response to Constant Pulse Input t Test Plate

TABLE 7. Response of High-Temperature AE Sensors Versus Frequency at RT(a)

Sensor	Gain dB	High-Pass Filter, KHz 100	400
B	83.4	257	101
C	69.5	553	167
Wave Guide	69.5	1541	56

(a) Sensor response referred to preamplifier input in μV.

TABLE 8. Signal-to-Noise (S/N) Ratio for High-Temperature AE Sensors at RT

Sensor	Gain dB	High-Pass Filter, KHz 100	400
B	83.4	7.6	6
C	69.5	5.5	2.9
Wave Guide	69.5	7.7	5.7

- AE monitoring of a stress corrosion cracking test in 4-in. Schedule 80 stainless steel pipe
- completion of fabrication of specimen and test facility for high temperature-pressure water test and initiation of testing
- initiation of development of a concept for an on-reactor AE monitor prototype
- continuation of investigation of pattern recognition techniques for AE signal classification.

REFERENCES

Adaptronics, Inc. 1978a. Development of Adaptive Learning Networks for Pipe Inspection. EPRI-NP-688, final report on Project 770, Electric Power Research Institute, Palo, Alto, California.

Adaptronics, Inc. 1978b. Feasibility of Using Adaptive Learning Networks for Eddy Current Signal Analysis. EPRI-NP-723, final report on Technical Planning Study 77-723, Electric Power Research Institute, Palo Alto, California.

Bryan, J. K. 1977. Signal Processing and Pattern Recognition of Ultrasonic Waveforms for the Nondestructive Evaluation of Materials. Report AFOSr-TR-77-0955, Air Force Office of Scientific Research, Bolling Air Force Base, Washington, D.C.

Hutton, P. H., E. B. Schwenk, and R. J. Kurtz. 1978a. "Acoustic Emission-Flaw Relationships for In-Service Monitoring of Nuclear Pressure Vessels." In Reactor Safety Research Programs Quarterly Report, January 1 - March 31, 1978, ed. J. L. Hooper, NUREG/CR-0086, PNL-2653-1, Pacific Northwest Laboratory, Richland, Washington.

Hutton, P. H., E. B. Schwenk, and R. J. Kurtz. 1978b. "Acoustic Emission-Flaw Relationships for In-Service Monitoring of Nuclear Pressure Vessels." In Reactor Safety Research Programs Quarterly Report, April 1 - June 30, 1978, ed. J. L. Hooper, NUREG/CR-0341, PNL-2653-2, Pacific Northwest Laboratory, Richland, Washington.

Hutton, P. H., E. B. Schwenk, R. J. Kurtz, and C. Pavloff. 1978c. Acoustic Emission-Flaw Relationships for In-Service Monitoring of Nuclear Pressure Vessels. NUREG-0250-3, BNWL-2232-3, Annual Report No. 1, Pacific Northwest Laboratory, Richland, Washington.

Rose, J. L. 1977. "A 23 Flaw-Sorting Study in Ultrasonics and Pattern Recognition." Materials Evaluation, July, pp. 67-92.

Tada, H., P. C. Paris, and G. R. Irwin. 1973. The Stress Analysis of Cracks Handbook. Del Research Corporation, Hellertown, Pennsylvania.

Ultrasonics International. 1978. Ultrasonic Pattern Recognition Study of IGSCC in SS Piping. EPRI-NP-891, interim report on Project 892-1, Electric Power Research Institute, Palo Alto, California

FUEL SUBASSEMBLY PROCUREMENT AND IRRADIATION TEST PROGRAM*

C. R. Hann, Program Manager
E. L. Courtright, Project Manager
P. L. Hendrick
A. G. Dunbar
R. R. Lewis
A. G. Couch
R. K. Marshall
D. D. Lanning
M. E. Cunningham

SUMMARY

Preliminary results from signal interferensce tests indicate that multiple-pin underwater connectors could be used to facilitate disassembly of multi-rod test train hardware.

Analysis of IFA-432 rods has shown that the temperature response (i.e., fuel centerline) to a step power change holds promise for confirming the partitioning of thermal resistance between fuel and gap. This technique could prove useful in analyzing fuel rod thermal response during the preconditioning phase of Power Burst Facility (PBF) experiments.

Preliminary evaluations indicate that a 25-rod BWR bundle could be substituted for the PWR assembly that was previously proposed as part of a multi-rod generic test train design concept. Modification of the upper and lower instrumentation assemblies would be required.

---

*RSR Fin. Budget No: B2043; RSR Contact: R. VanHouten

INTRODUCTION

The Fuel Subassembly Procurement and Irradiation Test Program has been divided into five tasks for fiscal 1979. The objectives of these are as follows:

- Task A: 4X Test Train Hardware Development. The primary purpose of this task is to develop underwater electrical connector devices for the instrumentation used in fuel rod irradiation experiments. Supplementary or replacement quadrants for Power Burst Facility (PBF) 4X Test Trains will be provided as needed.
- Task B: Gap Conductance Test Analysis. This task will be directed as providing the testing methodology for obtaining gap conductance data from a selected test in the PBF series. Post-test analysis and data interpretation of the experimental results will be provided.
- Task C: Dual Purpose Assemblies. This task covers the efforts associated with the experimental design, fuel rod fabrication, pre-characterization, and shipping of fuel assemblies irradiated in Halden and subsequently tested in a transient mode in the PBF.
- Task D: Multi-Rod Test Trains. The purpose of this task will be to design and build a multi-rod test assembly based on the generic design concept developed in Task E.
- Task E: Generic Test Train Design. The objective of this task will be to provide a conceptual design of a multi-rod irradiation test train for use in conjunction with NRC-sponsored programs. The test assembly will incorporate features designed to support experimental testing in any of the following reactors: PBF, NRU, SGHWR, BR-2, and ESSOR.

4X TEST TRAIN HARDWARE DEVELOPMENT

The task of designing a multi-rod test assembly has focused attention on the need for an underwater electrical connector. Connectors would allow the use of modular instrumentation packages and enable poolside disassembly of the

test train. Work this quarter has been directed at qualifying connector cross talk and evaluating compounds for sealing exposed cable ends.

CONNECTOR QUALIFICATION

Signal interference tests were performed[(a)] to determine the interference in the sensor circuit caused by the addition of a connector. These tests included AC coupling into DC circuits, AC coupling into other AC circuits and DC coupling into other DC circuits. The tests were conducted at room temperature and at 650°F and in both laboratory and autoclave environments. The tests on low-pressure connector were only performed in the laboratory at room temperature and not in an autoclave or at elevated temperatures.

The following results were observed for the high-temperature, high-pressure connector:

AC-to-AC Coupling: Two to three millivolts (rms) of interfering frequency could be measured between wire and sheath. None was observed in the control cable without a connector. This level of interference is considered relatively minor and can be substantially improved with differential input signal conditioning.

An induced signal level of 70 μ microvolts (rms) was also measured differentially between wires. These signals are small and are not expected to cause interference errors.

AC-to-DC Coupling: The AC coupled magnitudes were approximately the same as for the AC-to-AC case, but were not large enough to cause significant error. Also, filtering can be placed in most DC signal conditioning to remove the interference to insignificant levels.

DC-to-DC Coupling: Coupling between circuits using a variable 4 to 17 volt DC power supply was less than 3×10^{-9} amps at 650°F and 10^{-13} amps at room temperature. These current levels are not expected to induce error in a self-powered neutron detector circuit.

(a)This work is being done by the Instrument Technology Section of the Hanford Engineering Development Laboratory operated by Westinghouse Hanford Company, Richland, Washington.

Similar tests performed on the low-pressure, 30-pin connector gave results as follows:

DC-to-DC Coupling: As in the high-pressure case, the coupled currents were insignificant.

AC-to-DC Coupling: The coupled AC signal can be removed from the DC circuit in most applications to achieve insignificant error.

AC-to-AC Coupling: In general, the maximum coupled single-ended voltage was in the 3-millivolt range for the cable with the connector and about 1.8 millivolts for a cable without a connector. Both of these voltage levels may be reduced to a small value using differential input signal condition.

There is a potential problem with the attachment cable for AC circuits, however, because the wires were not shielded twisted pairs; and, thus, limited improvement would be expected if differential input signal conditioning was used.

CABLE SEALANT EVALUATIONS

An important part of building a connector junction is the ability to re-establish a moisture-proof seal at the end of each cable after it has been cut and wires exposed. Both the initial sheath and protective ceramic insulation are normally stripped for an inch or more to expose the conductor wires. This step is necessary for purposes of rejoining the wires to connector pins or for splicing. Moisture will rapidly diffuse into the ends of the cable because the ceramic insulation is porous. Significant amounts of moisture can seriously degrade the high electrical resistivity that originally exists between conductor pairs or between a conductor and the sheath.

The sealant used for repairing the damaged cable end must meet the following requirements:

- It must form an impermeable seal to moisture.
- It must withstand temperatures up to 650°F.
- It must be resistant to thermal cycling and shock because, if it cracks, it will provide pathways for moisture penetration.

- It must have good dielectric properties at all temperatures up to and including a 650°F operating temperature.

Four sealing compounds are currently under evaluation. These are:

1. Polyimide 2080D (an aromatic, fully imidized and polymerized polyimide made by the Upjohn Company.
2. Westinghouse A508 Glass Frit (a product of VitriFunctions, Greensburg, Pa).
3. Dow Corning 803 (a moisture resistance silicone paint resin made by Dow Corning).
4. AerOseal (a patented high temperature sealant made by ARi Industries, Inc.).

Since moisture contamination is basically a diffusion controlled process, the degradation of insulation resistance with time is a concern. Ongoing tests are being performed to determine the change in resistance of sealed cable ends exposed to ambient conditions. Current data for each of the four compounds compared against an unsealed reference cable are shown in Figure 1. A rapid decline in resistance has been observed in three of the four sealants after ten days of exposure. In contrast, the AerOseal cable maintained its high initial value for 85 days. A sharp decline to 10^{11} ohms was observed between 85 and 90 days but seems to have leveled off at 92 days. The reason for this behavior has not yet been determined. Also, the uncertainty in the resistance measurement has not been calculated and may be large. At this point in the study, only the relative trends are of principal interest.

GAP CONDUCTANCE TEST ANALYSIS

Suggested criteria for gap conductance tests during the pretransient phase of PBF tests were reported in Reactor Safety Research Programs Quarterly Report, April 1 - June 30, 1978 (Hooper 1978). Additional ideas on the use and analysis of short "step" power drops for obtaining composite fuel rod thermal resistance information are presented below.

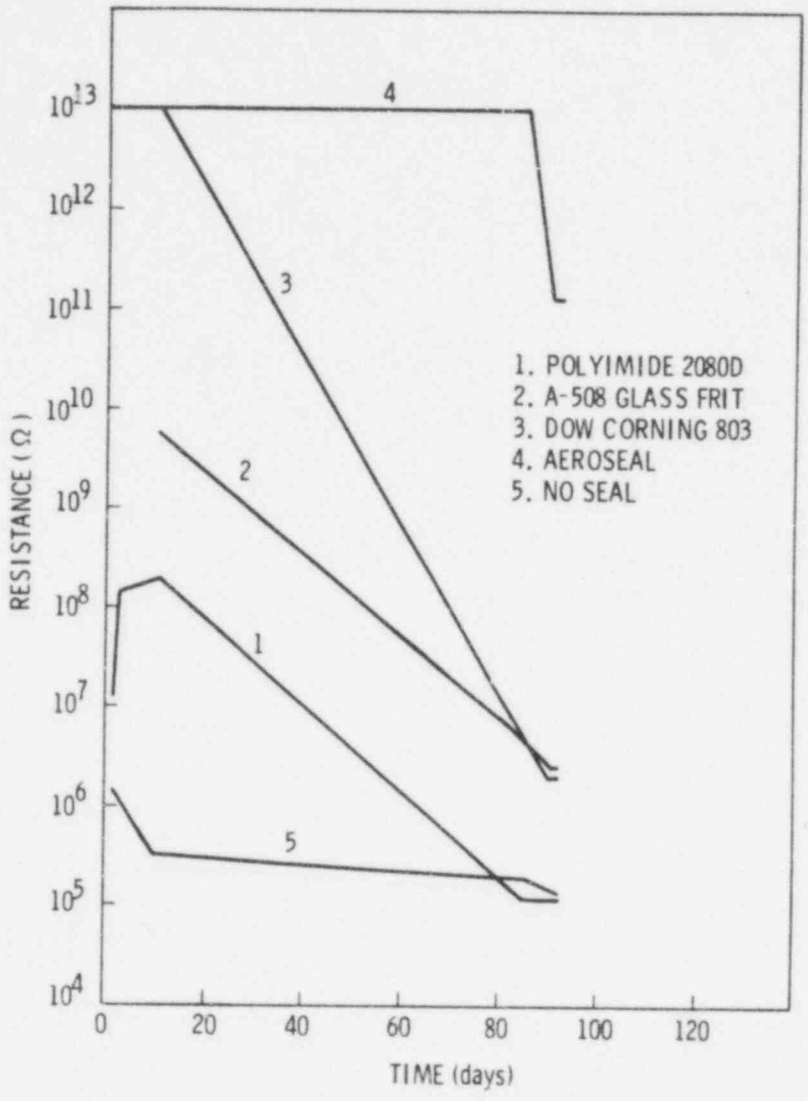

FIGURE 1. Conductor - Conductor Resistance Change as a Function of Shelf Life for Four Sealing Compounds

For an idealized fuel rod, which has no temperature dependence in its thermal parameters, the temperature response to a pure step power decrease would be an exponential fall to a new steady-state level. In fact, the final normalized temperature, T_N, will equal the final normalized power, P_N, where

$$T_N = \frac{T_{fuel} - T_{coolant}}{T_{fuel}^{initial} - T_{coolant}}$$

$$P_N = P/P^{initial}$$

Given the above relationships, the idealized transient behavior will be summarized as

$$T_N(t) = T_N^{final} + (1 - T_N^{final})\, e^{-\alpha t}$$

or $$-\ln (T_N - T_N^{final}) = A + \alpha t$$

In a previous quarterly report (Hooper 1978), we presented calculated plots of $-\ln (T_N - T_N^{final})$ versus time for rods of varying resistance and showed that significant variation in slope, α, could be expected.

For real rods, the thermal parameters are temperature dependent, and one consequence is that $T_N^{final} \neq P_N^{final}$ in general.

Consequently, a better variable choice for comparative plots of real data is $-\ln (T_N - a)$, where $a = P_N^{final}$. Recent calculations with GAPCON-3 show that $-\ln (T_N - a)$ versus time is still quite linear for all types of rods over a restricted time range, and also that its slope (curvature) is not strongly affected in this range by the thermocouple time constant. This is of considerable importance in data interpretation because, in ordinary plots of T_{fuel} versus time, the thermocouple time constant severely alters both the magnitude and the curvature.

Finally, we have concluded that fuel transient temperature data will have considerably more use than simply to confirm the apparent resistance[(a)] behavior of various fuel rods. The temperature response to step power changes holds promise for confirming the proper partition of resistance between fuel and gap. Note that steady-state resistance can be explained (matched) by a very broad range of fuel conductivity and gap conductance functions. For

---

(a)The resistance referred to here is the measured (centerline) fuel temperature minus coolant temperature, divided by the associated power.

example, consider the resistance behavior sketched in Figure 2. Using Lyons (1964) fuel thermal conductivity equation and a constant gap conductance, h_{gap}, GAPCON-3 (or any code) could be forced to match the behavior of the "gap-dominated" rod by making the adjustments noted in Table 1. Notice the tremendous range of (constant) gap conductance values that can be envisioned

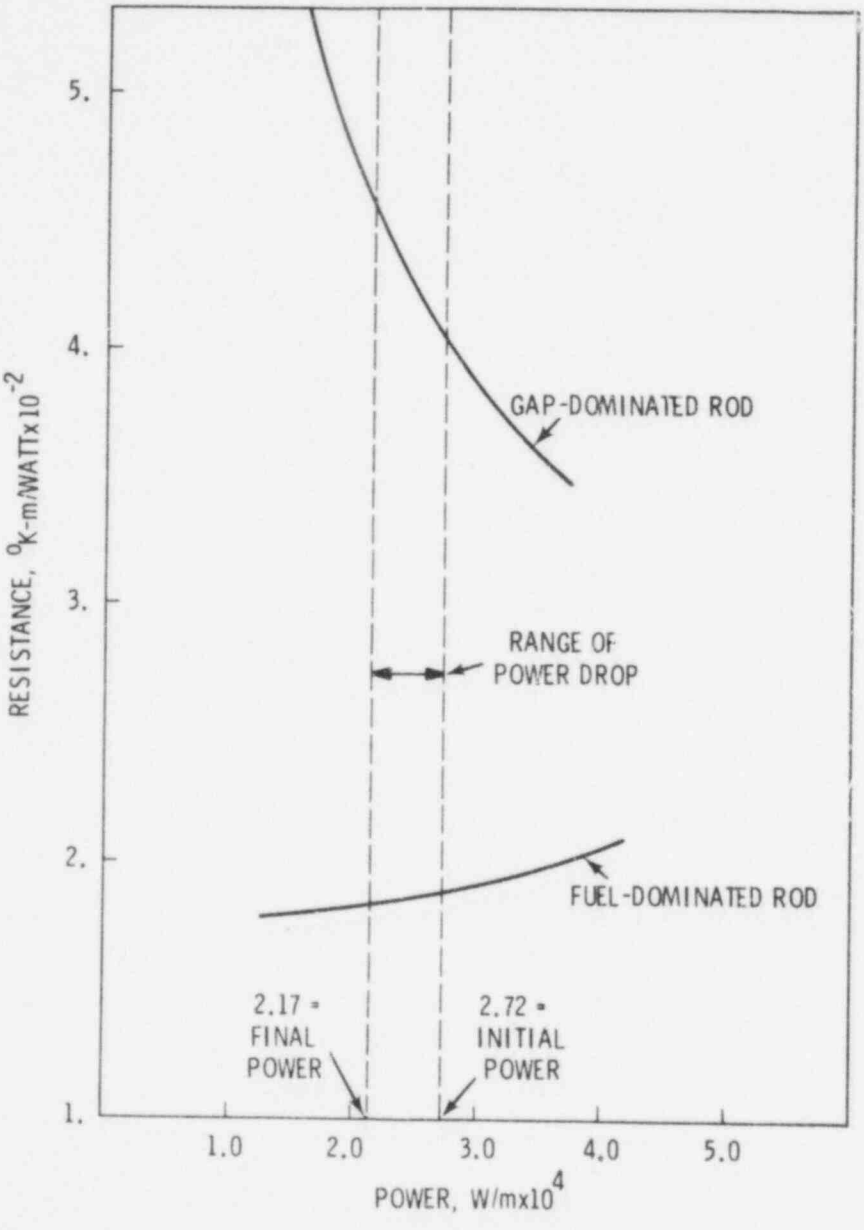

FIGURE 2. Typical Resistance Versus Power Behavior

TABLE 1. Test Cases for Gap Dominated Rod(a)

Case #	h_{gap}, kW/m^2°K	A	B
1	1.0	-8.7	.0096
2	2.0	-1.8	.0027
3	3.0	-1.1	.0020
4	10.0	-0.9	.0017

(a) The fuel conductivity in these cases is given by

$$K_{fuel} = K_{Lyons}^{(T)} \text{ times } (A + \overline{BT}),$$

where $\overline{T}$ is the volume average temperature in °C.

The gap conductance is held constant throughout the transient (commensurate with cracked and relocated fuel).

if one permits the modifier ("a crack factor") to adjust the fuel conductivity, as noted.

Now all four partitions of resistance noted in Table 1 match the resistance versus power behavior exactly, within the range of the 20% power decrease. But the corresponding calculated transient temperatures, shown in Figure 3, are quite different. Comparison to actual data will define a narrow range of resistance partition that is truly reasonable for a particular rod. This should aid immensely in data interpretation and fuel rod modeling.

GENERIC TEST TRAIN DESIGN

The multi-rod test train design concept for use in studying fuel rod interactive effects under off-normal transient conditions has been proposed (Hendrick 1979). This design concept selected a 32-rod 17x17 PWR size fuel

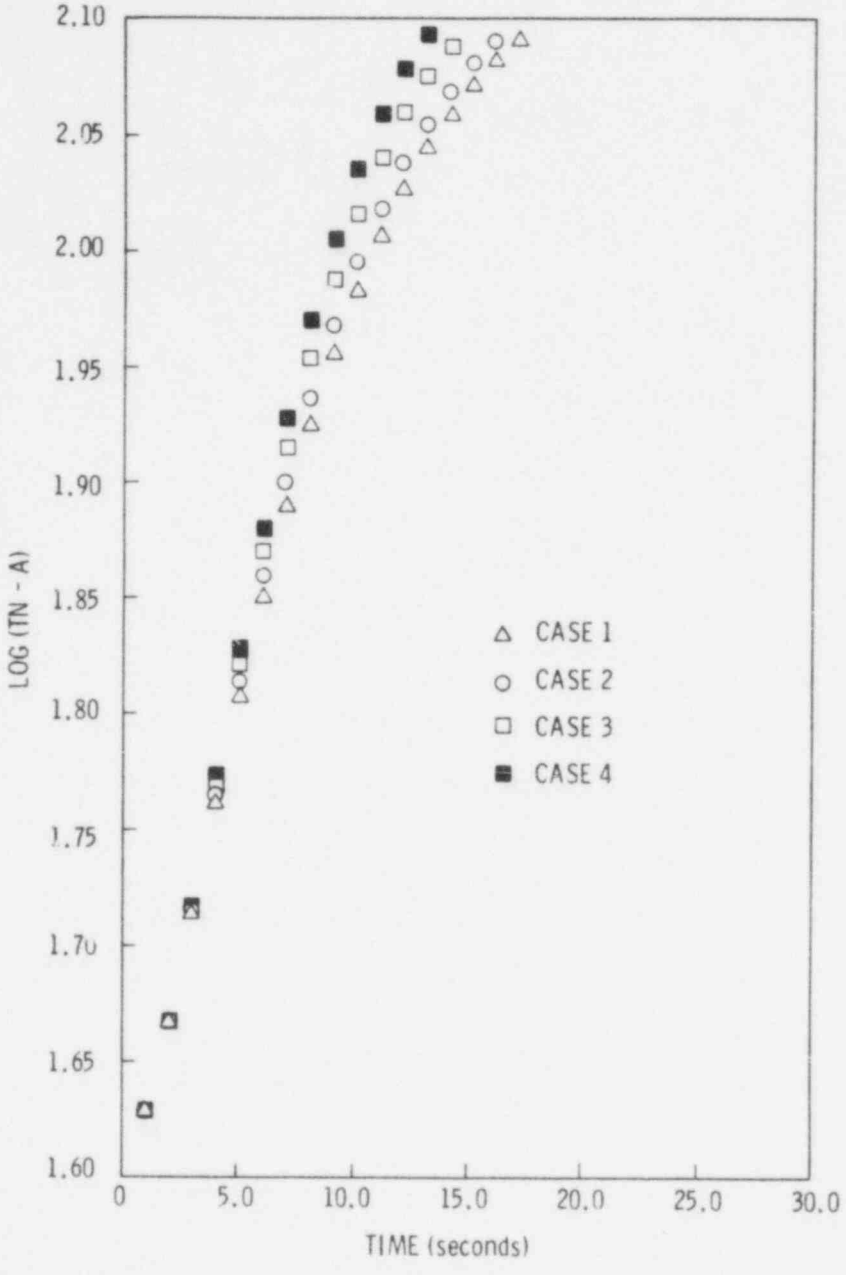

FIGURE 3. Calculated Transient Response for the Fuel Rod Parameters in Table 1

array as the principal bundle configuration. Although suitable for most basic studies of accident categories, this array cannot accurately represent some BWR hydraulic or flow limiting conditions. An evaluation was thus initiated

to determine the feasibility of developing an interchangeable BWR bundle configuration which could fit into the same basic test train assembly.

An 8x8-type BWR rod size and pitch configuration was selected to maximize the number of rods which could fit within a given test space. A 25-rod (5x5) bundle as shown in Figure 4 will fit within four of the five selected reactors. In NRU it would be necessary to adopt a 16 or 21 (5x5-4) rod bundle having 4 or 5 test rods, respectively. The decision was made to adopt the 25-rod bundle, which has a 9 test rod core section and 16 peripheral rods. This configuration maximizes the number of test rods and will fit within most of the facilities considered. In view of BWR two-phase flow conditions, it may be desirable in some instances to convert the shroud outlet flowmeter to a recombined flowmeter. Several changes would be required to accomplish this as follows:

- Cut bypass inlet ports into the upper instrumentation assembly below the flow straightener.
- Cause flow to exit the upper instrumentation assembly through the hanger tube instead of around it with outlet ports in the hanger tube section immediately below the closure head.

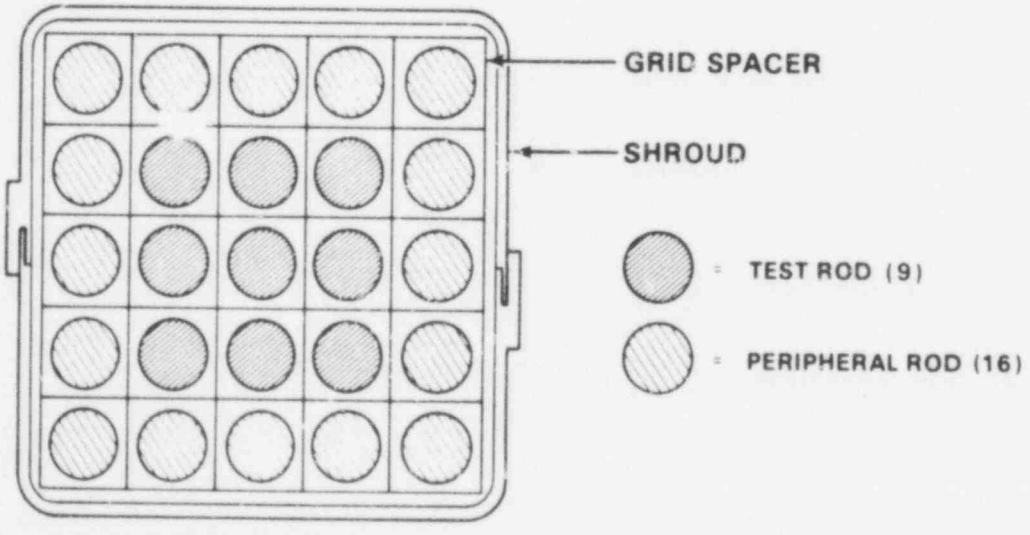

FIGURE 4. 25-Rod, BWR-Size, Test Array

- Add an upper flow restrictor around the hanger tube and below the hanger tube outlet ports to insure that shroud bypass flow goes through the recombined flowmeter.

The objective of the recombined flowmeter would be to derive heat balance data under two-phase conditions by allowing sufficient shroud bypass flow to quench the shroud outlet and permit measurements under single-phase fluid conditions. The recombined flowmeter could be viewed as an option if item (b) above were implemented. Then the addition of item (a) and (c) would convert the flowmeter to the measurement of recombined flow.

Most other aspects of the BWR design would be similar to the previous PWR generic design. Since there are fewer test rods (i.e., 9 instead of 12) a somewhat higher density of instrumentation would be permitted (e.g., 9 elongation detectors instead of the 6 allowed in the PWR design).

FUTURE PLANS

Task A: 4X Test Train Hardware Development

A detailed analysis of the connector qualifications performed to date will be completed and a report issued. The prospects of building connectors commercially will be explored. Industry technology and manufacturing capability will likely require design modifications. These potential modifications will be combined with recent knowledge obtained from in-house test and fabrication experience to generate a third generation design. Follow-on testing will also be performed as required.

Purchase requistions for 4X test train hardware components will be issued. Fabrication of four fully instrumented quadrant assemblies is planned. Two high-pressure connector units will be added to each quadrant for purposes of obtaining in-reactor qualification data.

Task B: Gap Conductance Test Analysis

A technical liaison with members of the EG&G experimental staff has been established. Analytical support and technical inputs will be supplied as requested. Work progress will depend upon PBF test schedules and priorities.

Task C: Dual Purpose Assemblies

The IFA 513 assembly is currently under irradiation in Halden. No further work is planned until this assembly is ready for discharge.

Task D: Multi-Rod Test Trains

The feasibility of adapting the basic generic design concepts to a nine-rod cluster assembly suitable for OPT 1-3 and RIA 1-7 experiments in PBF will be evaluated.

Task E: Generic Test Train Design

Meetings with the engineering staffs at ESSOR and SGHWR will be held to assess the feasibility of implementing the generic test train concept. Further conceptual work on the BWR version of the generic test train will depend upon the results of discussions with SGHWR staff personnel and future programmatic needs.

REFERENCES

Hendrick, P. L. 1979. Concept for Generic Multi-Rod Test Train. PNL-2908, Pacific Northwest Laboratory, Richland, Washington.

Hooper, J. L., ed. 1978. Reactor Safety Research Programs Quarterly Report, April 1 - June 30, 1978. NUREG/CR-0341, PNL 2653-2, Pacific Northwest Laboratory, Richland, Washington.

Lyons, M. F., et al. 1964. UO_2 Pellet Thermal Conductivity from Irradiation with Central Melting. GEAP-4624, General Electric Atomic Power, Sunnyvale, California.

STEAM GENERATOR TUBE INTEGRITY*

R. A. Clark, Project Manager
V. F. FitzPatrick, Deputy Project Manager

J. M. Alzheimer
G. H. Lyon
C. J. Morris
K. R. Wheeler

SUMMARY

The program operated on an expanded scope starting this quarter with the introduction of a large number of tasks related to transporting a retired surry steam generator to Hanford. Phase II activities of the original program continued at a slowed rate due to initial difficulties in both preparation and nondestructive characterization of stress corrosion cracked specimens.

INTRODUCTION

A laboratory program is underway at the Pacific Northwest Laboratory (PNL) to develop validated models, based on experimental data, for prediction of margins-to-failure under burst and collapse pressures of steam generator tubing found to be service degraded by eddy current inservice inspection. The program is a multi-task effort to achieve the desired objectives. Included are burst and collapse tests at reactor operating temperatures of tubes having mechanically or chemically placed defects simulating those found in service. These controlled defects are subject to full nondestructive characterization by serveral techniques to evaluate the accuracy of the various nondestructive testing methods. Finally mathematical modeling, on a statistically valid defected tubing sample, is used to develop formula relating remaining tube

---

*RSR Fin. Budget No. B2097; RSR Contact: J. Muscara

strength to actual defect type and extent. Comparison of eddy current indicated defects with actual defects then allows predictive margins of remaining tube life based on inservice inspection eddy current indications of tube degradation.

TECHNICAL PROGRESS

Following is a description of progress during this reporting period.

BURST AND COLLAPSE TESTING

Three intergranular attack, one chemically induced elliptical wastage, and all stress corrosion cracked specimens remain to be tested. All other mechanically and chemically defected specimens have been tested. No testing was conducted this quarter because insufficient specimens were available.

STRESS CORROSION CRACKING

A new system to produce stress corrosion cracked (SCC) Inconel 600 steam generator tubing was brought on line during the quarter. The system is shown schematically in Figure 1. It consists of a 4.2-liter nickel 200 autoclave with appropriate temperature and pressure controls. The head of the autoclave is fitted with nine penetrations. Two penetrations are for control thermocouples and seven allow penetration of 0.25-in. pressure tubing into the autoclave. Specimens consist of 12-in. lengths of steam generator tubing with a plug welded on one end and a transition piece and length of 0.25-in. tubing on the other. The specimens are prefilled with deionized water and attached to the autoclave head by passing the 0.25-in. pressure tubing through the head pressure fittings. The specimens are then lowered into the autoclave which has been prefilled with a charge of copper-saturated sodium hydroxide (6 g CuO + 0.5 g Cu metal dust + 600 g NaOH per liter of water). The autoclave is heated to 300°C for the stress corrosion cracking process. After reaching 300°C the tube specimens are water pressurized to ~90% of their 300°C yield strength through a common manifold, taking into account the equilibrium pressure of the heated hydroxide solution in the autoclave. Pressure is

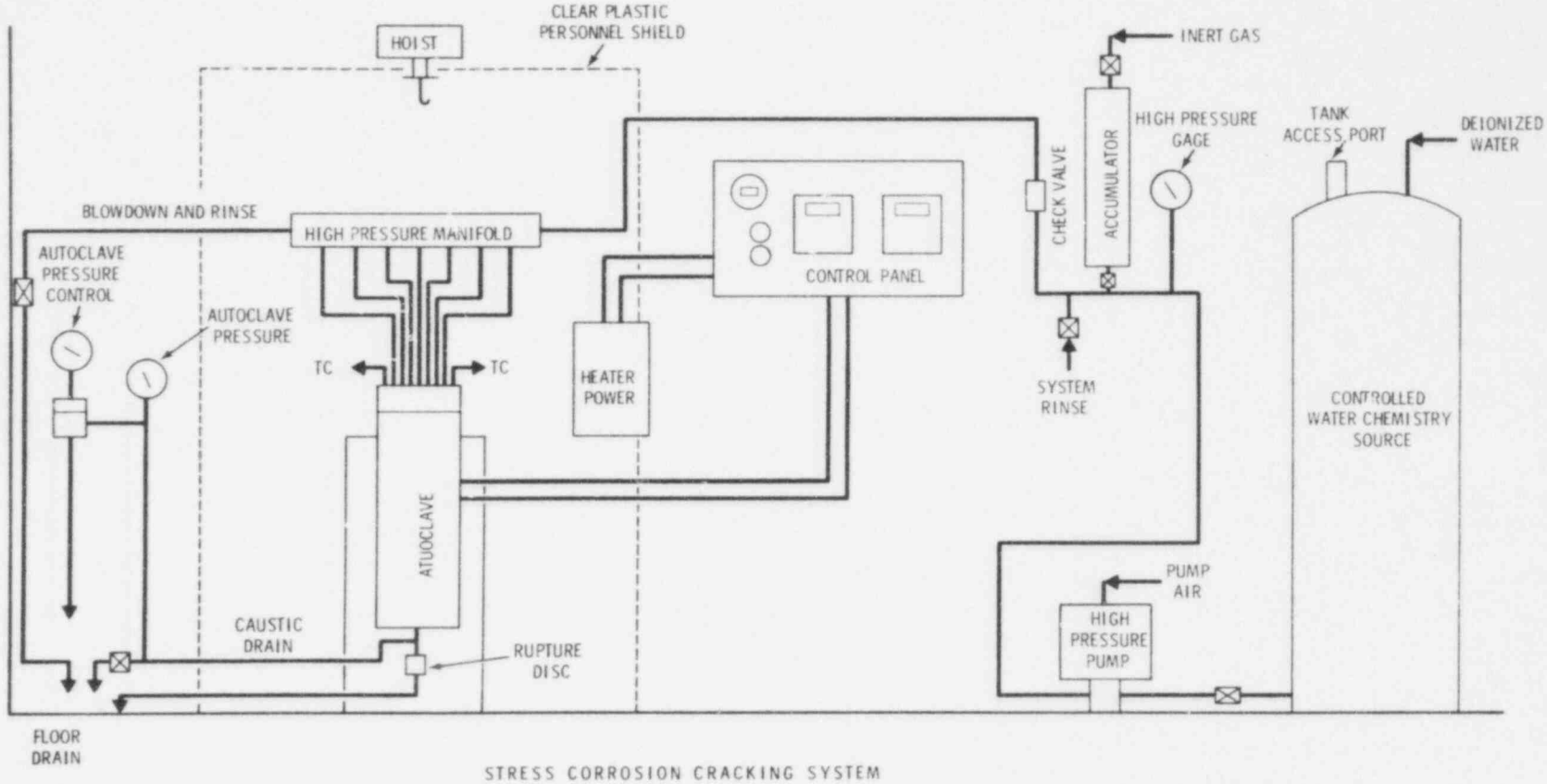

FIGURE 1. Stress Corrosion Cracking System, Employing Ni 200 Autoclave to Induce Stress Corrosion Cracks in Inconel 600 Tubing

maintained by an inline accumulator. Upon developing a through-wall stress corrosion crack in any one specimen, the stress on all other specimens is relieved as the autoclave and all specimens reach equilibrium pressure stopping further stress corrosion cracking of remaining tubes. The autoclave is then shut off. The resulting specimens have a random distribution of crack depths. Crack location is controlled by appropriate masking with shrink-fit Teflon tubing and Teflon tape.

A typical specimen is shown in Figure 2. An autoclave run can be conducted every alternate day resulting in about 15 to 18 specimens during a work week.

Detection of stress corrosion crack initiation and growth in BWR pipe welds is a major concern. A test loop has been established which allows crack detection instrumentation and techniques to be evaluated on welded piping up to 4 in. diameter. The loop operates under BWR pressure, temperature and water chemistry conditions. Waterflows through the specimen section to 100 gpm are achievable. The specimen section has an axial loading capacity of 20 T. Initial tests duplicate the General Electric 135 of 550°F yield strength cyclic load. Instrumentation being evaluated includes accoustic emission and an internal friction device manufactured by Daedalean. Figure 3 shows the specimen-loop setup.

NONDESTRUCTIVE TESTING

Current phase nondestructive examination consists of conventional single frequency and multi-frequency eddy current inspection for evaluation of chemically induced corrosion defects in steam generator tubing. To date sixty chemically degraded specimens have been inspected and evaluated using these eddy current techniques. The major effort this quarter was attempting to establish a sound nondestructive analysis of steam generator tubing sections having several stress corrosion cracks. Eddy current signals could not be interpreted on these multiple-cracked samples. As an alternate means of nondestructive analysis, radiographic tomography was explored. This technique is under development at Los Alamos Laboratories by Dr. Roger Morris and associates. A subcontract was let to Dr. Morris for analysis of one multiple stress

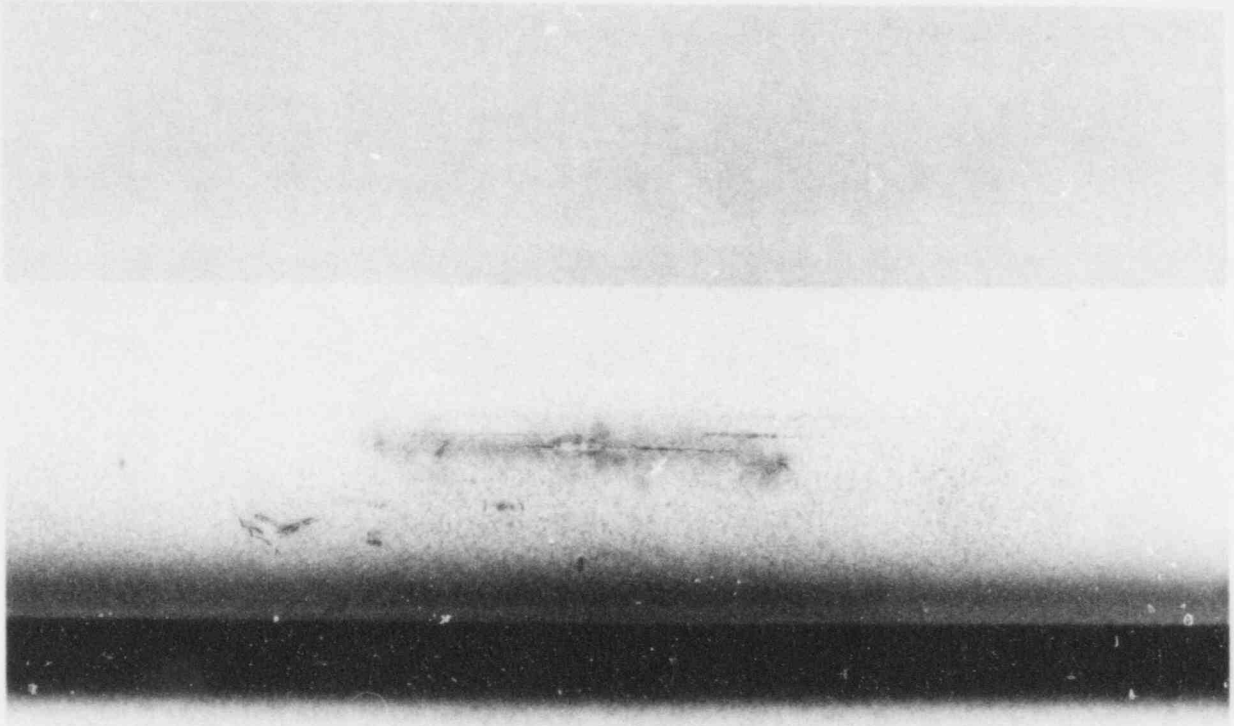

FIGURE 2. Typical Stress Corrosion Cracked Specimen Produced

corrosion cracked Inconel tube. His preliminary results show that a large amount of information can indeed be obtained using radiographic tomography. Crack lengths and depths can be determined. Los Alamos is currently destructively characterizing the tube to analyze the resolution and reliability of their technique. Initial PNL analysis of radiographic tomography indicates the technique will give detailed information on stress corrosion cracked tubes. However, considerable development work on instrumentation remains before the technique is practical. The current level of instrumentation would require two to three months for total characterization of a single specimen. We are currently seeking other nondestructive testing techniques for stress corrosion cracked tube characterization.

A pitting sample was developed using a grit blas machine in order to determine the sensitivity of the single-frequency 400 kHz eddy current test to small single pits in steam generator tubing. The pitting work showed that flaws typically under 40 of the wall thickness in depth are not detectable using conventional single frequency techniques.

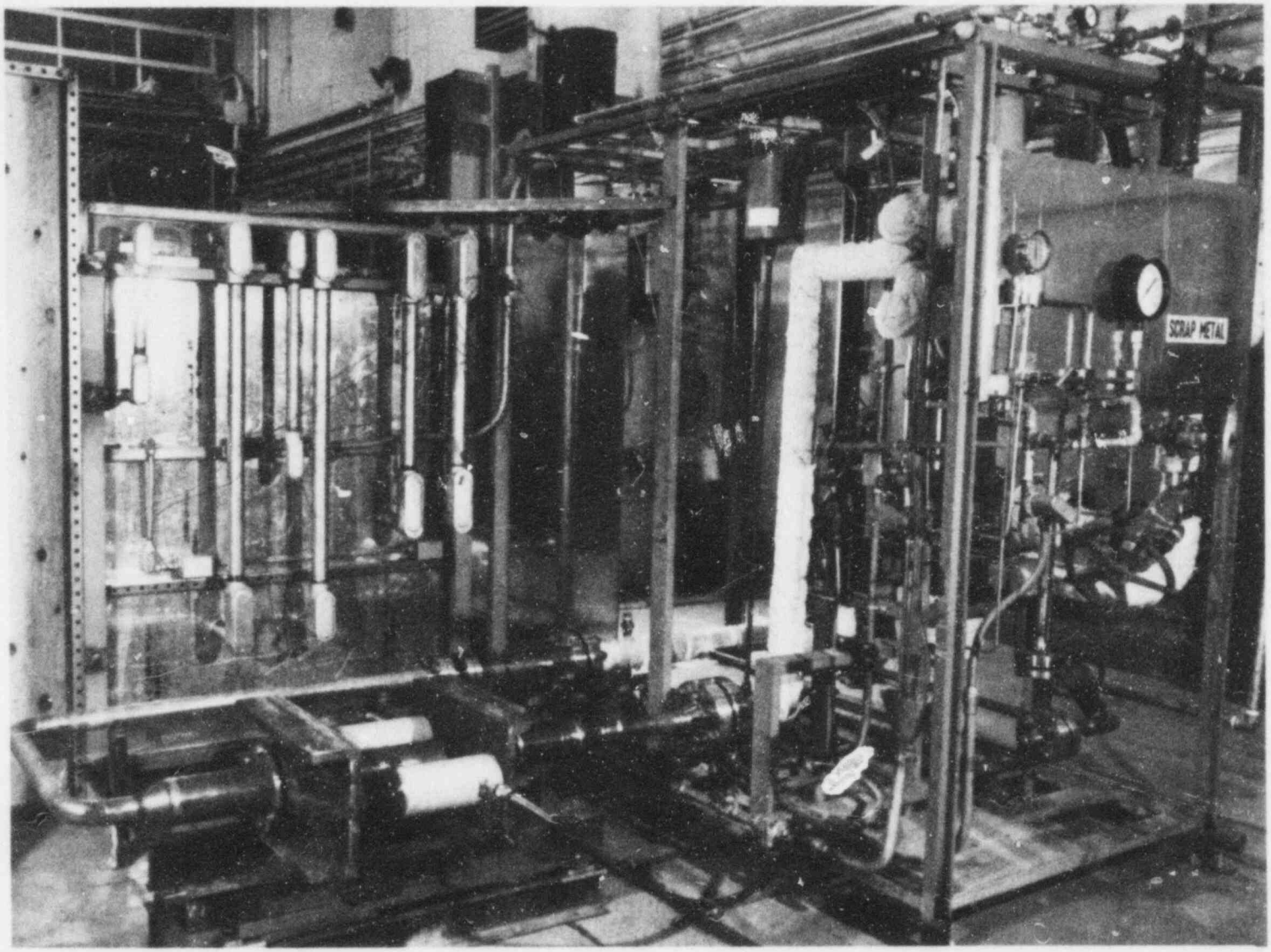

FIGURE 3. Loop for Conducting Stress Corrosion Testing of Welds on 4-in. Pipe Axially Loaded to 135% of Yield Under BWR Conditions

MATHEMATICAL MODELING AND DATA ANALYSIS

A re-evaluation of the burst data to provide refined mathematical relationships of failure pressure to defect type and extent is underway. The refined analysis will not significantly alter the form of the existing relationships, but will provide a statistically optimized evaluation of the data. Similarly an analysis of collapse data is underway to develop mathematical curve-fitting relationships.

Scoping studies have been initiated to evaluate the use of spectrum analysis and other vibrational methods for the examination steam generator tubing. Analysis of rather simple models indicated that changes in natural frequencies and mode shapes of the tubing may give an insight into the types of degradation present.

STATISTICAL ANALYSIS

The eddy current and tube failure data developed in Phase I on mechanically defected tubing were forwarded to Robert Easterling of Sandia Laboratories. Dr. Easterling is conducting a program for the Division of Operating Reactors, Nuclear Reactor Regulation, on a "Statistical Assessment of Steam Generator Tube Degradation." Our data are the first available that represent a statistically valid sample according to Dr. Easterling's analysis.

SURRY GENERATOR MOVE

FEASIBILITY STUDY

A feasibility study on transporting an out-of-service nuclear steam generator to Hanford Washington from Surry, Virginia or Turkey Point, Florida nuclear plants was completed. The study was conducted by Olympic Engineering under subcontract to PNL and by PNL. The conclusions reached were that retired nuclear generator could be transported to Hanford from either site and that exclusive cargo via barge was the preferred mode of transport. We also determined that no existing Hanford facility could handle a vertically positioned generator, and that a new facility to house the generator would be

economically preferable to an extensively modified existing structure. A preconceptual design of the generator housing facility was drafted as a basis for future work. Upon NRC recommendation that a Surry generator was more desirable, being a unit common to more operating plants, costs and schedules were determined for establishing the generator in a facility at Hanford ready for destructive examination.

ALTERNATE SITE STUDY

As an adjunct to the feasibility study, an alternate site study was conducted. This study was to determine the cost and technical effectiveness of placing a Surry generator for nondestructive/destructive analysis at various government laboratories besides Hanford. The study evaluated existing as well as new facilities at alternate sites. Also considered was transport feasibility. In addition an appraisal of scientific support capabilities was conducted. The conclusions and comparative cost analysis of this study will become available during the next quarter.

ADDITIONAL ACTIONS

In anticipation of an expanded program including examination of a retired Surry Generator, PNL has established a management and financial structure appropriate to the needs of this complex undertaking. Department of Energy, Richland Office, personnel have been kept informed of our intent to propose an expanded Steam Generator Tube Integrity Program so that an appropriate NRC-DOE-RL liason could be established.

MILESTONES

- Nearly all Phase II chemically defected tubes except those with stress corrosion cracks have been nondestructively evaluated and tested.
- Stress corrosion cracking of Inconel 600 steam generator tubing is currently being conducted.

- The Phase I topical report was completed and transmitted to NRC for publication.
- A feasibility study on shipping a retired nuclear steam generator to Hanford for nondestructive and destructive examination was completed.
- The use of x-ray tomography to characterize stress corrosion cracks in steam generator tubing was examined.
- A 4-in. pipe stress corrosion cracking experifment was started to evaluate the ability of internal friction measurements to determine crack initiation and growht in the weld heat affected zone.

PROBLEMS

No definitive existing methcd has been found that can be used to nondestructively characterize multiple stress corrosion cracks in Inconel 600 steam generator tubing. Potential methods are forefront technology efforts requiring funding and research for equipment development/optimization.

CORE THERMAL MODEL DEVELOPMENT*

D. S. Trent, Program Manager
M. J. Thurgood, Project Manager
T. L. George
J. M. Kelly
J. M. Cuta
K. L. Basehore

SUMMARY

A simulation of Semiscale MOD3 test S07-6 has been made out to a transient time of 50 seconds. The simulation is in reasonable agreement with the measured data for this period of the transient. The new rod model has been used to perform simulation of FLECHT reflood experiments. The resulting data comparisons are quite encouraging. Finally, the coupling of COBRA-TF with TRAC is well underway. The combined version is expected to be operational early in the next quarter.

INTRODUCTION

This work is being conducted as part of the NRC Water Reactor Safety Research Program in the area of analysis development. The purpose of this work is to provide better digital computer codes for computing the behavior of full-scale reactor systems under postulated accident conditions. In particular, COBRA-TF is being developed as a component code to be used for the detailed analysis of the hot bundle and/or hot channel of a reactor core during postulated transients. COBRA-TF will use time-dependent boundary conditions computed by the Los Alamos Scientific Laboratory developed systems code TRAC and must, therefore, be compatible with TRAC output.

---

*RSR Fin. Budget No: B2041; RSR Contact: S. Fabic

In addition, COBRA-TF has a high-priority goal of providing a Semiscale system upper head injection (UHI) simulation capability for use by Idaho Nuclear Energy Laboratory in evaluating Semiscale-MOD3 UHI test planning and results. The COBRA-TF vessel model will be incorporated into TRAC to provide a UHI system simulation capability. The application of the full-vessel capability to the analysis of UHI-equipped PWR's and UHI experiments will continue.

The results of the Semiscale-MOD3 simulation will be presented first, followed by the results of bottom reflood simulations and then an update on the COBRA/TRAC coupling progress.

SEMISCALE MOD3 SIMULATION

Semiscale MOD3 test S07-6 was simulated with COBRA-TF to assess the code's ability to simulate the measured behavior of the system. Results of the simulation are being used to improve the physical models in COBRA-TF and to improve the nodalization of the Semiscale MOD3 facility.

The MOD3 vessel and downcomer were modeled by dividing them into twelve axial regions (Figure 1). A minimum number of subchannels was then placed in each region to model the main flow paths. A minimum number of subchannels was used so that the basic behavior of the system could be studied at a reasonable cost. Experience with this model is expected to point out areas which require a more detailed nodalization to realize better comparison with the measured data. The number of subchannels used to model each section is shown in Figure 2, as are the simulated heat transfer surfaces, which are designated by an "R" before the number. For example, R1 and R2 model the high- and low-powered fuel rods, respectively, in Section 3; while R5 is the vessel wall and R6 the downcomer wall. The fluid in this section is modeled by a single channel in the core, channel 5, and a single channel in the downcomer, channel 6. The axial node length is 0.5 ft. The number of nodes in each section is also indicated in Figure 2.

Measured volumetric flow rates and enthalpies were specified at both hot legs and the intact loop cold leg. The measured pressure and enthalpy were

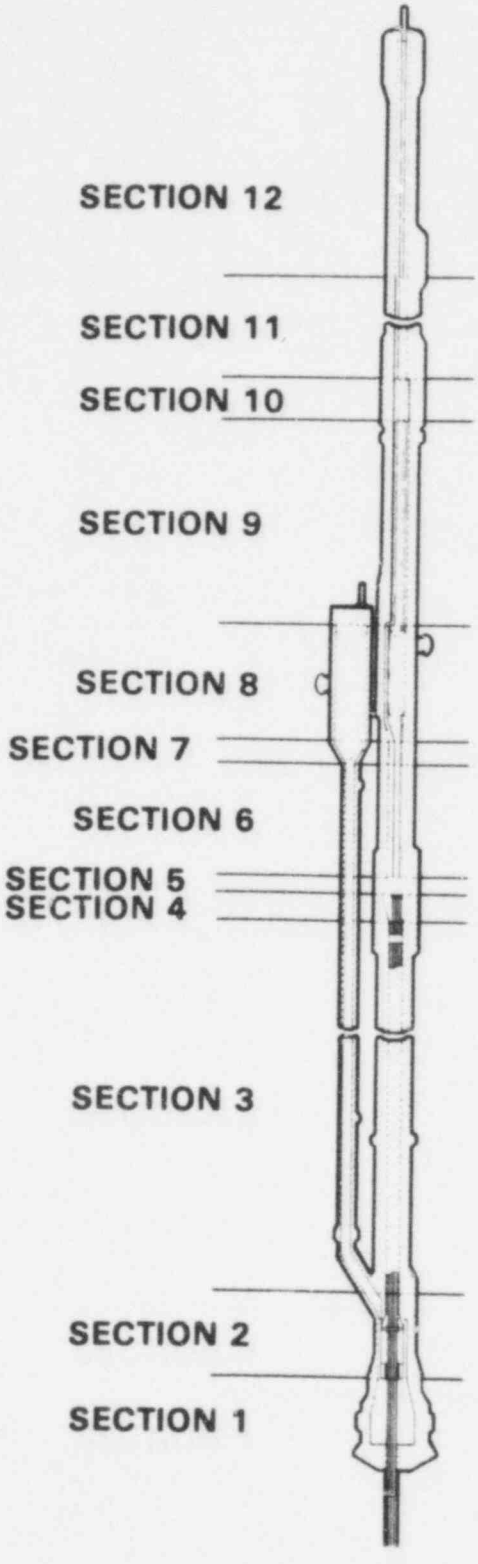

FIGURE 1. Semiscale MOD3

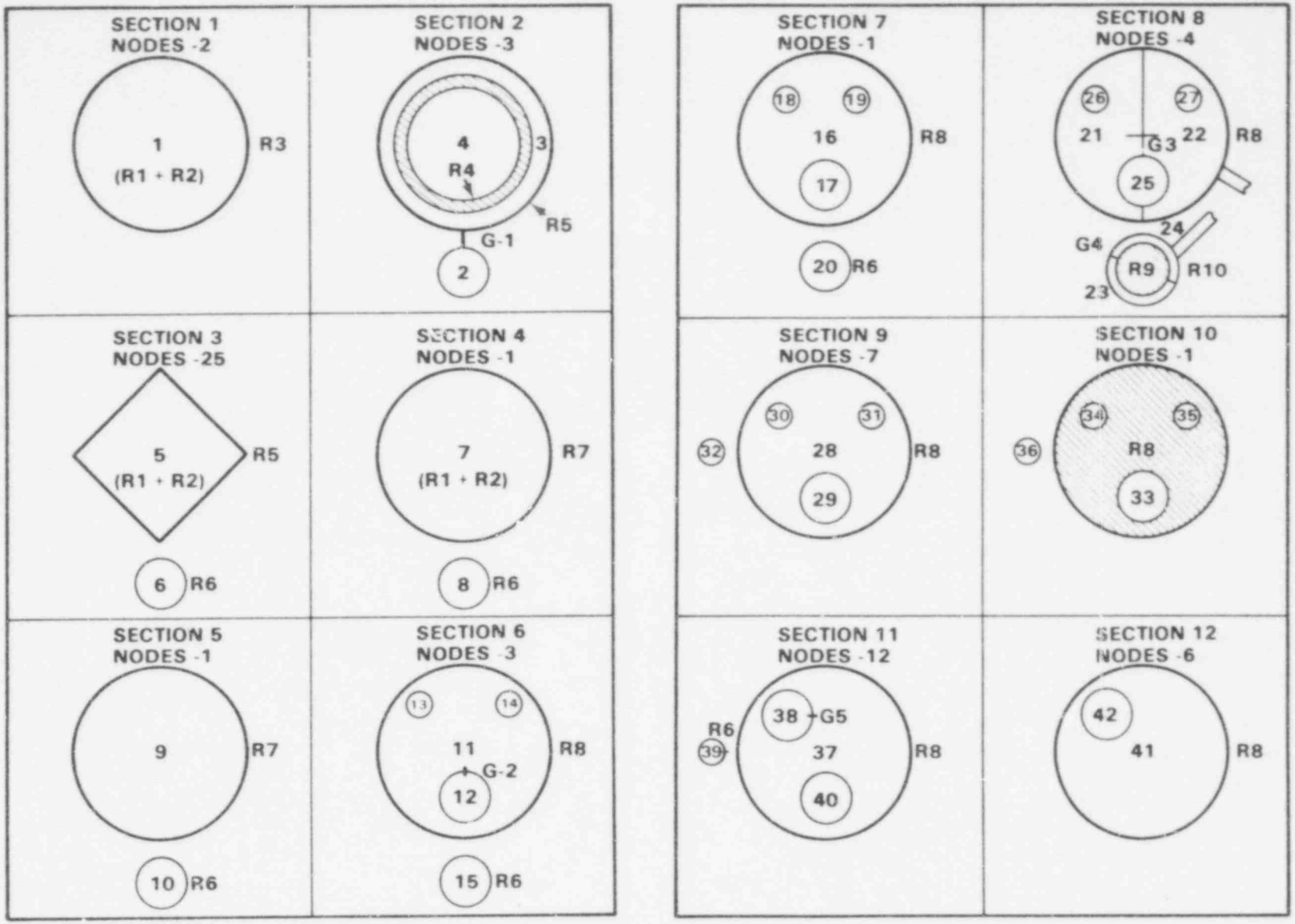

FIGURE 2. Section Nodalization

specified on the broken loop cold leg. Enthalpies were obtained from measured density and pressure for two-phase flow and measured temperature and pressure for single-phase flow. A comparison of the measured and computed upper plenum pressure is shown in Figure 3.

The volumetric flows in the upper plenum and lower downcomer are shown in Figures 4 and 5. Temperature plots of the hot rod towards the bottom, at the midplane and near the top are given in Figures 6, 7 and 8. Densities in the upper downcomer, lower downcomer, lower plenum, bottom of core, top of core, upper plenum and upper head are shown in Figure 9 through 15.

The predicted upper plenum pressure compares quite well with the data except during the period from 5 to 15 seconds and again from 25 to 35 seconds, indicating that the pressure drop from the upper plenum to the broken cold leg was not predicted correctly during these periods.

The predicted volumetric flows compare relatively well with the data, being somewhat higher during the initial stages of blowdown. This is believed to be mainly a result of the gross nodalization of the core, resulting in a higher vapor generation rate at higher pressures. During emergency core cooling injection, oscillatory behavior is computed as well as measured. While the measured oscillations are not exactly reproduced by the computation, it is believed that about the correct amount of condensation is occurring in the downcomer. The hot-rod temperatures agree less well with the data. In general, the temperatures are initially overpredicted and then too much cooling occurs during the period of upper head flashing. The high temperatures, particularly near the bottom of the rod, are thought to be the result of excessive vapor generation early in the blowdown, resulting in early dryout of the rod. Finer nodalization of the core is expected to improve the comparison early in time. The excessive cooling during upper head flashing may be partially explained by the gross core nodalization as average fluid conditions are used for both the hot and colder regions of the core. If additional channels were used in the core, one might expect the liquid to go down around the cooler rods of the core, providing less cooling to the hot rod. The major cause, however, is the result of a coding error in the code's heat flux

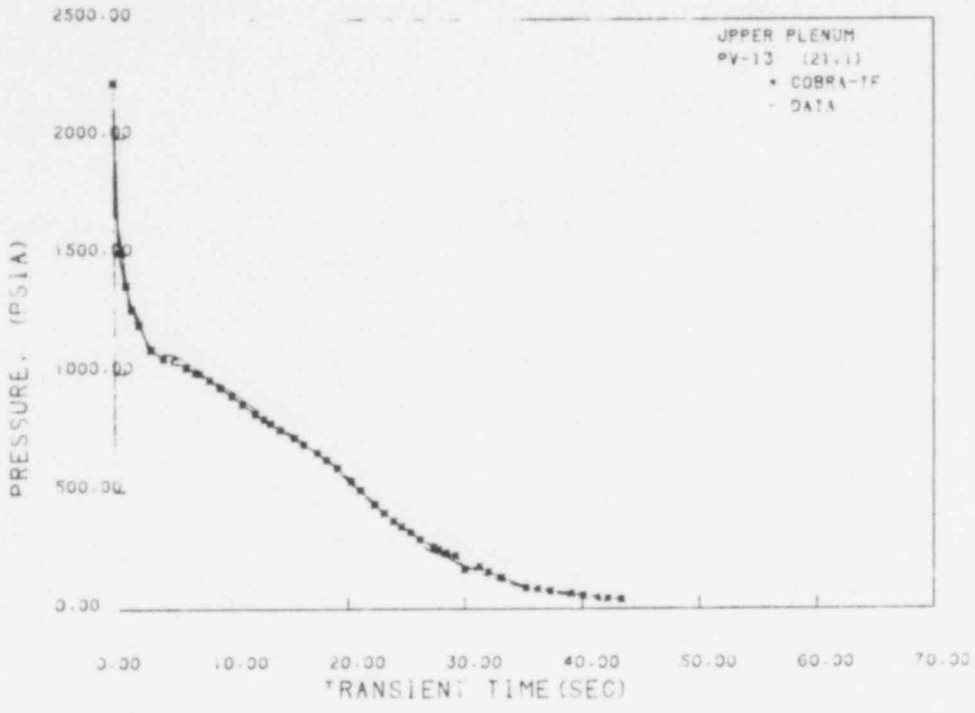

FIGURE 3. Upper Plenum Pressure

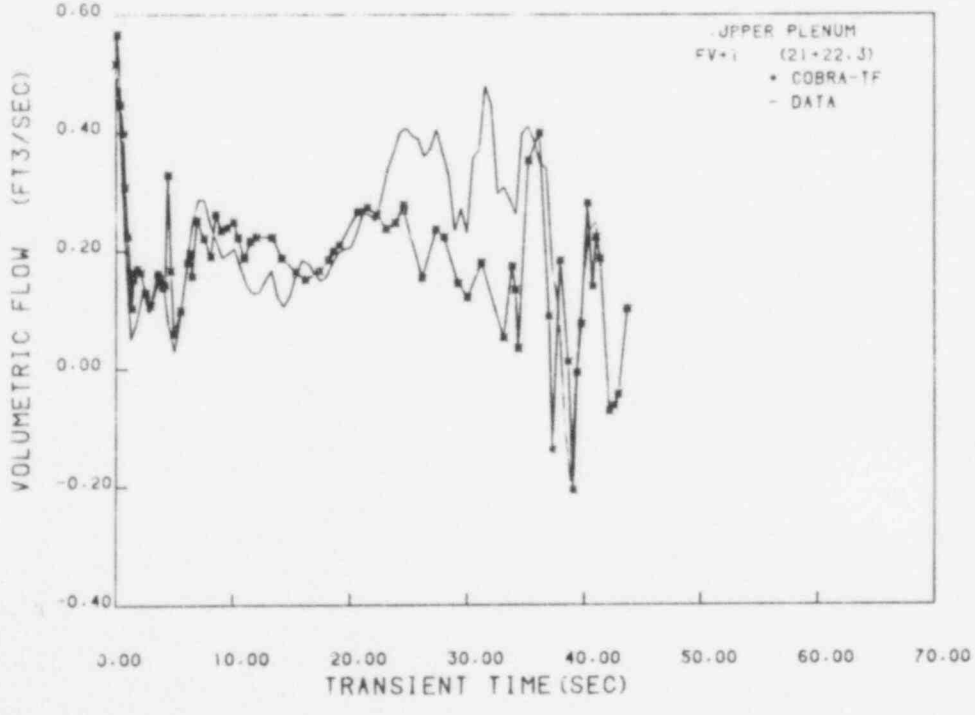

FIGURE 4. Upper Plenum Volumetric Flow

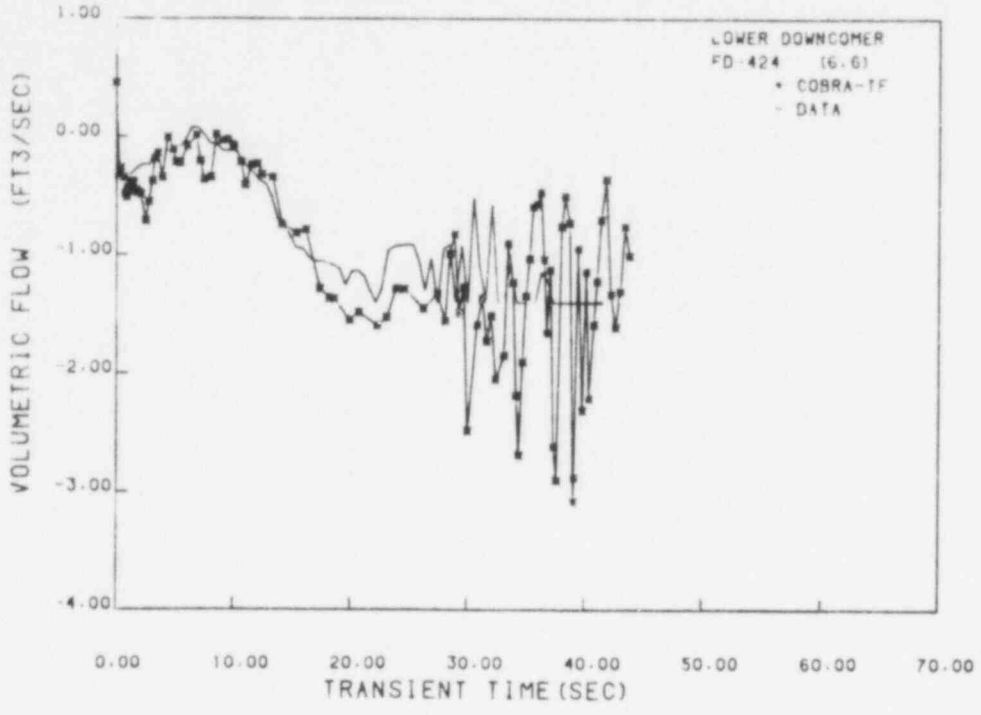

FIGURE 5. Lower Downcomer Volumetric Flow

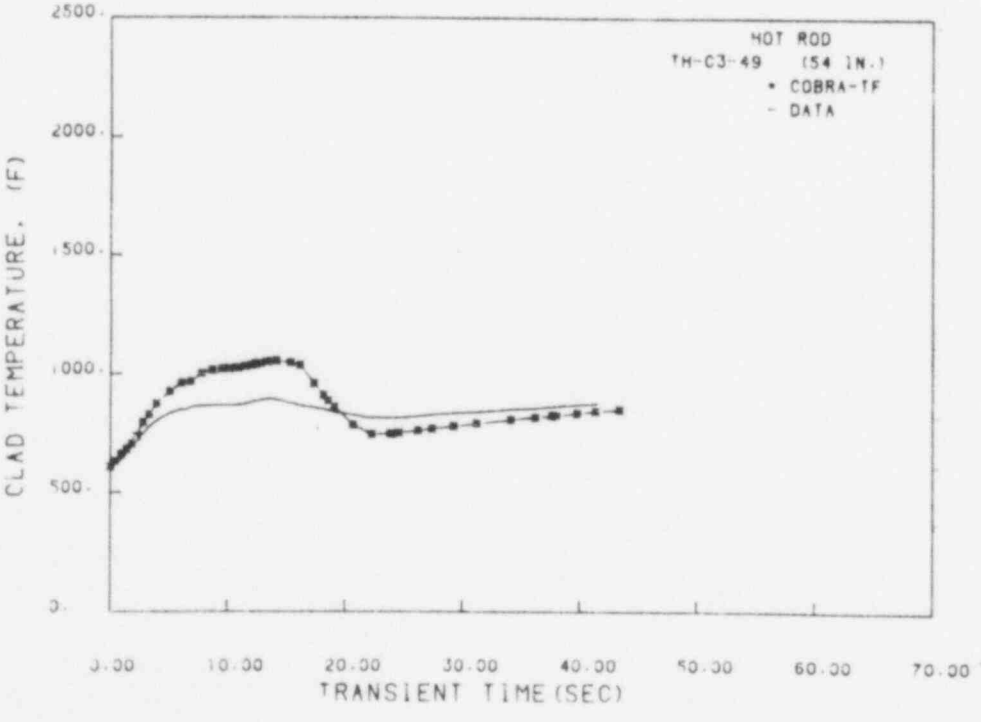

FIGURE 6. Hot Rod Temperature Near Bottom of Rod

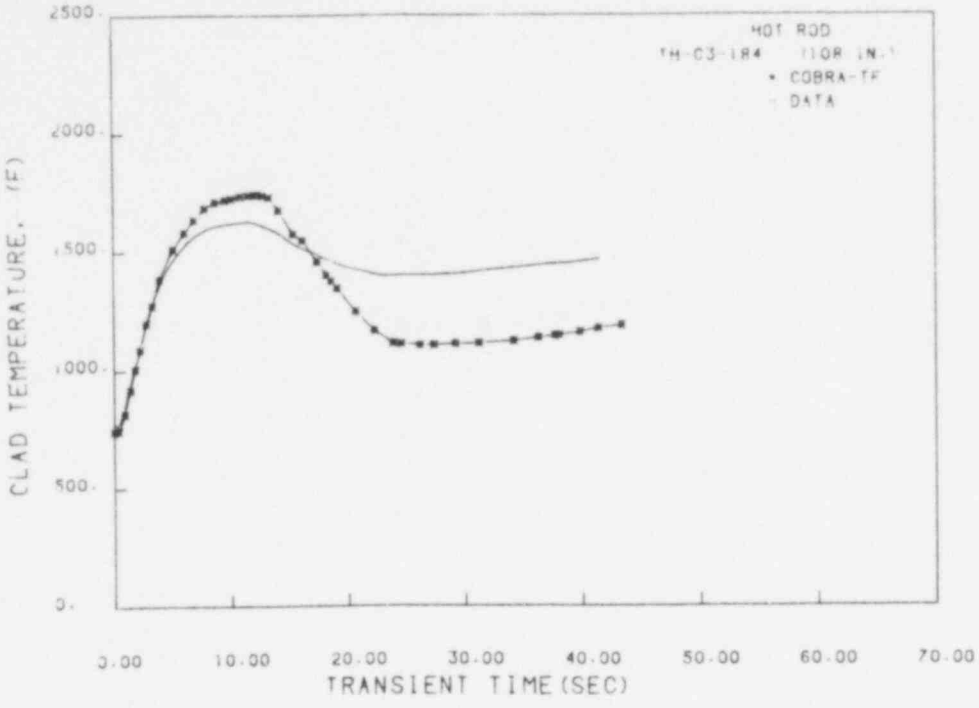

FIGURE 7. Hot Rod Temperature at Midplane

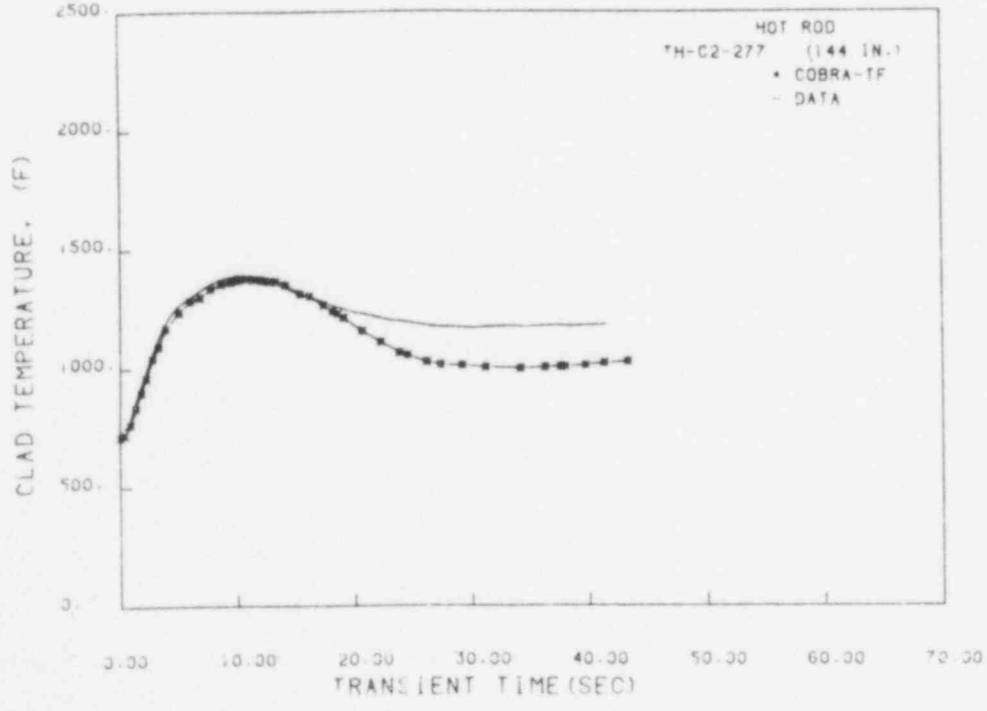

FIGURE 8. Hot Rod Temperature Near Top

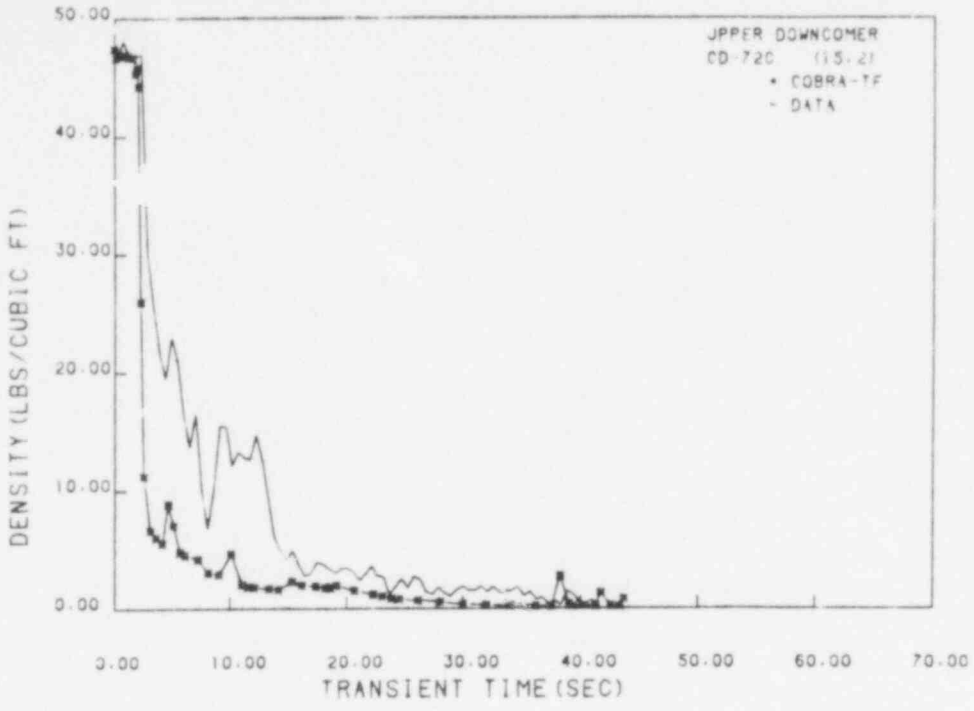

FIGURE 9. Upper Downcomer Density

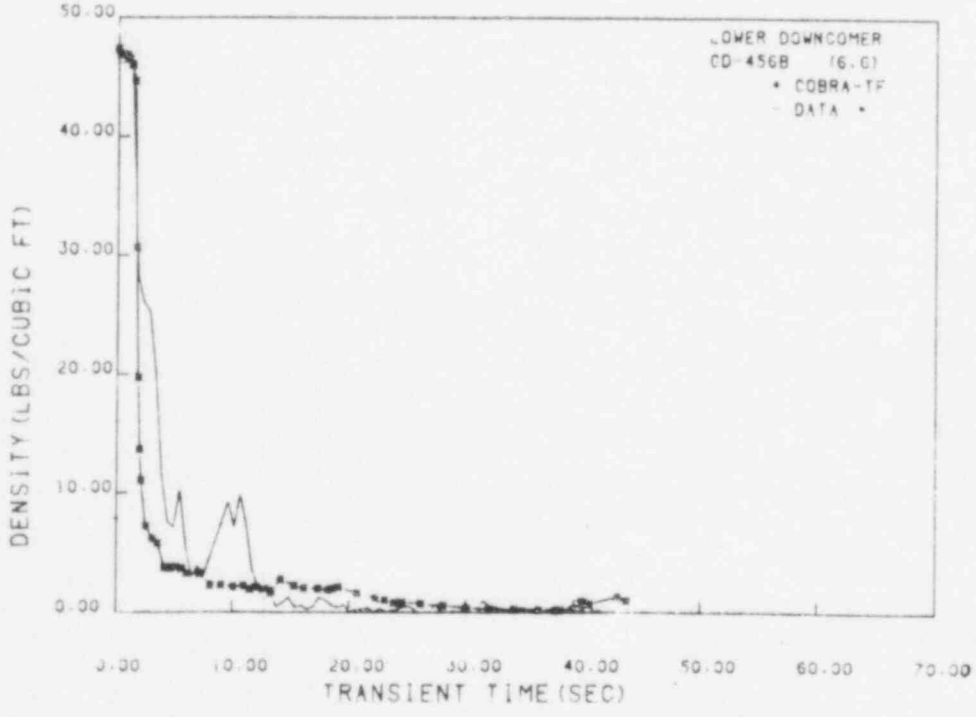

FIGURE 10. Lower Downcomer Density

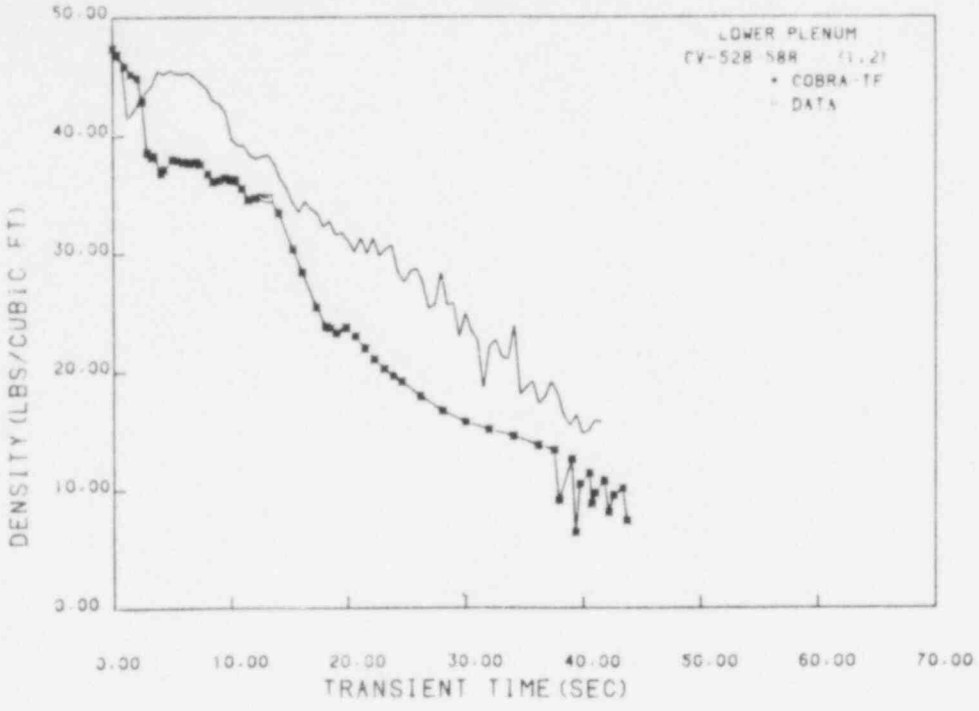

FIGURE 11. Lower Plenum Density

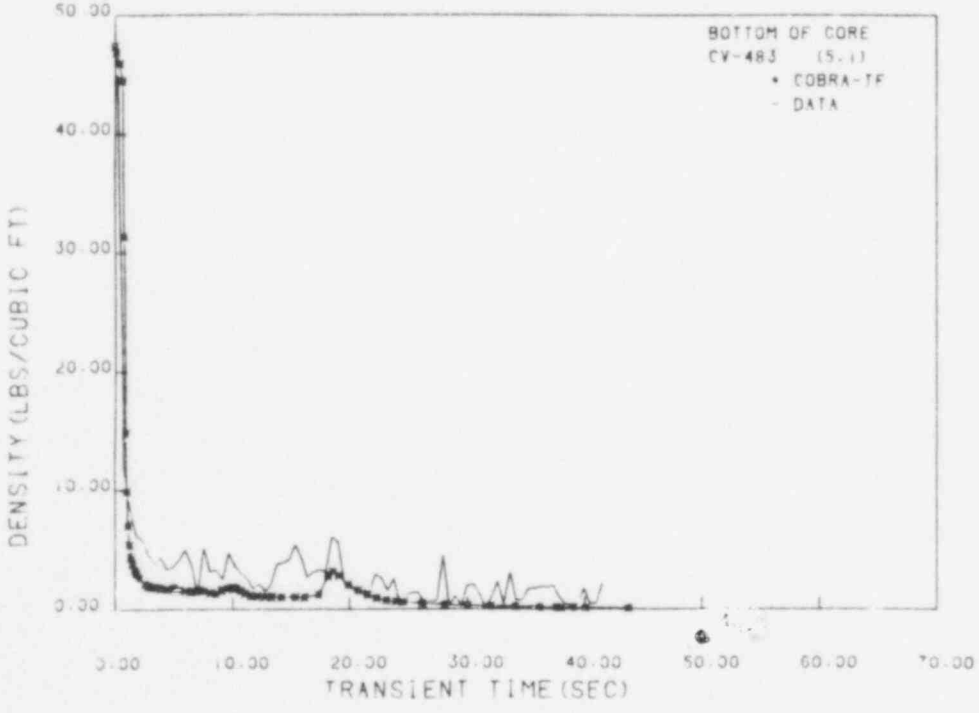

FIGURE 12. Density at Bottom of Core

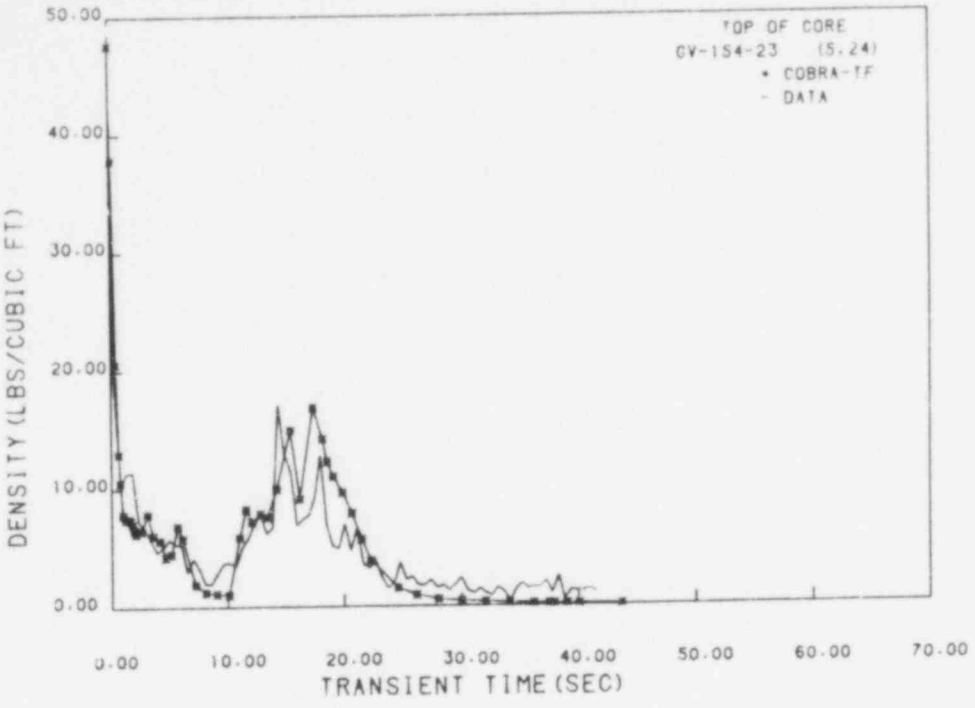

FIGURE 13. Density at Top of Core

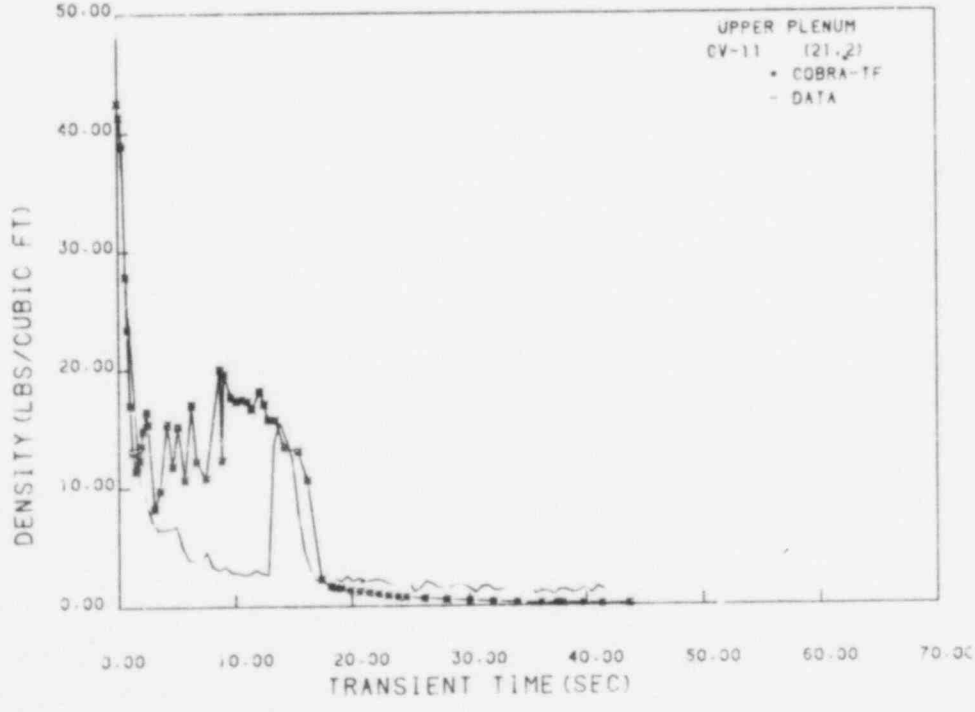

FIGURE 14. Upper Plenum Density

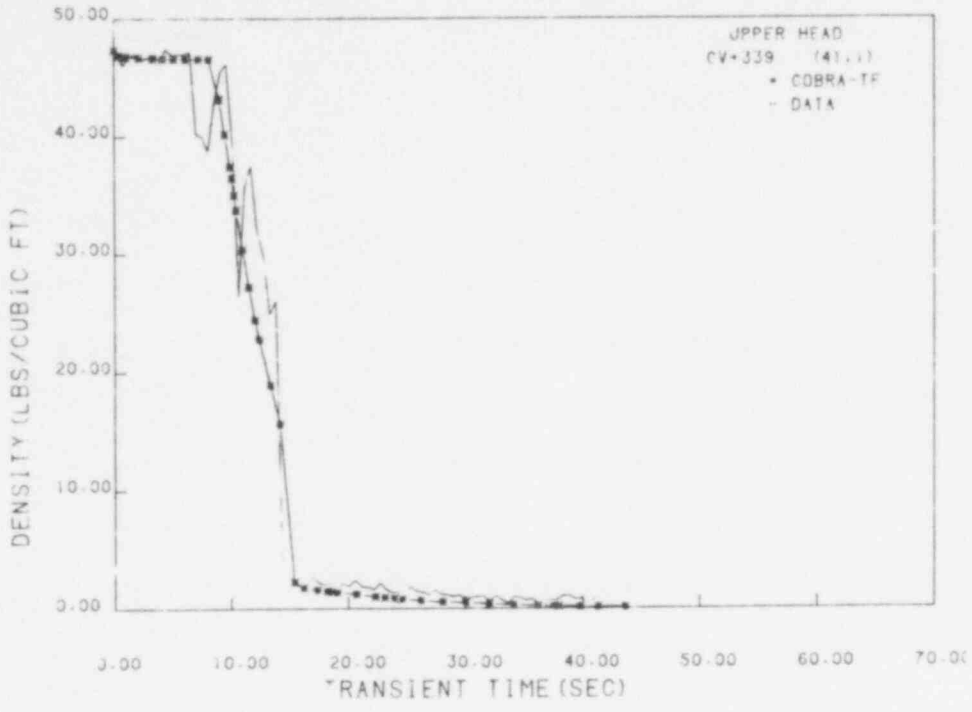

FIGURE 15. Upper Head Density

calculation. The error has been corrected and should give improved results in future simulations.

The computed densities are in good agreement with the data with two exceptions. During the initial stages of blowdown, the density in the downcomer is underpredicted. We believe that a vapor core formed in the downcomer during blowdown results in annular flow at a relatively low void fraction. This would result in more slip and account for the measured densities. This type of flow behavior may be expected in a rapidly accelerating flow and is not accounted for in the present flow regime selection logic in the code. The second exception is the upper plenum density. The predicted density was higher than the measured density during the first 12 seconds. This is a direct result of the one-dimensional nodalization of the upper plenum above the hot legs. The nodalization did not permit the fluid above the hot legs to mix with the hotter fluid coming from the core. This resulted in a steady-state fluid temperature in this region equal to the cold leg temperature. This fluid would not flash until later in time, allowing it to fall down into

the lower part of the upper plenum. The predicted fluid density at the top of the core compares very well with the data, indicating that the amount of liquid being delivered to the core from the upper head is being correctly computed.

In general, the results of the simulation are encouraging, while the data comparisons point out the need for improvements in both the nodalization and the physical model. Some changes and corrections have already been made which should improve future calculations.

THERMAL MODEL DEVELOPMENT

Qualification of the "fine mesh-rezoning" quench front model and incorporation of the rod model into the entrainment version of COBRA-TF occupied this reporting period. Development of the circumferential conduction option (one-third complete) was halted in accordance with the new project priorities formulated at the mid-year review.

Qualification efforts were directed toward two objectives:

- assessment of the numerical accuracy of the "fine mesh-rezoning" technique
- assessment of the integrated thermo-hydraulic model's ability to simulate bottom reflood experiments.

Confirmation of the numerical quench front model's ability to resolve steep axial temperature gradients in an environment of stepwise-discontinuous surface heat transfer coefficients was established through comparison with the predictions of analytical steady-state quench front models. Simulations for both a two-regional model (Yamanouchi 1968) and a three-region model (Kelly 1978) were performed.

In both the analytical and numerical predictions a thin-walled (1 mm thick) stainless steel plate was employed as the conductor geometry. Upon this single stair step heat transfer coefficient profile was imposed for the two-region model. Figure 16 illustrates this profile and shows the discontinuity at the quench front separating the wetted and unwetted regions. The assumed boundary conditions were:

fluid temperature = 212°F
quench temperature = 500°F
wet side heat transfer coefficient = 3000 $(\frac{BTU}{hr/ft^2/°F})$
dry side heat transfer coefficient 0.0

Prediction for the steady-state quench front velocity versus initial wall temperature are compared in Figure 17. In the COBRA-TF simulations, transients were run until the quenching rates approached a constant value. At moderate and high initial wall temperatures, the comparison is quite good; however, at low temperatures, when the wall temperature approaches the quench temperature, COBRA-TF overpredicts the quench velocity. This discrepancy is a form of numerical diffusion and encountered because there is not enough of a temperature difference downstream of the quench front to allow fine mesh-rezoning. Overall, the numerical model did a good job of resolving a severe and unrealistic discontinuity.

A more realistic, though still more severe than would actually be encountered in reactor safety, heat transfer coefficient profile is used in the three region simulation. This profile, illustrated in Figure 18, contains a double stair step delineating three regions: wetted, transition, and dry. The applied boundary conditions are:

fluid temperature = 212°F
CHF temperature = 265°F
quench temperature = 750°F
wet side heat transfer coefficient = 3000 $(\frac{BTU}{hr/ft^2/°F})$
transition heat transfer coefficient = 500
dry heat transfer coefficient = 0.0

Predictions for the steady state quench front velocity are presented in Figure 19. Reasonable agreement between the analytical and numerical solutions exist for the entire temperature range, with COBRA-TF slightly underpredicting the quenching rate. Figure 20, a comparison of the predicted lengths of the transition boiling region, shows that the numerical model predicted a flatter temperature profile than the analytical model, accounting for the underprediction of velocity.

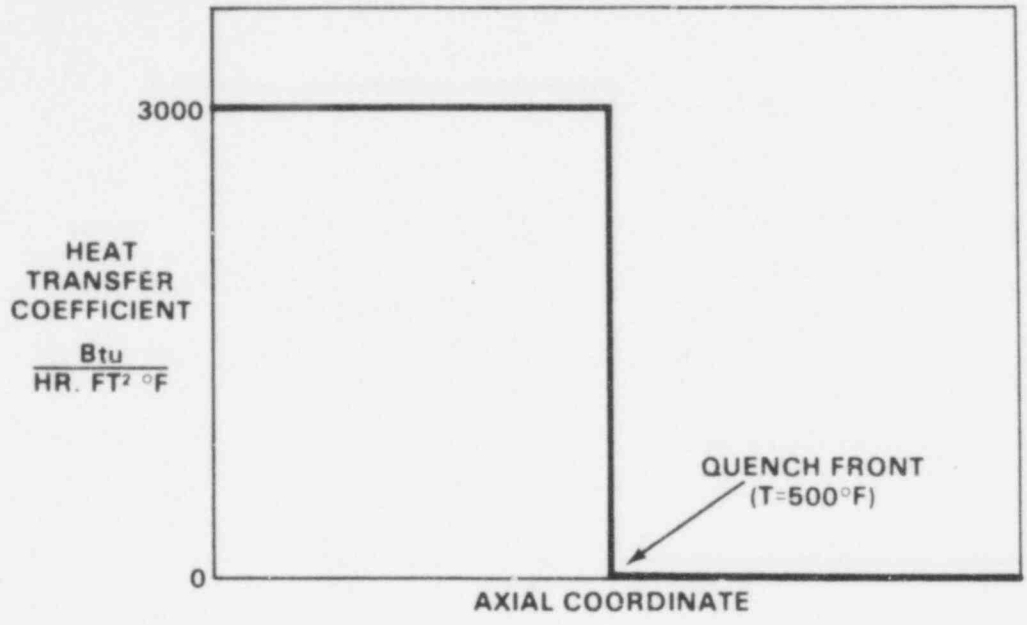

FIGURE 16. Analytical Model: Two Region

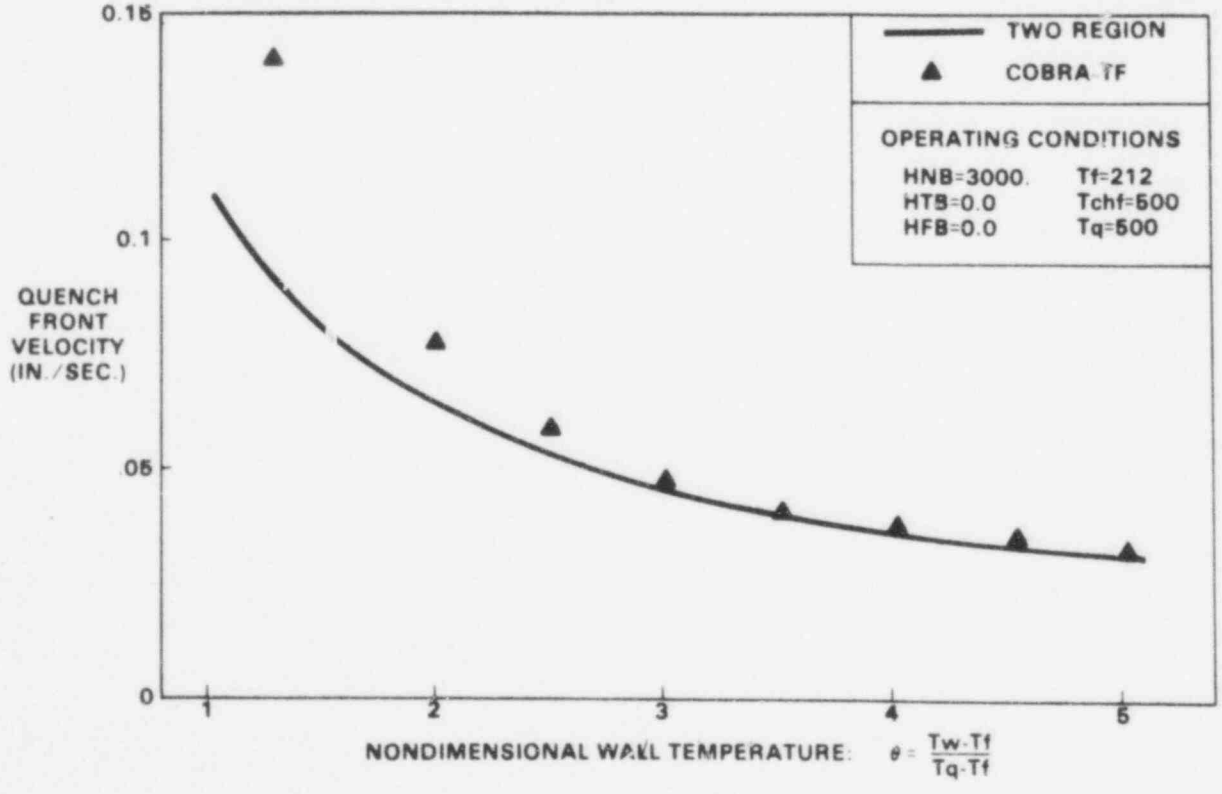

FIGURE 17. Two Region Model: Comparison of Analytical and Numerical Predicted Quench Front Velocity

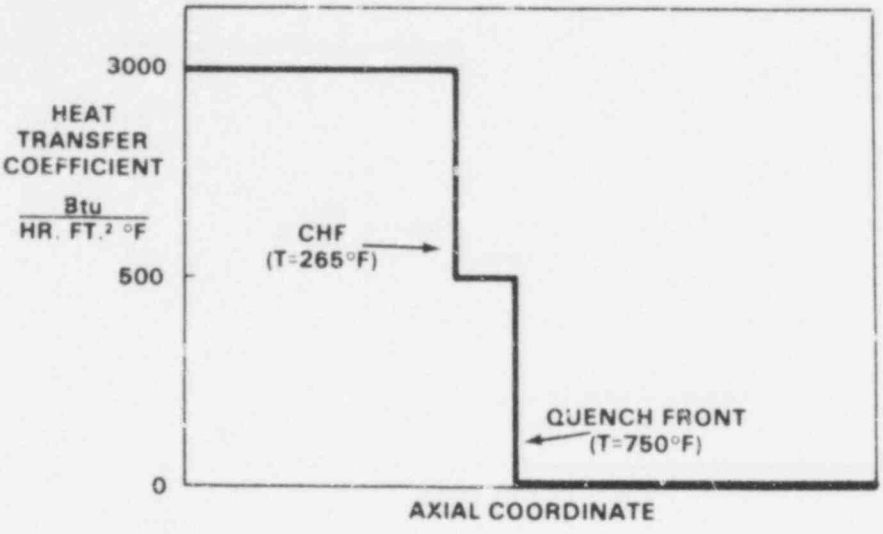

FIGURE 18. Analytical Model: Three Region

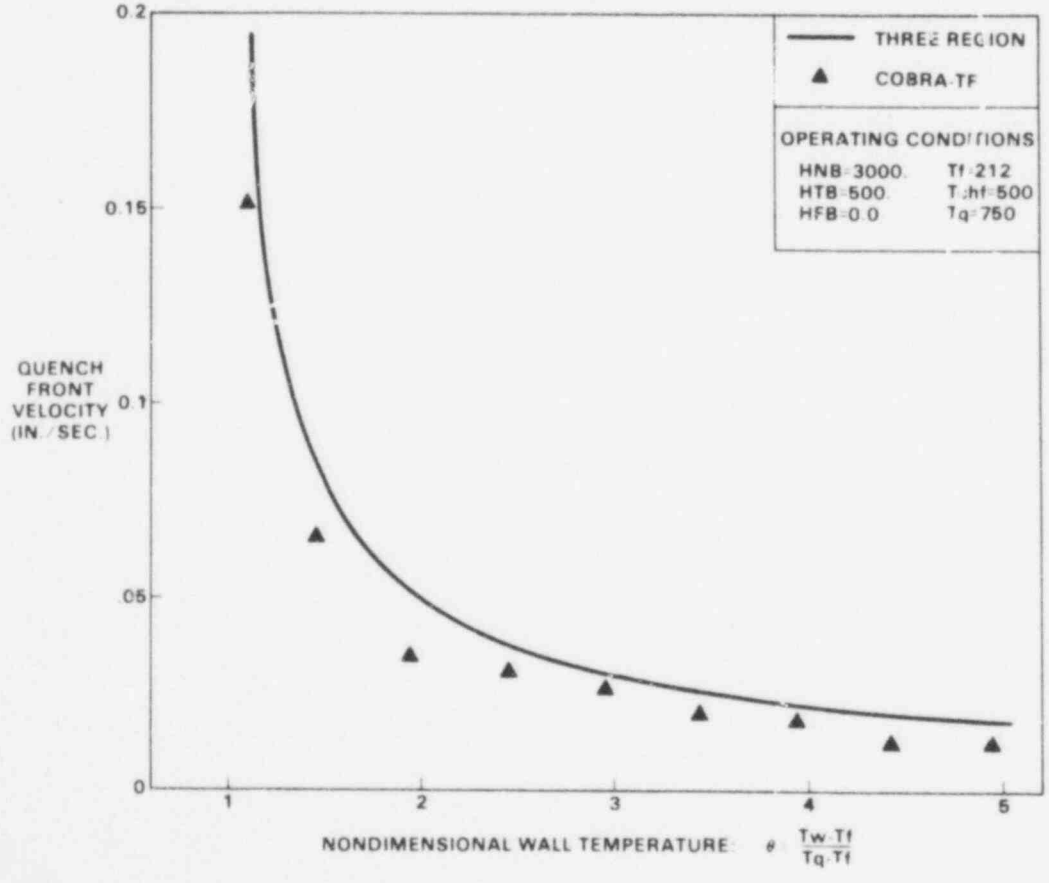

FIGURE 19. Three Region Model: Comparison of Analytical and Numerical Predicted Quench Front Velocity

791153

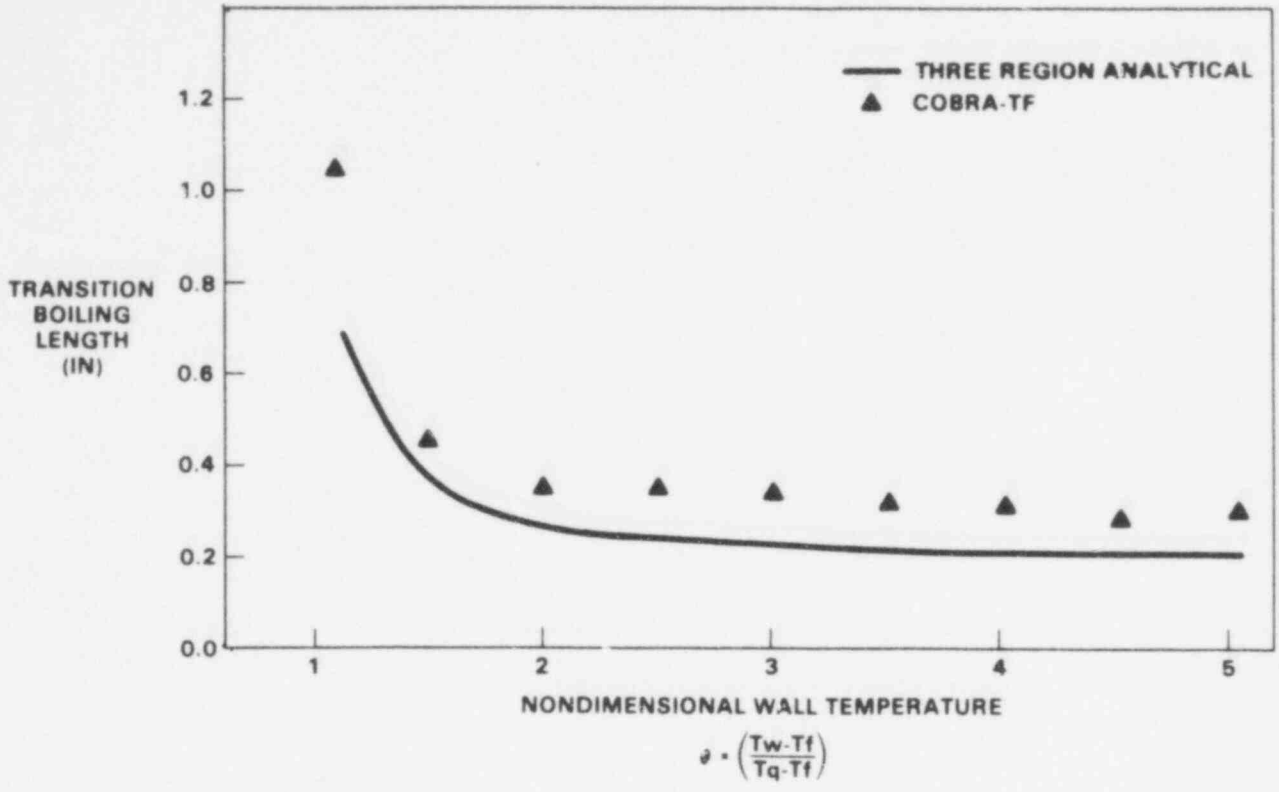

FIGURE 20. Comparison of Predicted Analytical and Numerical Transition Boiling Region Lengths

In summary, the "fine mesh-rezoning" model was able to predict quench front propagation for cases where axial conduction was all important and resolve temperature profiles across discontinuities in the surface heat transfer coefficient. It is expected that, for modeling quenching of fuel rods where discontinuities are smoothed by the effects of two-dimensional conduction and precooling, the resolution capabilities of the "fine mesh-rezoning" model are more than adequate.

A series of four FLECHT forced reflood tests were also simulated to exercise the code and assess the performance of the combined quench front, heat transfer and hydrodynamic models. Table 1 lists the operating conditions for these tests. Tests 3541, 3440 and 3642 are at the same nominal conditions with a parametric variation of initial clad temperature. Likewise, tests 3541 and 4321 are similar except for flooding rate.

TABLE 1. FLECHT Forced Reflood Test.

Run	T_{Clad}, °F	Power, kW/ft	Flooding Rate, in./sec	T_{Fluid}, °F	Pressure, psia
3541	1598	1.24	5.9	148	57
3440	1204	1.24	5.9	155	55
3642	1805	1.24	5.9	148	57
4321	1608	1.24	3.9	151	58

Figures 21 through 24 display the mid-plane clad temperature history of these four tests. The data comparisons range from fair to very good and provide confidence that most of the important phenomena are being modeled adequately. All four curves indicate an early predicted turnaround time. This appears to be the result of an excessive amount of vapor generation in the lower core region at the beginning of the transient. Possible causes for this are:

- an inaccuracy in initializing the clad temperature in the first 2 ft of the heater rods (which didn't contain thermocouples)
- not enough condensation
- using only one channel, rather than a hot and cold channel, for the hydrodynamic model.

In tests 3541 and 3642 there is a period during which the heat transfer is underpredicted. At this time the rod should be in inverted annular film boiling (IAFB). However, because too much liquid was entrained and carried over, the local void fraction was too high and an interpolation between IAFB and dispersed flow film boiling was used. Tests 3440 and 4321 both quench early despite having followed the temperature history up to that time. This appears to result from the inclusion of Hsu's transition boiling region heat transfer coefficient as an additive term in the IAFB region.

Despite these discrepancies, the overall predictive capability of the code anpears credible and should improve with further experience and modeling improvements.

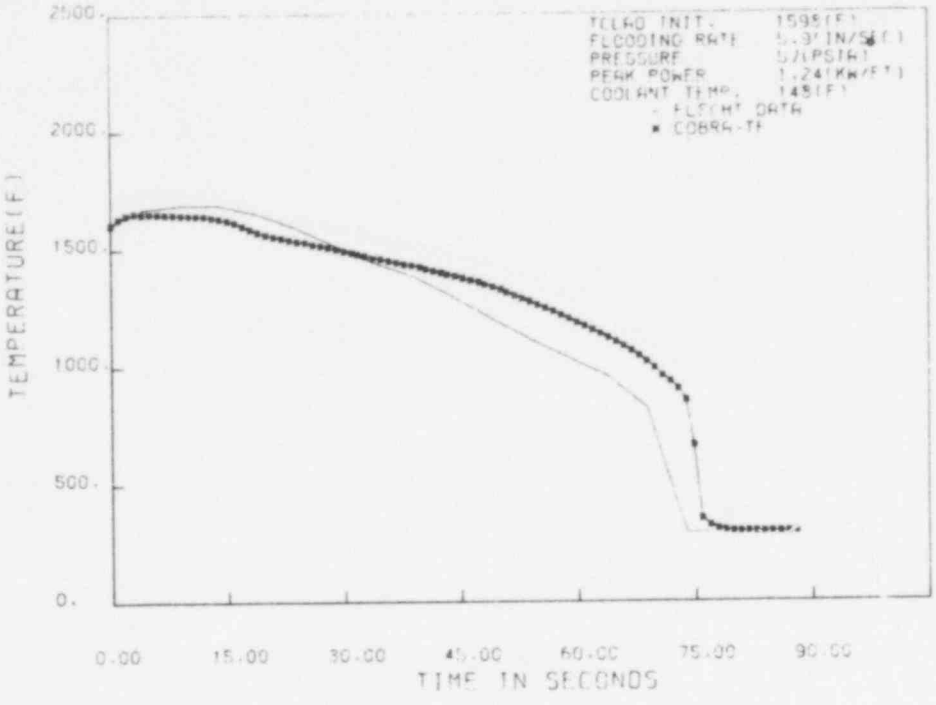

FIGURE 21. FLECHT 3541 - Clad Temperature versus Time

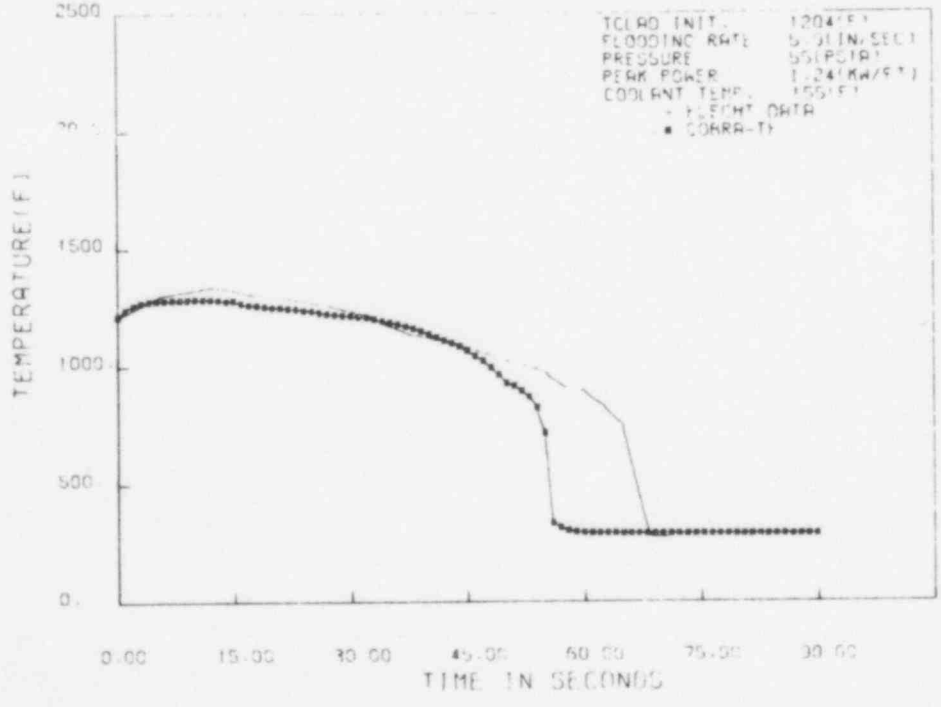

FIGURE 22. FLECHT 3440 - Clad Temperature versus Time

791156

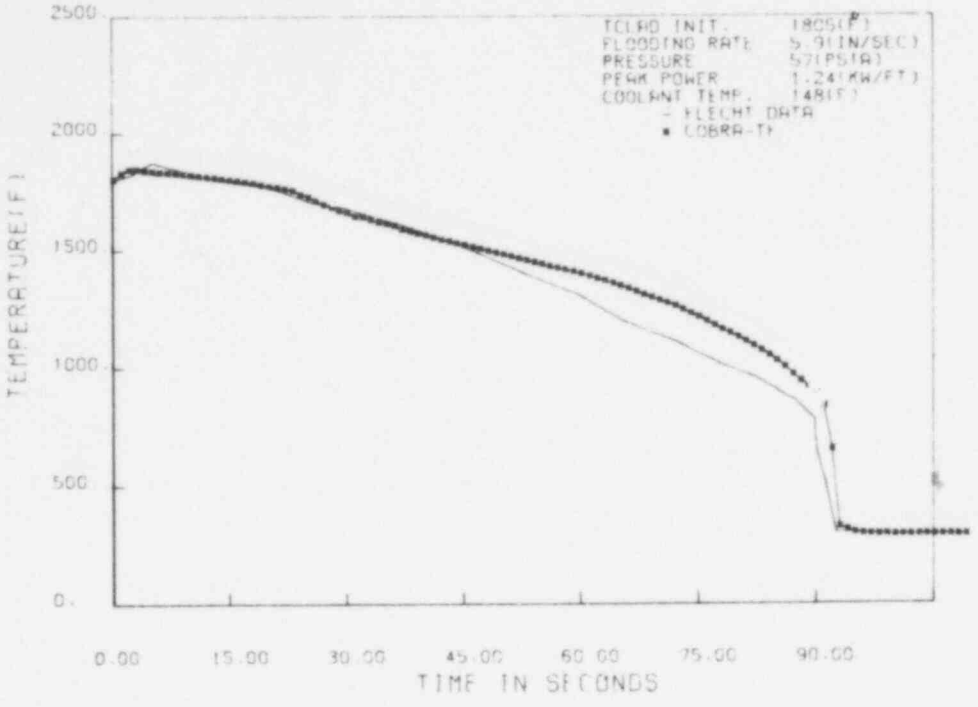

FIGURE 23. FLECHT 3642 - Clad Temperature versus Time

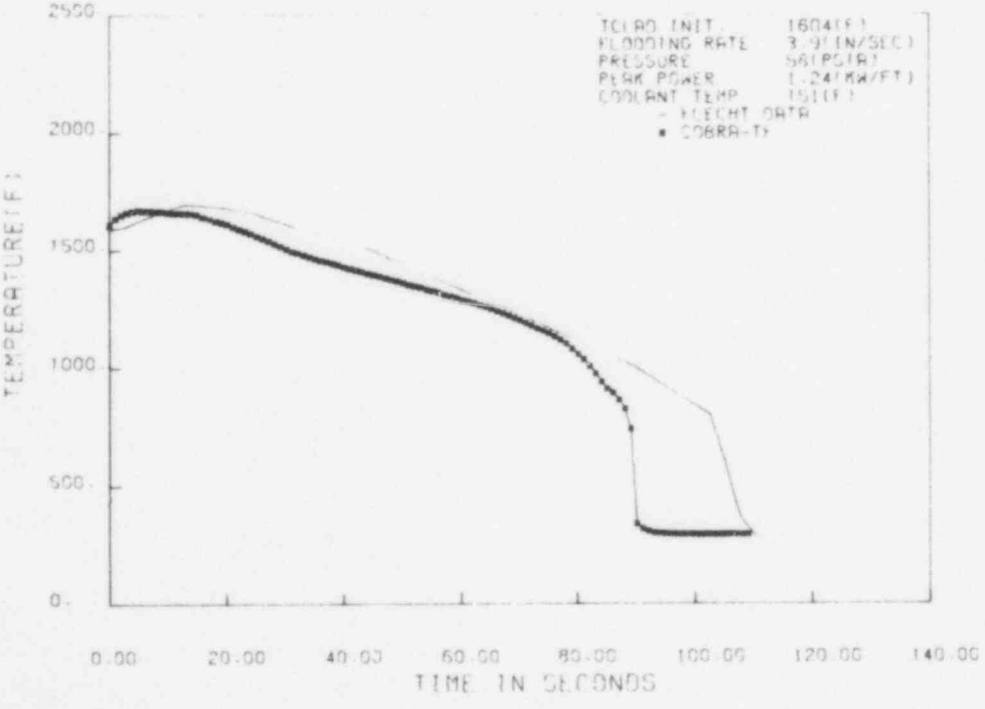

FIGURE 24. FLECHT 4321 - Clad Temperature versus Time

Figures 25 and 26 illustrate the dependence of quench front velocity on clad temperature and the quench "envelope." Figures 12 and 13, axial temperature and heat flux profiles, are especially interesting since they depict the degree of fine mesh noding (each asterisk = 1 node) and the consequent degree of resolution of the boiling curve in the region of the quench front.

COBRA-TRAC COUPLING

This quarter a high priority project of incorporating the COBRA-TF vessel model into the system code, TRAC, was begun. The purpose of this work is to provide a UHI system simulation capability.

The computer programming is nearly complete and the new code is expected to be operational early in the next quarter. The coupling was accomplished by removing all of the TRAC vessel subroutines and replacing them with the corresponding COBRA-TF subroutines. The COBRA-TF rod model is also being used in place of the TRAC core heat transfer model. The new model will utilize the advantages of channel splitting to model the complex geometry of UHI experimental facilities and plants.

FUTURE WORK

After completion of the COBRA-TRAC coupling, a system simulation of the Semiscale MOD3 test S07-6 will be performed. This next quarter, work will commence on the hot bundle capability. This work was halted until work on the COBRA-TRAC coupling was completed. Additional reflood simulations will also be performed during the next quarter.

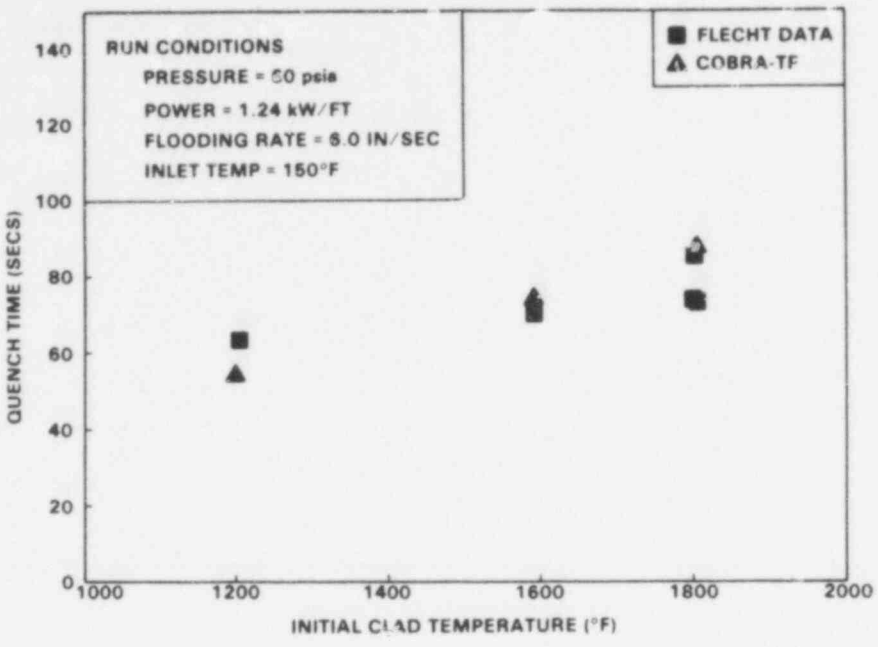

FIGURE 25. Effect of Initial Clad Temperature on Quench Time at Hot Rod Mid-Plane

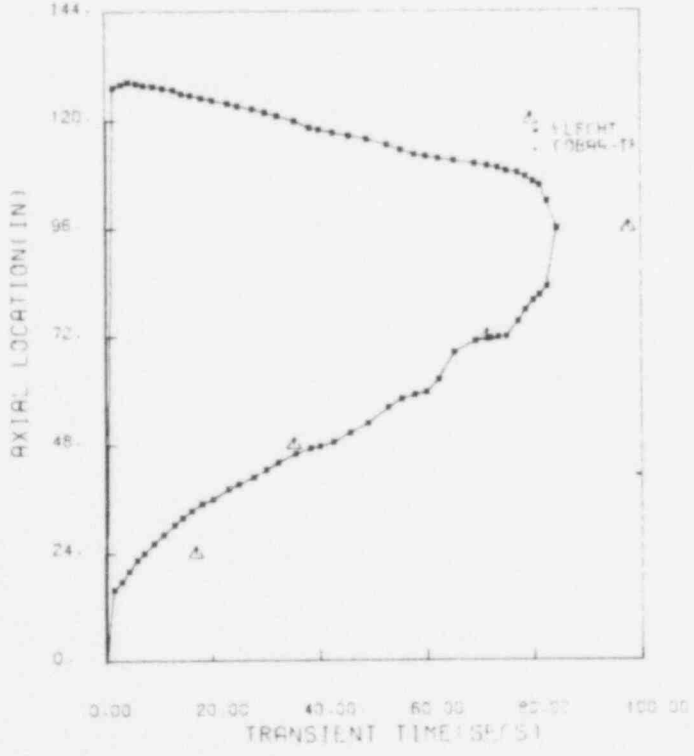

FIGURE 26. Quench Front Propagation - Run 3541

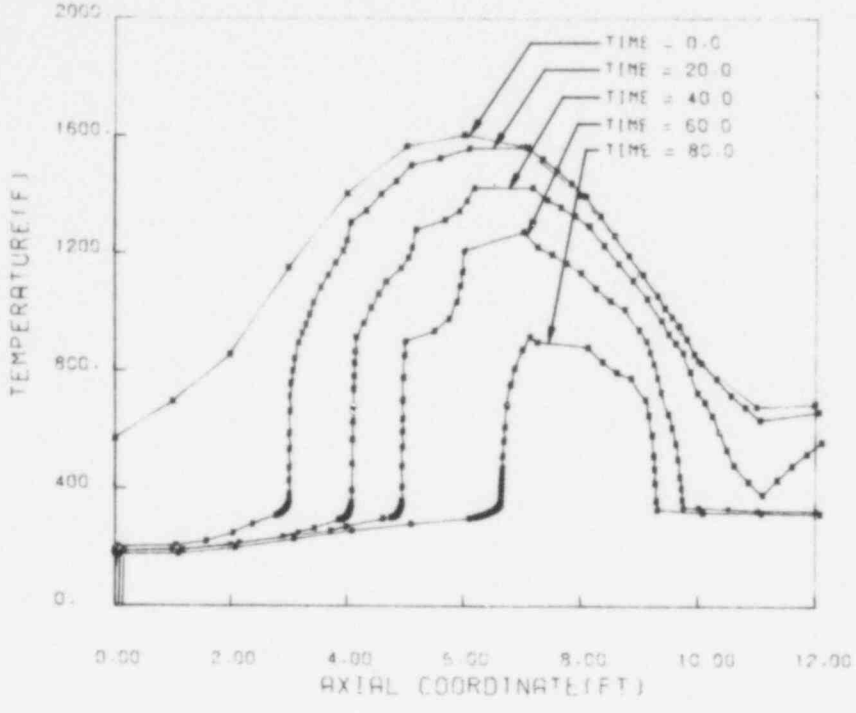

FIGURE 27. FLECHT 3541 - Axial Temperature Profile

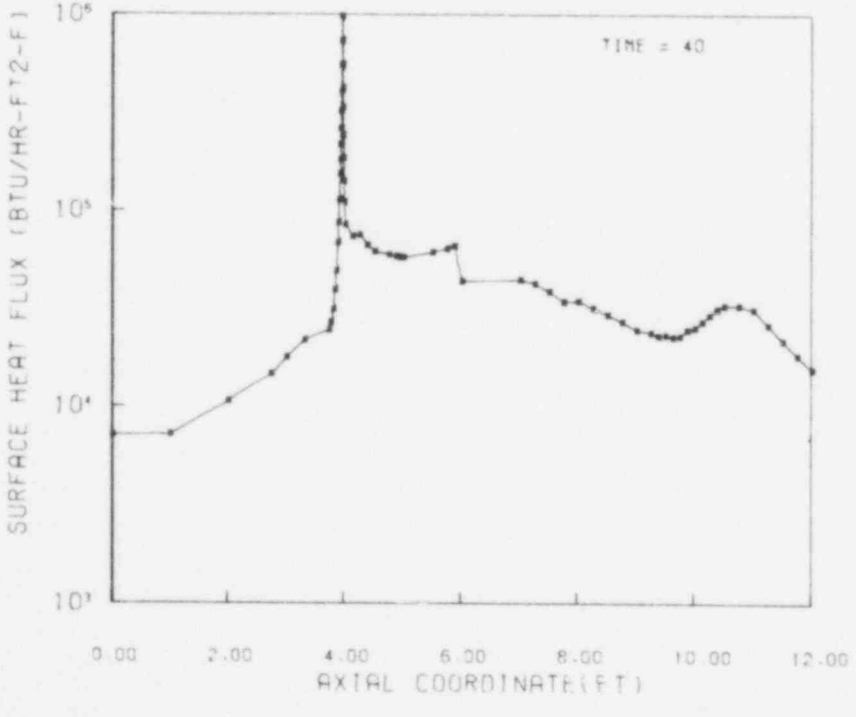

FIGURE 28. FLECHT 3541 - Axial Surface Heat Flux Profile

REFERENCES

Kelly, J. M. 1978. "Core Thermal Model Development." In Reactor Safety Research Programs Quarterly Report, April 1 - June 30, 1978, J. L. Hooper, ed., NUREG/CR-0341, PNL-2653-2, Pacific Northwest Laboratory, Richland, Washington.

Yamanouchi, A. 1968. "Effects of Core Spray Cooling in Transient State After Loss of Coolant Accident." Journal of Nuclear Science and Technology 5(11):547-558.

INTEGRATION OF NONDESTRUCTIVE EXAMINATION RELIABILITY AND FRACTURE MECHANICS*

G. L. Posakony, Program Manager
F. L. Becker, Project Manager
S. H. Bush, Project Manager

SUMMARY

Primary emphasis during the last quarter was placed on the fabrication of cracked samples for the Phase 1 study. Fabrication of the crack characterization samples is in progress. The thermal fatigue process has been selected for cracking welded pipe samples. Equipment for the thermal fatigue process is on order and procedures are being developed to control the crack depth and aspect ratios.

The state-of-practice review is approximately 50% complete and will be finalized in June.

INTRODUCTION

Activities during the past quarter have been primarily directed toward fabrication of the crack characterization samples. These activities are described below for each task.

*RSR Fin. Budget NO: B2289-9; RSR Contact: J. Muscara

TASK ACTIVITIES

TASK 1: DRAFT WHITE PAPER

The initial draft of the first six chapters has been completed and is being reviewed. Comments have been received and are being considered. Although we had planned to provide a summary of the first six chapters in this report, this has not been possible due to lack of personnel. We do plan to provide this summary in the near future.

TASK 2: STATE OF PRACTICE REVIEW

PNL has contacted four public utilities, four private inspection agencies, four LWR vendors and one national laboratory concerning PNL/NRC interest in having various organizations participate in the state-of-practice survey. Each organization contacted showed interest in the program and was willing to participate in the survey.

Interviews started in late March and it is expected that by mid-May all interviewing will be completed. Therefore, a June 1, 1979 milestone has been set for completion of a draft of the survey report.

A one-day review meeting in early June is being considered in which all the organizations surveyed would be presented with the study results. Draft copies of the report would be sent to each organization prior to the meeting for their review. Such a meeting would provide a timely, convenient means for each organization to review the report and make comments on report content, structure, and method of reporting data. Because many of the participants are unacquainted with other inspection agencies, ultrasonic procedures, equipment used, and testing techniques, this meeting would provide a common ground for each participant to meet and openly discuss the results of the survey. In addition, weak sections of the report could be supplemented with additional information derived from this meeting. The availabaility of the participants will be a major factor in determining if such a meeting can be held.

The state-of-practice report is scheduled for publication in late June.

TASK 3: ANALYSIS-BEFORE-TEST DOCUMENT

The Phase 1 program plan and analysis-before-test document have been completed and submitted for review and approval. Phase 2 analysis-before-test document will be completed by November 1, 1979. A preliminary program plan for the remainder of the program will be submitted by July 1.

TASK 4: FRACTURE MECHANICS ANALYSIS

Fracture mechanics studies during the past quarter have investigated the thermal fatigue process, which will be used to produce cracks in piping samples (Task 6). The purpose of this study was to provide guidance in establishing fatigue parameters and to describe the influence of thicknesses and material properties on the process.

The primary conclusions of this study have been the following:

1. Cycle times (cooling) greater than 5 seconds should not be required.
2. Part thickness has little influence on the process.
3. Crack growth rate should be slightly faster in stainless steel than carbon steel.
4. Maximum stress intensity factors are directly related to preheat temperature, and hence crack growth rate.

A complete description of this analysis is contained in Appendix A.

TASK 5: STATISTICAL PROGRAM DESIGN

During a program review held in Silver Springs, Maryland, on April 11, concern was voiced as to the suitability of the statistical approach and the ability of the program to supply data usable for risk analysis. Further discussions will be required to resolve these differences of approach and objectives.

The statistical program approach which will be followed until the program is redirected is as follows:

Phase 1

1. Establish influence of inspection variables.
2. Establish interactive effects of variables in welded pipe samples.
3. Provide base line probability of detection (POD) based on available data base at that time (September 1979).

Phase 2

1. Select sample matrix (the most conservative level of each variable).
2. To establish suitable confidence levels, the number of samples and measurements will be determined on the basis of accepted statistical methodology requirements.
3. Measurements to be performed by industrial ISI vendors.
4. Output basic POD curves (one level of variables).
5. Analyze and report sources of inspection uncertainty for guidance in technique improvement.

Phase 3

1. Develop and test proposed probability of detection models using results of Phase 1 and 2 and supplemental testing.
2. Expand basic POD curves to include new variables based on the results of the model.
3. Based on results of these models, (1) above, construct simplified test matrices for testing other materials.

The probability of detection models referred to above is based on the hypothesis that the larger the signal amplitude returned from a flaw the higher its resultant POD will be. This hypothesis would ordinarily be accepted without question. However, in the testing of reactor piping systems, an inspector encounters many geometrical reflectors for each real flaw that is

found. The question is then how well can he differentiate between real flaws and other reflectors. This question must be answered before these models can be accepted. The principal benefit which can be realized through these models is that a POD curve can be established with substantially fewer samples and measurements.

We believe that in the testing and verifications to be carried out in each phase of the program the sources of inspection errors should be identified and measured, for two reasons. First, the magnitude and source of inspection errors can be used in models, which will substantially reduce the time and cost of POD determination. Second, these measures of inspection unreliability will provide guidance for research and development efforts to improve inspection reliability.

One method of analyzing the source of inspection errors is the event-tree approach. A discussion of this approach is included in Appendix B of this report. This method basically breaks down the events which must occur to properly detect a crack or flaw as follows:

1. The inspection system is capable of detecting the required cracks. System here refers to the instrument, search unit, procedure, test standard and calibration accuracy.
2. The scanning beam must strike the crack and be returned to the search unit.
3. The reflected beam must have an amplitude above the reportable level.
4. The inspection team must categorize the reportable indication as a crack.

The probabilities for each event are then calculated. This method of analysis does not require any additional samples. However, additional information must be recorded. The necessary recording is technically feasible. Further study must be performed to determine the practicality of the procedure.

TASK 6: SAMPLE FABRICATION

Two sample fabrication programs are currently in progress. These include the flaw characteristics samples (fatigue flaws produced by bending) and the thermal fatigue flaws which will be produced in welded samples. The thermal fatigue method of producing flaws in welded pipe samples has been selected based on the following criteria:

1. Feasibility has been established by General Electric San Jose and PNL on a range of materials (stainless and carbon steel) and thicknesses.
2. Flaws produced are both tighter and slightly rougher than those produced by bending fatigue. These are conservative conditions (i.e., more difficult to detect).
3. Small aspect ratios (in the range of 3 to 5) can be produced.
4. The technique is adaptable to large components such as PWR main coolant pipes.
5. Multiple flaws can be produced simultaneously.
6. The method is less costly than using large fatigue machines.

A description of the progress for each of the sample production programs is given below.

Thermal Fatigue

A pilot program to determine the feasibility of using thermal fatigue for producing cracks in (10-in., Schedule 80, Type 304) stainless steel pipe has been completed. A stand-in specimen of 1/2-inch thick 304 stainless steel plate was used in a prototype thermal fatigue system instead of the actual pipe. The thermal parameter study, reported under Task 4, was used in establishing test parameters.

Thermal fatigue was achieved by heating and quenching of the plate in a localized area at a starter notch. A block diagram of the prototype thermal fatigue system used in this portion of the study is shown in Figure 1. A propane infrared heater, located above the plate, was used to maintain the

temperature of the top surface of the specimen at $1000^{o} \pm 25^{o}F$. Temperature control was achieved by regulating the propane flow to the heater using a high/low control regime. The bypass valve allowed the propane to flow continuously at a metered rate, while the main solenoid valve was operated by the temperature controller to provide high heat output. The thermocouple used to monitor the top surface temperature was set in a thermocouple well to avoid fallacious readings due to the infrared radiation from the heater. The thermocouple well was drilled from the bottom surface of the specimen to within 0.040 in. of the t surface at a distance of 1.0 in. from the center of the starter notch. The dimensions of the plate specimen are shown in Figure 2 along with the location of the thermocouple well. The bottom surface of the plate specimen was quenched in a localized area by confining the water jet within a 1.25 in. I.D. pipe which fit up against the bottom of the specimen, as illustrated in Figure 1. Distilled water was fed to the water jet on a 10-sec on, 30-sec off cycle at 25 psi pressure. Distilled water was used to avoid the formation of an insulating layer at the quenched surface due to precipitation of dissolved impurities. During the quench, the localized reduction of temperature in the quenched area caused the material to attempt to contract with respect to the balance of the plate, which restrained the contraction, producing high tensile stresses at the starter notch (Figure 2). Another thermocouple well was drilled 0.2 in. into the top surface of the plate directly over the quenched region to monitor the thermal cycle. This thermocouple and the top surface thermocouple were recorded on a strip chart for diagnostic and parameter development purposes, as well as to provide a permanent record of the test. Under normal operating conditions temperature variations of $85^{o}F$ were recorded over the quenched region. The temperature variations at the bottom of the plate, however, were much larger. The plate specimen was cycled for a total of 15,000 thermal cycles. The resultant crack is shown in Figure 3. The starter notch and the monitoring thermocouple well can be observed on the surface of the crack.

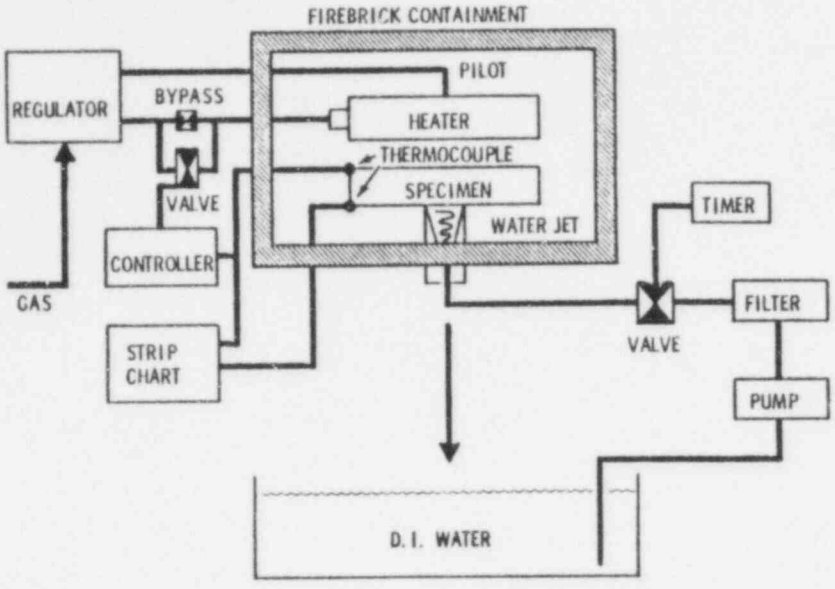

FIGURE 1. Thermal Fatigue Facility Block Diagram

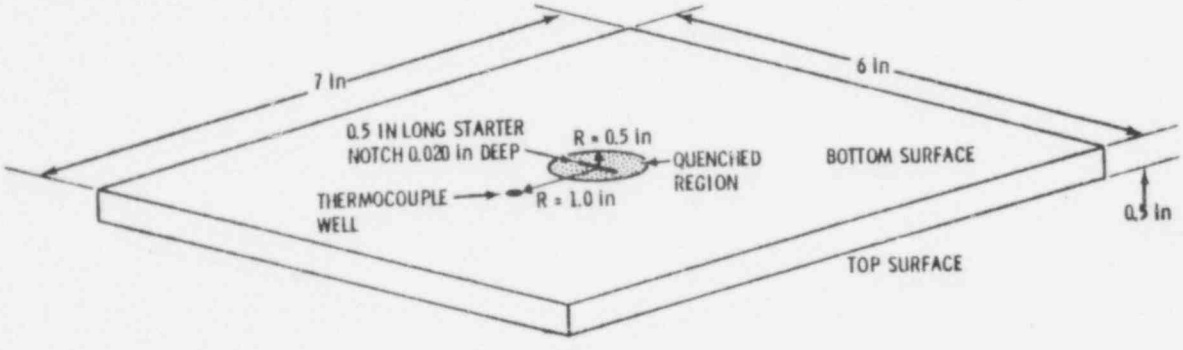

FIGURE 2. Prototype Test Specimen

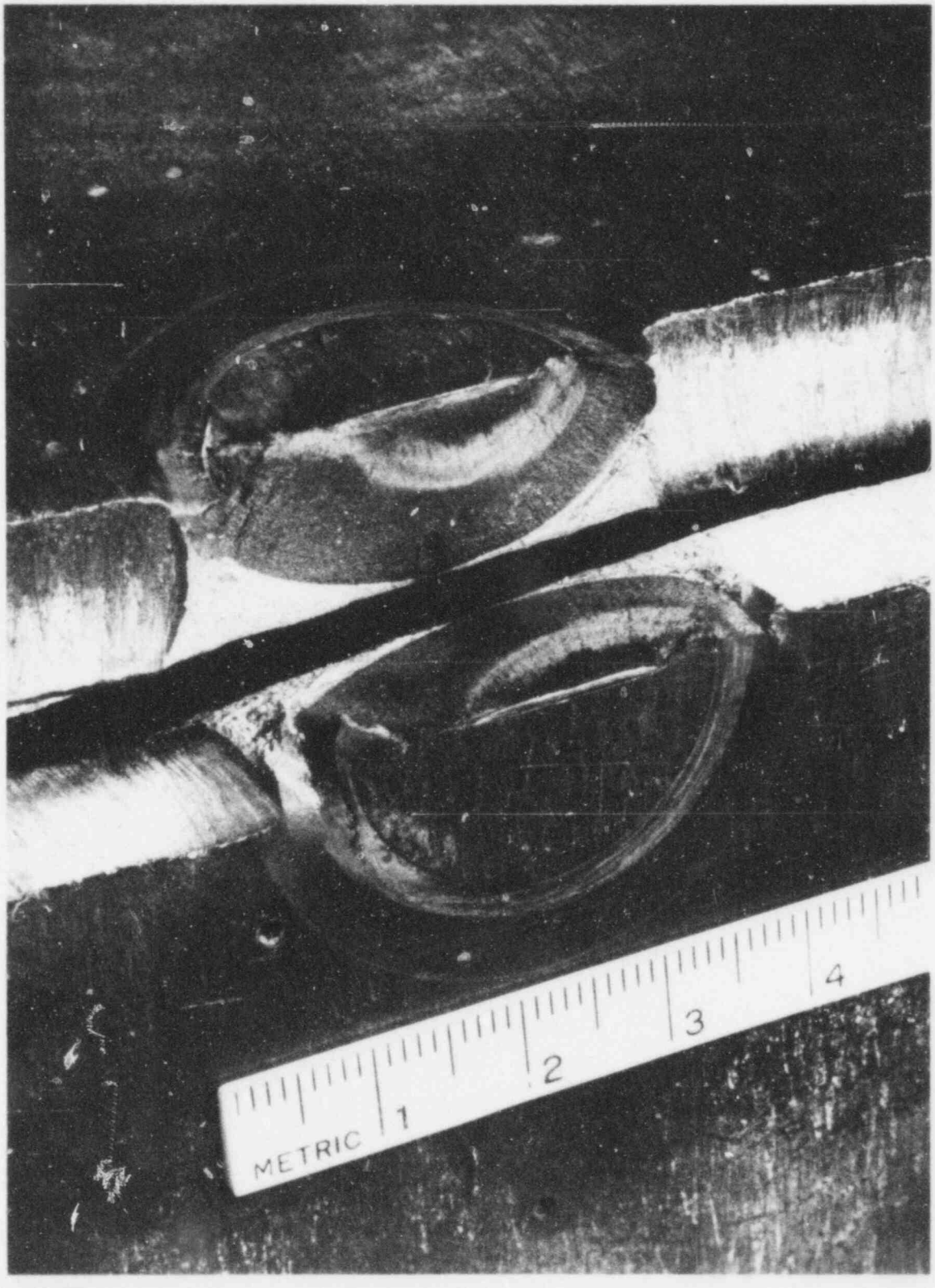

FIGURE 3. Thermal Fatigue Crack in 304 Stainless Steel

A parametric study has been initiated to study the effects of maximum surface temperature and cycle rates on the crack growth rate. The crack growth rate data will be important in determining the total cycles required to produce a crack of a predetermined size. The configuration of the starter notch will also be investigated for its effect on the aspect ratio of the crack. Some preliminary results of the crack growth rate tests for the 0.5-in., 304 stainless steel plate are shown in Figure 4 along with some results obtained from General Electric San Jose for comparison purposes. The crack growth rates for both materials appear to fall into the same general grouping. Note, however, that the cycle rate for the 0.5-in. stainless steel was twice as fast as that for the 2.0-in. carbon steel. Crack initiation appeared to occur within a few thousand cycles. This was an important result because it will increase the reliability of crack size predictions. These initial results were encouraging because crack depths of interest can be produced in a matter of days. For example, a half-through crack (0.25 in.) can be grown in less than 3 days.

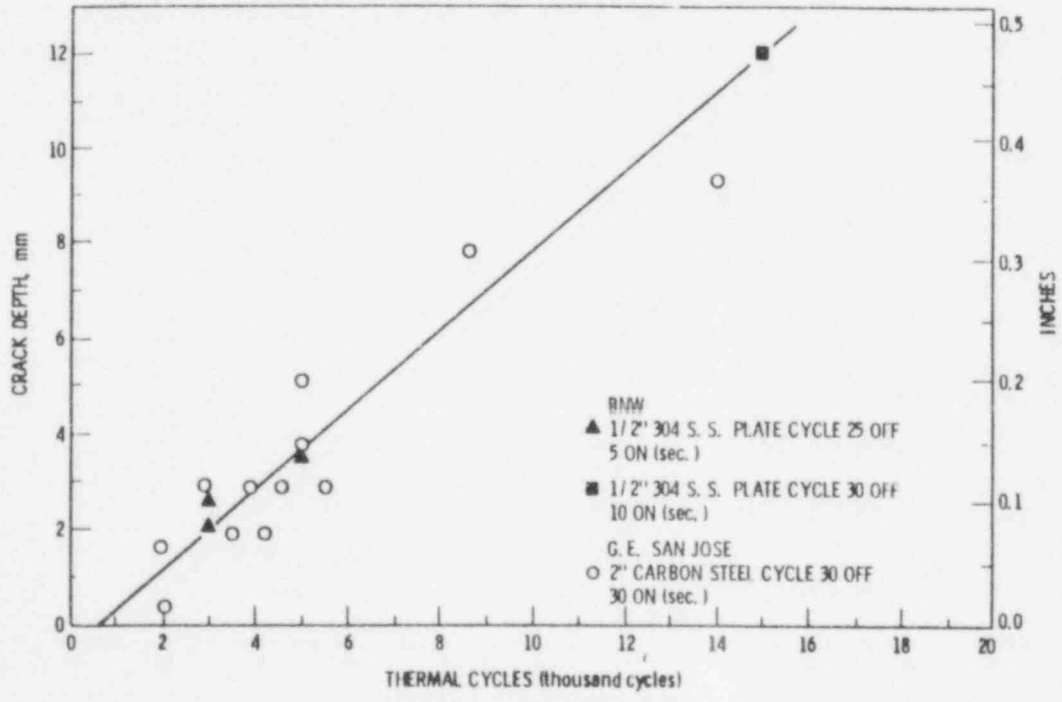

FIGURE 4. Crack Depth Versus Thermal Cycles

Specimen Production

Equipment has been ordered to construct six thermal fatigue stations. The equipment is scheduled to be delivered in early May with operation to begin by June 1. The estimated cost of the facility is $10K for equipment and $6K for installation. It is expected that the 10-in., Schedule 80 pipe fatigue flaws will be completed by mid-July. This is approximately a one-month schedule slippage as we do not expect to receive the centrifugally cast stainless samples before June 1. This will also cause a delay of at least two months. These slippages will result in some schedule delay and a limitation in the quantity of data which can be recorded this fiscal year. However, we still expect that the baseline (initial estimate) of flaw probability of detection can be made this fiscal year.

Flaw Characterization Samples

It is necessary to produce a series of cracks with specific sizes, aspect ratios, and roughnesses for nondestructive examination (NDE) flaw characterization and evaluation. This requires understanding and control of crack initiation and growth rates, and crack-shape changes.

Initial considerations showed that aspect ratio can be controlled by the shape of the initiator and stress distribution. Final crack size can then be estimated using initiation rates, crack-growth rates, and controlled by accurate measurement of crack length. Roughness is thought to be controlled by environment, stress-intensity amplitude and R-ratio.

Calculations of stress intensities required to produce desired crack-growth rates showed that very high loads would be required to produce the cracks in cyclic tension; therefore it was decided to load the specimens in cyclic bending. Cold-rolled material was found to be sufficiently strong to allow application of the desired stress intensities. Two cyclic-bending approaches have evolved; one using a mechanical fatigue machine and one using servohydraulic testing machine. Sketches of the fixtures are shown in Figures 5 and 6.

A matrix on the crack sizes, aspect ratios, and roughness is given in Table 1. The remainder of the section will describe methods which will be used to produce this matrix, and will summarize the results to date.

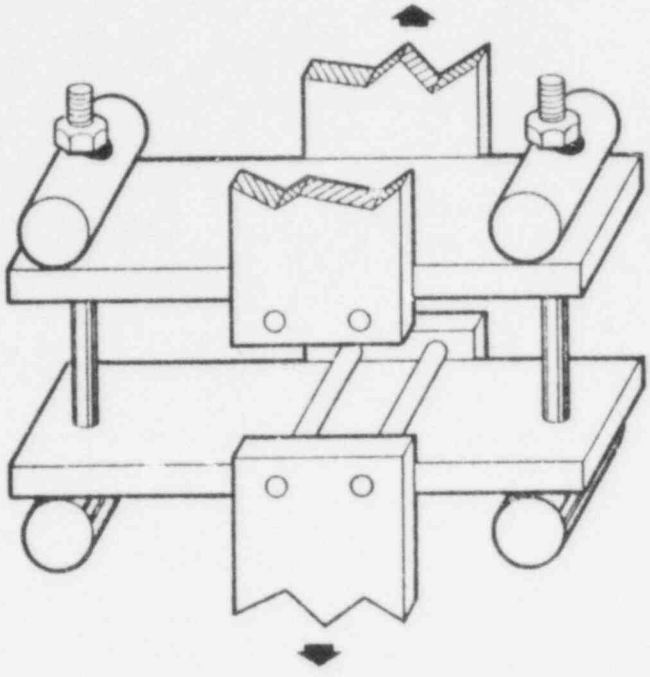

FIGURE 5. Fixture Used to Hold Specimens in Mechanical Cycling Test Machine. Load is applied at the center-support plates, producing four-point bending.

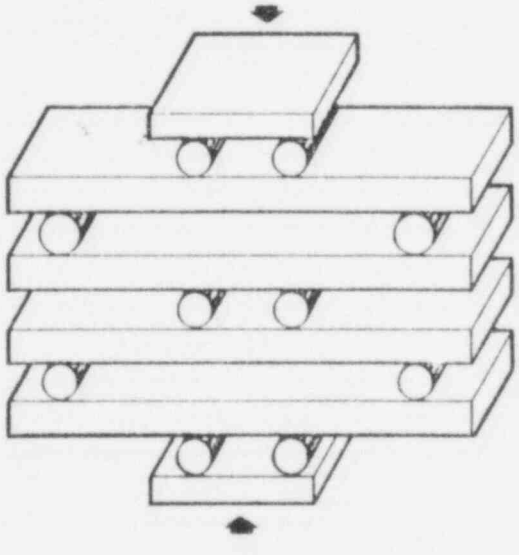

FIGURE 6. Fixture Used to Support Specimens in Hydraulic Testing Machine. Size of specimen stack can be increased as desired. Uniform four-point bending is produced.

TABLE 1. Specimen Matrix for Flaw Characteristics Experiment

Roughness	Aspect Ratio	Depth
rough	10	10%
rough	10	10%
rough	10	20%
rough	10	20%
rought	10	50%
rough	10	50%
rough	4	10%
rough	4	10%
rough	4	20%
rough	4	20%
rough	4	50%
rough	4	50%
smooth	10	10%
smooth	10	10%
smooth	10	20%
smooth	10	20%
smocth	10	50%
smooth	10	50%
smooth	4	10%
smooth	4	10%
smooth	4	20%
smooth	4	20%
smooth	4	50%
smooth	4	50%

Crack Initiation

The requirements of crack initiators in this study are:
locate the crack at the desired position
influence the shape of the crack
reduce the required stress level
not influence NDE signals and
be relatively reproducible.

Chemical and mechanical crack initiators were considered. Chemical (crevice corrosion, stress-corrosion cracking) methods lacked reproducibility and shape control; however, they had the advantage of having less influence on NDE signals. Mechanical (sawcut, drilled holes, abrasive-wheel, and electron-discharge machining) methods are more controllable and reproducible, but produce NDE interference. This problem was solved by producing the cracks in over-thickness plate and removing the stress concentrator by machining after some crack growth. One benefit of this method is additional crack-shape control obtained by cycling after removal of the stress concentrator.

Preliminary work has shown that abrasive-wheel cuts are satisfactory for long-aspect-ratio cracks, and drilled holes are suitable for short-aspect-ratio cracks. The drilled hole starter consists of three overlapping 1/16 in. diameter holes drilled 0.1 in deep. Initiation appears to occur evenly across abrasive-wheel cuts, but cracks emanating from drilled holes appear to initiate first at the end of the hole, then grow around the sides. This helps to produce low aspect-ratio cracks.

Crack Growth

Eight specimens were used to evaluate crack-shape changes during crack-growth. Unlike cyclic tensile loading, cyclic bending produces large changes in crack-shape if crack growth is large.

It is apparent that three stages of crack growth exist. In the first stage, crack-shape remains relatively constant and is determined by the shape of the crack initiator. This stage is typically 0.1 to 0.2 in. for the specimens used in this study. The second stage is a transition stage. Here the initial shape and the stress distribution interact to determine crack-shape.

The third stage of crack-growth is dependent only on the stress distribution. The bending stresses produce crack-growth rates higher at the surface of the specimen. As the net section ligament decreases, the surface stress increases, producing acceleration in surface crack-growth rate relative to through-thickness crack-growth rate. Specimens with drilled holes and abrasive-wheel initiators are shown in Figures 7A and 7B.

Summary

A suitable method has been established for production of cracks with specific aspect ratios, sizes, and roughnesses. Each of the two systems shown in Figures 5 and 6 cycles four specimens simultaneously. With known information concerning crack-initiation levels, crack-growth rates and changes in crack-shape during growth, production of cracks should proceed rapidly. Four low cycle (rough) flaw samples have been fabricated. These four samples required approximately one day to fatigue. It is expected that all flaws in Table 1 will be fabricated by June 15.

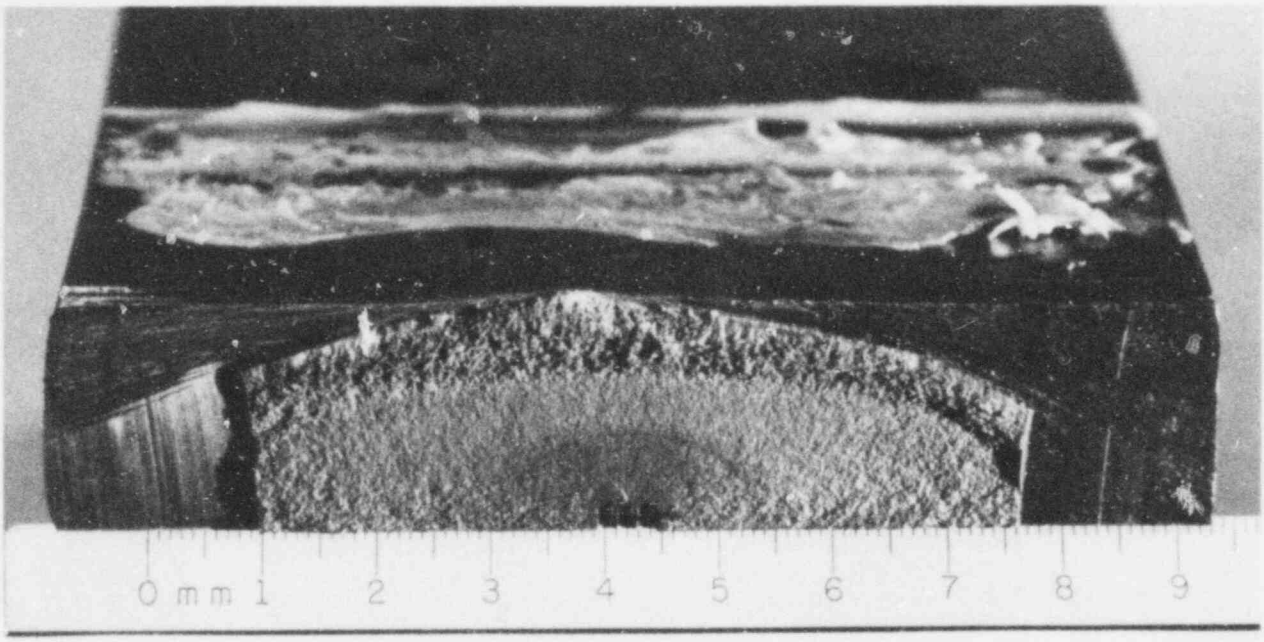

FIGURE 7.A. Photo of Fatigue Surface, Four-Point Bend Specimen. In this case, crack emanates from a drilled hole initiator. This type of notch is used to produce cracks with low aspect ratios.

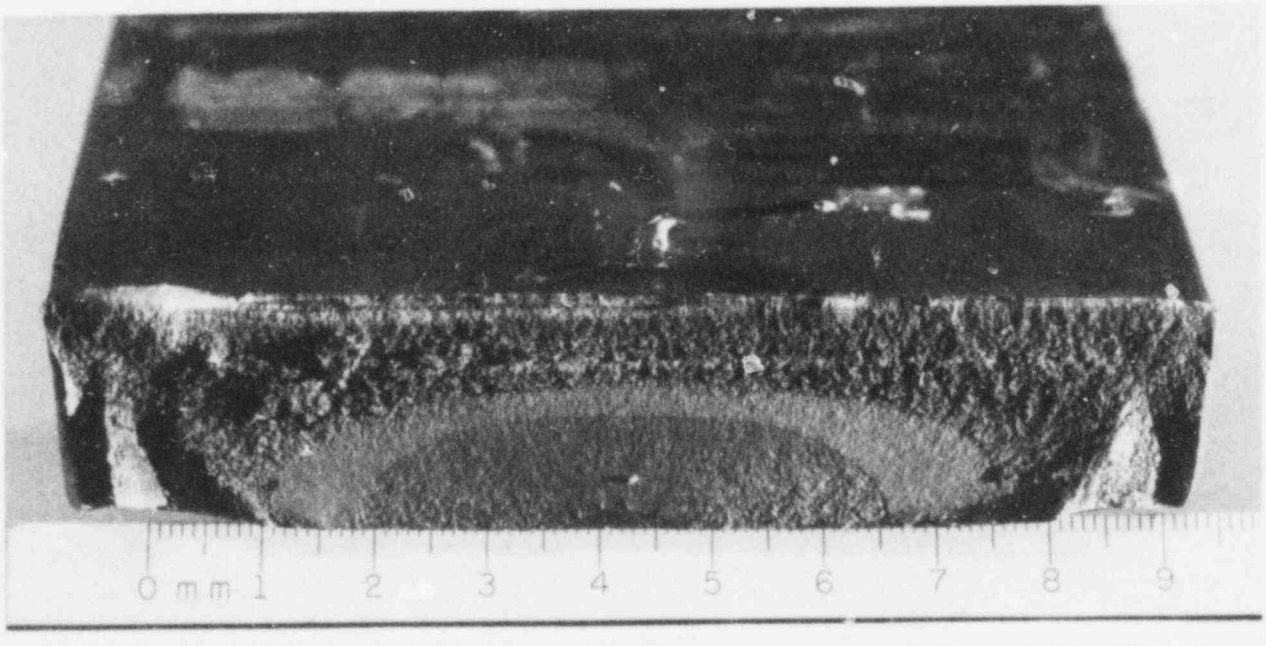

FIGURE 7.B. Photo of Fatigue Surface, Showing Heat Tinted (dark) and Non-Heat Tinted (light) Areas. Heat tinting was used to mark the progress of fatigue--crack growth, so that changes in crack shape during growth could be studied. This crack initiated at an abrasive wheel cut, and is typical of long aspect ratio cracks.

TASK 7: MEASUREMENT AND EVALUATION

Measurement and evaluation activities during the past quarter have been directed toward evaluating the suitability of fatigue cracks which were produced as a part of Task 6. A method was developed for measuring crack depth in the flat plate standards (flaw characteristics samples). A normal beam longitudinal wave is used directly over the crack. Sufficient energy is returned from the crack-tip to identify its depth. Of the ten cracks measured in this manner five were measured to within 0.020 in. of the actual size, as determined by destructive tests. The other five samples produced insufficient reflection from the crack tip for measurement. In these cases the angle beam, 6 db drop technique was used to size the flaws. These two sizing techniques should provide sufficient information to assure that the samples are suitable for the test matrix.

Two ultrasonic instruments have been ordered for this evaluation: Sonic Mark 1 and a Nortec 131D. These instruments were selected based on preliminary results of the state-of-practice survey (Task 2). They represent approximately 60% of the industry in usage. A range of search units (2.25 MHz, with diameters from 0.25 to 1.0 in.) as well as four dual element search units for the various thickness ranges to be inspected have also been purchased.

In addition to the fatigue cracks which will be generated in Task 6, electron-discharge machining (EDM) notch standards are being fabricated for evaluation of geometric variables. The EDM notches cover a range of 0^{o} to 30^{o} for notch orientation and 0^{o} to 20^{o} for counterbore, all at fixed depths and metal path. The notches will also cover a depth range of 0.020 in. (3%) to 0.36 in. (60%) at a fixed 5:1 aspect ratio.

After completion of geometric effects evaluations using notches, selected fatigue cracks will be grown to quantify the differences for real flaws.

FUTURE PLANS

Activities for the next quarter will concentrate on completion of the cracked sample fabrication matrix. Efforts will be made to accelerate shipment of the large diameter pipe samples from Naval Systems Research and Development Center and the crack fabrication process. The measurement and evaluation program will be initiated and will evaluate available samples. The state-of-practice review will be published.

APPENDIX A

ANALYSIS OF THE THERMAL FATIGUE PROCESS FOR CRACKED SPECIMEN PRODUCTION

INTRODUCTION

One of the requirements of the present NRC sponsored program on NDE reliability and fracture mechanics is to prepare cracked specimens. These specimens will be used to evaluate crack detection capabilities of ultrasonic inspection procedures.

It has been proposed to adapt a thermal fatigue method previously used by General Electric (G.E.) to initiate and grow cracks. This method is shown in schematic form in Figure A.1. A plate is heated on the back side to an elevated temperature (e.g., 1100°F), and a local area (1/16 in. diameter) is cooled with water jet on the opposite side of the plate. A 0.75-in. long by 0.02- to 0.04-in. deep notch serves to initiate a crack. The heated plate is quenched for 15 sec followed by a water-off period of 15 sec. G.E. has been able to grow cracks to lengths on the order of 1.0 in. with a few thousand cycles of quenching. The plates have been low carbon or low alloy steel in thicknesses of 2.0 and 6.0 in.

Battelle proposes to apply the G.E. method to somewhat different types of specimens. Wall thicknesses will be as low as 0.594 in., and in some cases a pipe geometry rather than a flat plate will be utilized. In addition, some specimens will be of 304 stainless steel. Metallurgical considerations may dictate the use of preheat temperatures less than the 1100°F level used by G.E.

The study reported here was to determine if the G.E. method can crack the specimens of PNL's program with a reasonable number of thermal fatigue cycles. Approximate stress analyses were performed to predict trends in crack growth rates. The objective was to determine if cracks will grow faster or slower for PNL's conditions as opposed to those within G.E.'s experience.

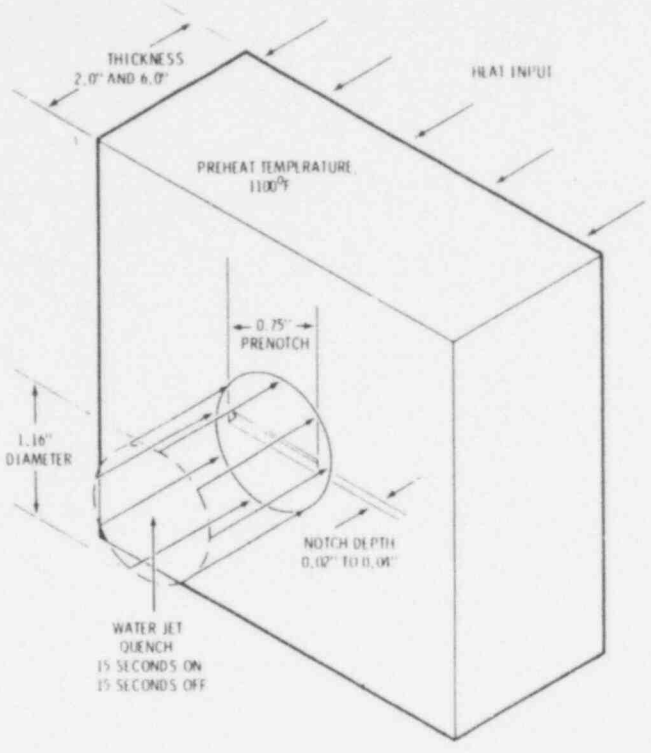

FIGURE A.1. Thermal Fatigue Cracking Specimen

The calculations are intended to guide and complement empirical cracking studies to be performed at Battelle in an experimental facility which will be based on the G.E. design.

Details of the analyses method are first described below. Results and conclusions are presented in the final section under the title of parametric studies.

HEAT TRANSFER

The idealized heat transfer model shown in Figure A.2 permitted trends relative to wall thickness and material thermal properties to be considered. Closed form solutions for transient heat conduction could be utilized since the heat transfer was purely one dimensional (i.e., through the thickness of the plate).

The analysis considered only the first thermal shock, when the initially hot plate was cooled locally by the water jet. Subsequent reheating once the jet was turned off and the eventual periodic temperature variation was not considered. Also inherent to the one-dimensional analysis was the neglect of heat flow parallel to the plane of the plate. It is believed, nevertheless, that the selected representation of the thermal shock conditions provided a sound basis for establishing comparative stress levels.

Available data indicate that the area of hot metal surface exposed to the water jet will cool to temperature at or below 200°F in less than one second. Accordingly the surface was taken to be cooled instantaneously. Data on quenching rates in heat treating (initial temperatures in excess of 1600°F) as discussed in the Metals Handbook (Taylor 1964) show this rapid surface cooling. Recent calculations at PNL (Simonen, Thurgood, and Griffiths 1978) of rapid cooling of heated waste canisters (initial temperatures in the range of 700°F) also show this trend. The latter calculations were based on boiling phenomena and surface heat transfer coefficients reported by Chen (1963).

Heat transfer references (Rohsenow and Hartnett; Carslaw and Jaeger 1959) give closed-form solutions for a slab of finite or infinite thickness for a step change in surface temperature with the initial temperature being uniform. For the thick-slab case,

$$\frac{T-T_o}{T_w-T_o} = \text{erfc}(x/2\sqrt{\kappa t}),$$

where

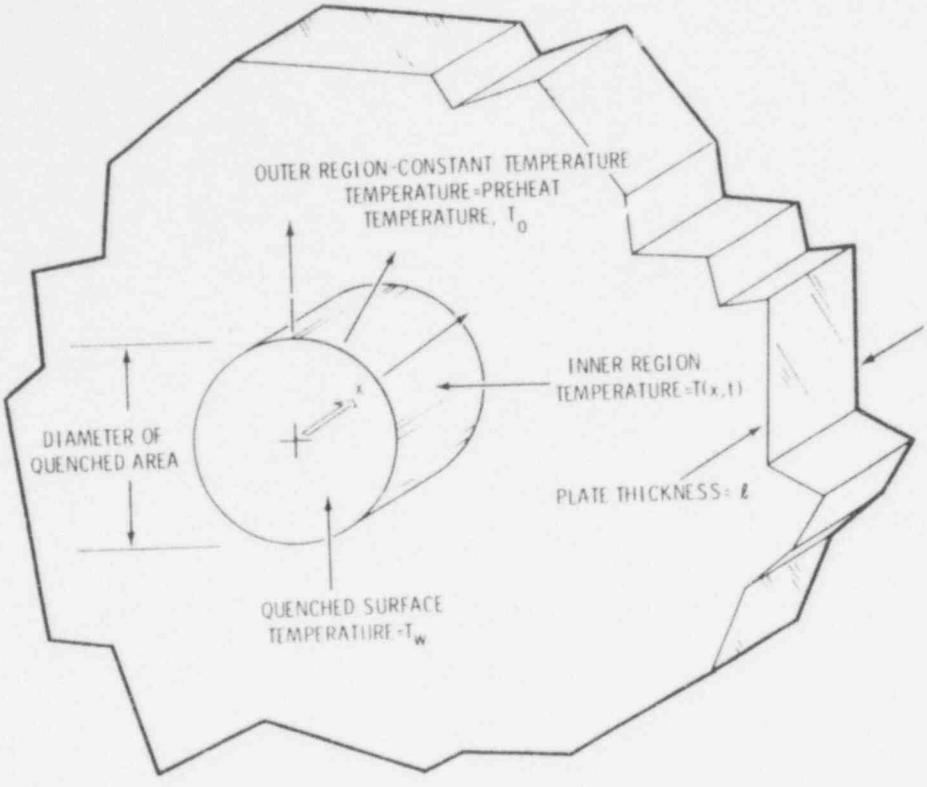

FIGURE A.2. Model for Heat Transfer Analyses--One Dimensional Idealization

$T = T(x,t)$ = temperature, ^oF

T_o = initial uniform temperature, ^oF

T_w = cooled temperature of quenched surface, ^oF

erfc = complimentary error function

x = depth below surface, in.

κ = thermal diffusivity, $in.^2/sec$

t = time, seconds.

This solution gives accurate results for the finite thickness slab for times soon after the quench, but does not account for back-side effects which develop after longer times.

A series solution which converges slowly for small values of time, but includes back surface effects is given by Carslaw and Jaeger (1959) as follows:

$$\frac{T-T_o}{T_w-T_o} = (4/\pi) \sum_{n=o}^{\infty} \frac{1}{(2n+1)} e^{-\kappa(2n+1)^2\pi^2 t/\ell^2} \mathrm{Sin}(2n+1)\pi x/\ell$$

where is the wall thickness. The back surface is assumed to be insulated, which neglects the transfer of heat into the plate over the small time period of the quench.

The above solutions for cooling for the initial quench will tend to overestimate the severity of quenching under conditions of repeated quenching. After a number of quenches, locations in the cooled zone will attain some mean temperature below the remote temperature T_o. Thus, the effective value of initial temperature will be somewhere between T_o and T_w.

STRESS ANALYSIS

The stress analysis was based on the elasticity theory solution for a circular disc in a hole in a plate as indicated in Figure A.3. It is implied that each mathematical layer of the plate acts independently of the others. That is, shear stresses between layers do not restrain adjacent layers. This approach will tend to underestimate stresses perhaps by a factor as high as two. On the other hand, the heat transfer solution by not considering effects of repeated quenching may overestimate the thermal loads by a comparable factor of two.

As shown in Figure A.3, the quenched circular disc region experiences a thermal contraction strain of

$$\varepsilon_{thermal} = \alpha(T-T_o)$$

α = thermal expansion coefficient, in/in/^oF

relative to the surrounding region that remains at T_o. To accomodate the differential thermal strain, mechanical strains in the disc and surrounding plate must satisfy the condition

$$\varepsilon_{plate} - \varepsilon_{disc} = -\varepsilon_{thermal}$$

where

$$\varepsilon_{disc} = -(p/E)(1-\nu)$$

$$\varepsilon_{plate} = +(p/E)(1+\nu)$$

p = radial pressure at interface

E = elastic modulus

ν = Poisson's Ratio

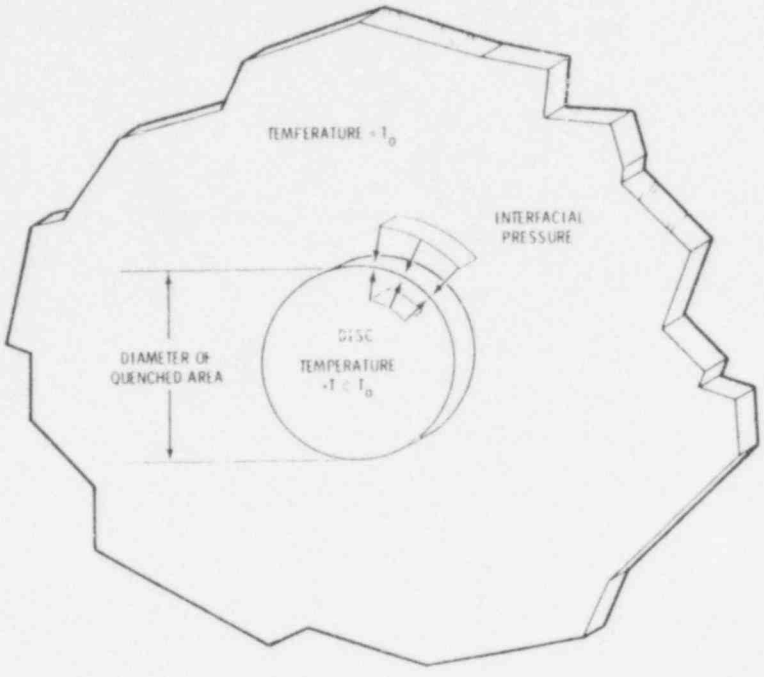

FIGURE A.3. Model for Stress Analysis--Thermal Contraction of Disc in Hole

The stress within the quenched region is given by

$$\sigma = \sigma(x,t) = -p = 1/2\ E\alpha\ (T-T_o).$$

This stress was used as an input to estimate stress intensity factors for cracks of various depths.

CRACK TIP STRESS INTENSITY

Stress intensity factors corresponding to the thermal stress distributions were computed using the idealization shown in Figure A.4. Stresses from the uncracked thermal stress solution were applied as loadings on the faces of an edge crack. The edge crack solution reasonably represents the cracked specimen geometry for short cracks. However, for deeper cracks, the effects of crack aspect ratio is lost (e.g., an elliptical surface crack). This edge crack simplification is believed to be consistent with the types of approximations made in other aspects of the analysis.

In reference to Figure A.4, the crack face stresses was approximated as a set of point loads. Using a solution reported in Tada(1973), the stress intensity factor K_I was computed as

$$K_I = \frac{2}{\pi a} \sum_{i=1}^{N} P_i \, F(b_i/a) \sqrt{1-(b_i/a)^2},$$

where a, b and P are defined in Figure A.4. And $F(b_i/a)$ is a function defined in Tada (1973) which varies from 1.0 for b/a = 1.0 to 1.3 for b/a = 0.

The above procedure for stress intensity evaluation along with the necessary heat transfer and stress equations were programmed for computer calculations, and parametric studies were preformed.

Input parameters to the program included:

- plate thickness
- specimen preheat temperature
- temperature of cooled surface
- material properties - elastic modules, expansion coefficient and thermal diffusivity
- cooling times of interest
- crack lengths of interest

As output the program provides

- temperatures and stresses as function of position and time
- stress intensity factors as a function of crack length and time.

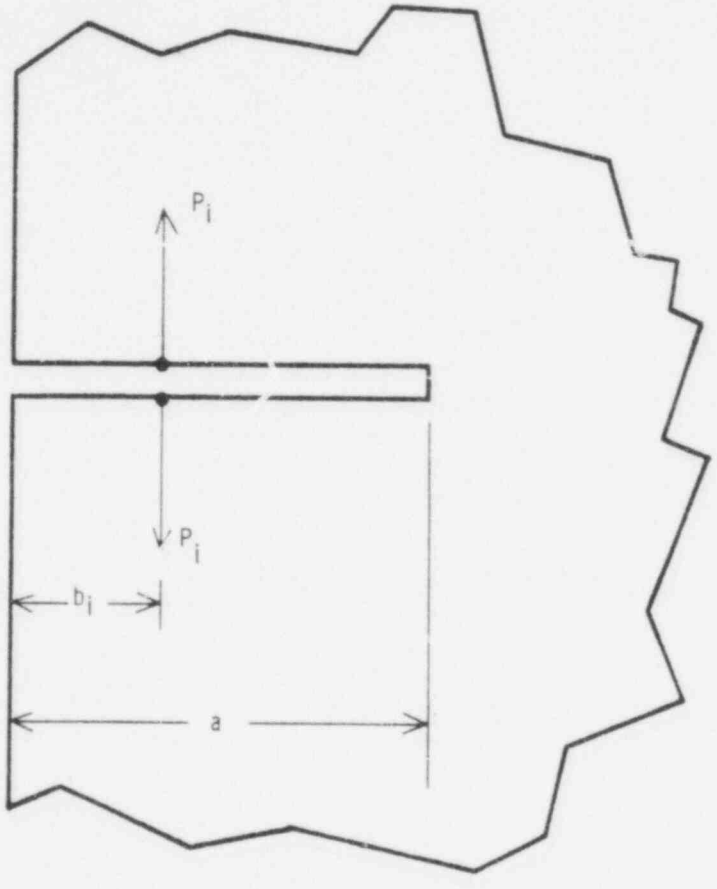

FIGURE A.4 Model for Calculating Stress Intensity Factors

PARAMETRIC STUDIES

The following parameters were selected for study:

- plate thickness - 6.0, 2.0 and 0.594 in.
- crack depth - 0.05, 0.10, 0.20, 0.50, 1.0, 2.0, and 4.0 in.
- materials - carbon steel and austenitic stainless steel with properties as given in the ASME Code
- preheat temperature - 1100^{o} and 650^{o}F
- cooled surface temperature - 200^{o}F
- cooling time - 1, 2, 5, 10, 15, 30 and 60 sec.

Variations in material properties with temperature were taken into account by selection of properties midway between T_o (650^{o} and 1100^{o}F) and T_w (200^{o}F). These values are given in Table A.1.

TABLE A-1 Thermal and Mechanical Properties from ASME Code

		Thermal Expansion Coefficient, in./in./^{o}F	Elastic Modulus, lb/in.^{2}	Thermal Diffusivity, in.^{2}/sec
Carbon steel	425^{o}F	7.61×10^{-6}	26.8×10^{6}	0.0263
	650^{o}F	8.54×10^{-6}	25.2×10^{6}	0.0167
Austenitic stainless				
	425^{o}F	9.99×10^{-6}	26.5×10^{6}	0.0065
	650^{o}F	10.45×10^{-6}	25.6×10^{6}	0.0069

Stress intensities were calculated based on linear elastic fracture mechanics, although nominal stresses exceeded yield for the imposed thermal shock conditions. Also the various approximations in the analyses suggest that the calculated stress intensity factors may be accurate only within a factor of two. The results do, however, serve the objectives of the study by showing trends as a function of specimen and test parameters. More exact calculations would be feasible using finite element methods, but such methods were inconsistent with cost and schedule constraints of the present program.

EFFECT OF PLATE THICKNESS

Figure A.5 shows stress intensities factors for plate thicknesses of 6.0, 2.0, and 0.594 in. Within the approximations of the present analysis, no difference between the 2.0- and 6.0-in. thick plate were predicted. The thinner 0.594-in. plate showed slightly higher stress intensity factors, particularly for deeper cracks and longer cooling times.

The 0.594 in. thickness corresponds to a pipe wall thickness of one proposed specimen. For the thermal fatigue conditions of interest it is believed that differences due to curvature between a pipe wall and a flat plate are of secondary importance.

Experience at G.E. has shown greater crack growth rates in 2.0-in. plates compared to 6.0-in. thick plates. These differences may be in part due to differences in the materials for the two plate thickness. Nevertheless there could be a thickness effect not fully accounted for due to approximations in the present analyses. Particularly, the heat transfer model was only one dimensional and considered only the initial thermal shock. It is thought that the thicker plate acts as a better heat sink and more effectively reheats the quenched zone between water quenches. Thus under repeated quenching the thicker plates probably have a higher effective temperature at the beginning of each quench.

EFFECT OF COOLING TIME

Figure A.5 shows that crack tip stress intensity factors increase as the quench duration increases. For the slower growing cracks of smaller depth, the stress intensity levels essentially saturate in the 15-sec quench of the G.E. test procedures. The calculated trends suggest that a shorter quench, say 5 sec, may be adequate. In fact, short quenches at greater frequency may actually decrease the hours of test time to grow a crack of a given size.

EFFECT OF PREHEAT TEMPERATURE T_o

Figure A.6 shows that crack tip stress intensity factors are strongly dependent on preheat temperature. The dependence is essentially directly in

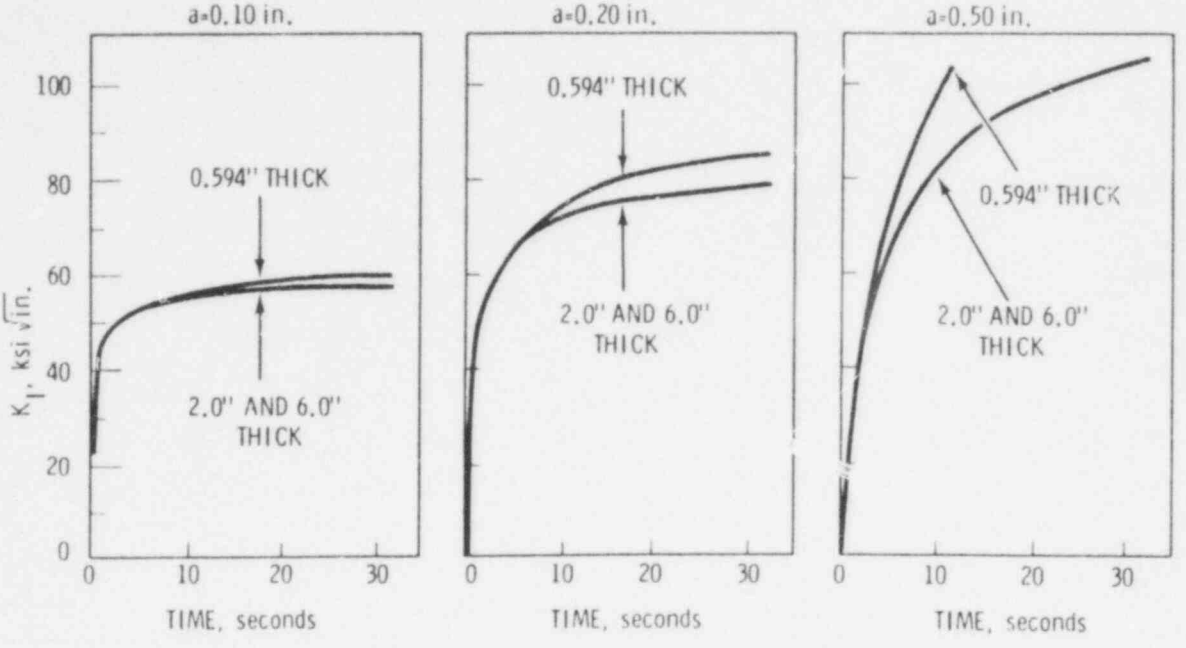

FIGURE A.5. Effect of Thickness on Performance of Thermal Fatigue Cracking Specimen

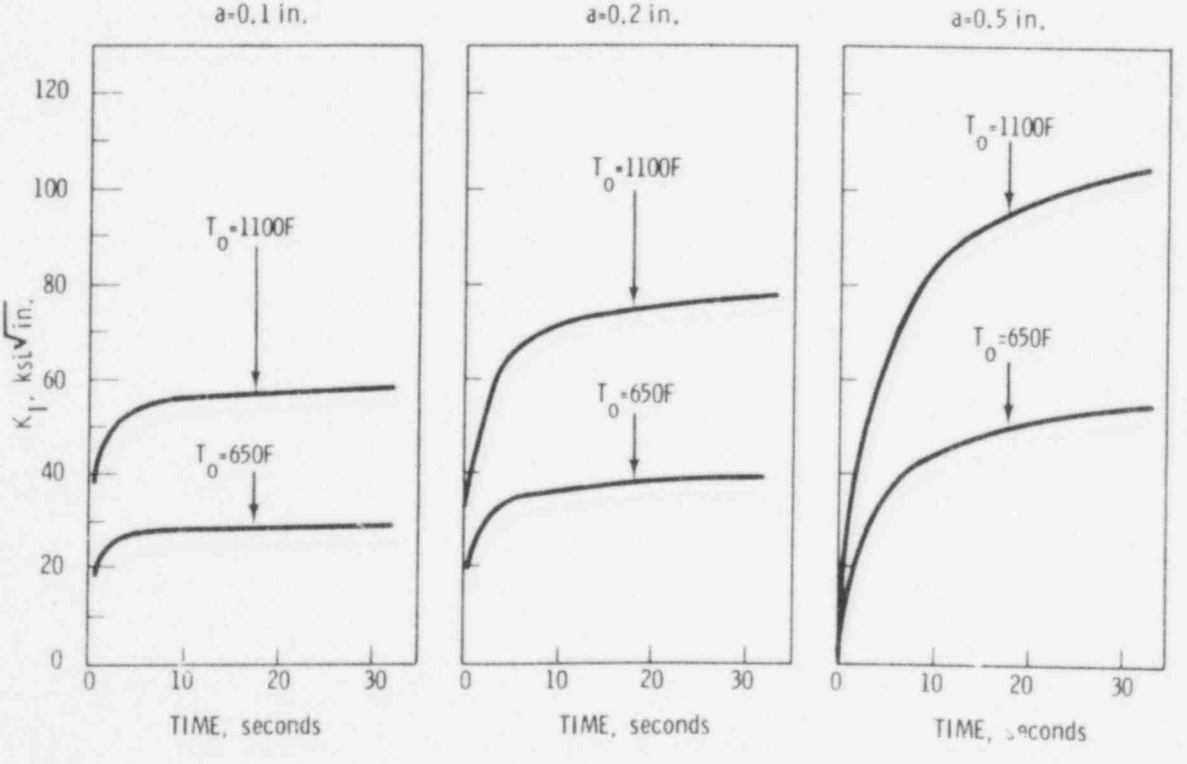

FIGURE A.6. Effect of Preheat Temperature on Performance of Thermal Fatigue Cracking Specimen

proportion to the difference between the preheat and cooled temperature of the quenched surface (200°F in these calculations). Crack growth rates, being logarithmic functions of stress intensity factor, will decrease dramatically with reductions in preheat temperature T_o. Therefore, if cracked specimens are to be produced within a minimum of test time, the preheat temperature must be maintained at maximum practical levels.

EFFECT OF MATERIAL

Figure A.7 compares stress intensity factors for low-carbon (or low-alloy) steel with those for an austenitic stainless steel such as 304. For a given plate thickness and quench, the stress intensity for the stainless alloys are somewhat higher than those for the low carbon type steels. This is due primarily to the higher thermal expansion coefficient of the stainless steel. However, the stainless steels have lower thermal conductivities, and Figure A.7 shows a slower increase of stress intensity factor with time for the stainless steel. Fatigue crack growth rate data should first be located before drawing any conclusions on the ability of the thermal shock procedure to produce cracked specimens of stainless alloys. If low carbon steels and stainless steels have identical crack growth rate properties, then this study indicates that stainless specimens will be easier to crack.

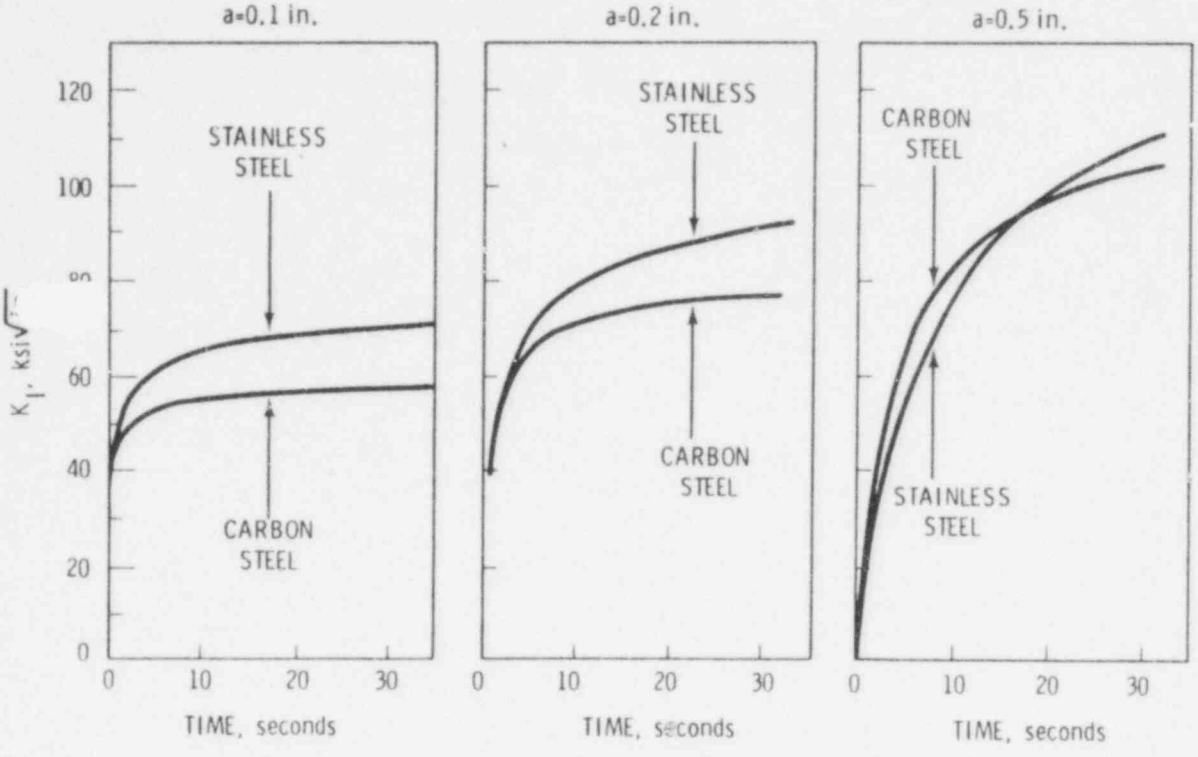

FIGURE A.7. Effect of Specimen Material on Thermal Fatigue Cracking--Low Carbon Versus Austenitic Stainless Steel

REFERENCES

1. Taylor, Lyman, ed. 1964. Metals Handbook 8th Edition - Vol. 2 Heat Treating, Cleaning, and Finishing. American Society for Metals, Metals Park, Ohio.

2. Simonen, F. A., M. V. Thurgood. and J. A. Griffiths. 1978. "Analysis of a Canister Closure Design by Damage Tolerance Concepts." ASME Paper No. 78-PVP-108, presented at the ASME 1978 Pressure Vessels and Piping Conference, Montreal, Quebec, Canada.

3. Chen, J. C. 1963. "A Correlation for Boiling Heat Transfer to Saturated Fluids in Convective Flow." ASME Paper No. 63-HT-34, American Society of Mechanical Engineers.

4. Rohsenow, S. M. and J. P. Hartnett. Handbook of Heat Transfer, McGraw-Hill, New York.

5. Carslaw, H. S., and J. C. Jaerger. 1959. Conduction of Heat in Solids. Second Edition, Oxford, England.

6. Tada, H. 1973. The Stress Analysis of Cracks Handbook, Del Research Corp., Hellertown, Pennsylvania.

APPENDIX B

AN EVENT-TREE APPROACH FOR PROBABILITY FOR DETECTION EVALUATION

For an inspection team to arrive at the correct conclusion regarding a cracked specimen, it must complete a series of well-defined steps. Recording the outcome of each of these steps may give us useful information concerning the weaknesses of the ultrasonic testing system. It should also be possible to use these extra data to better describe the relationship that probability of detection has with other variables. The event-tree description should be particularly relevant to inspection carried out under field conditions because it should allow us to keep track of events that might occur quite frequently under these circumstances. Consequently, the following comments are much more applicable to the Phase 2 round-robins than the Phase 1 experiments.

The following operations must be performed by the inspection team, if it is to find a crack:

(1) Event E_1 - The instrument must be correctly calibrated.[a]

(2) Event E_2 - The scanning beam must hit the crack at a reflectable angle.

(3) Event E_3 - The reflected beam must have an amplitude above the reportable level.

(4) Event E_4 - The team must categorize the reportable indication as a crack.

The relationship between the four events listed above and the event of primary interest can be described by an event-tree:

(a) "Calibrated" here refers not only to sensitivity adjustment, but also the capability of the system and procedure to detect the required reflectors.

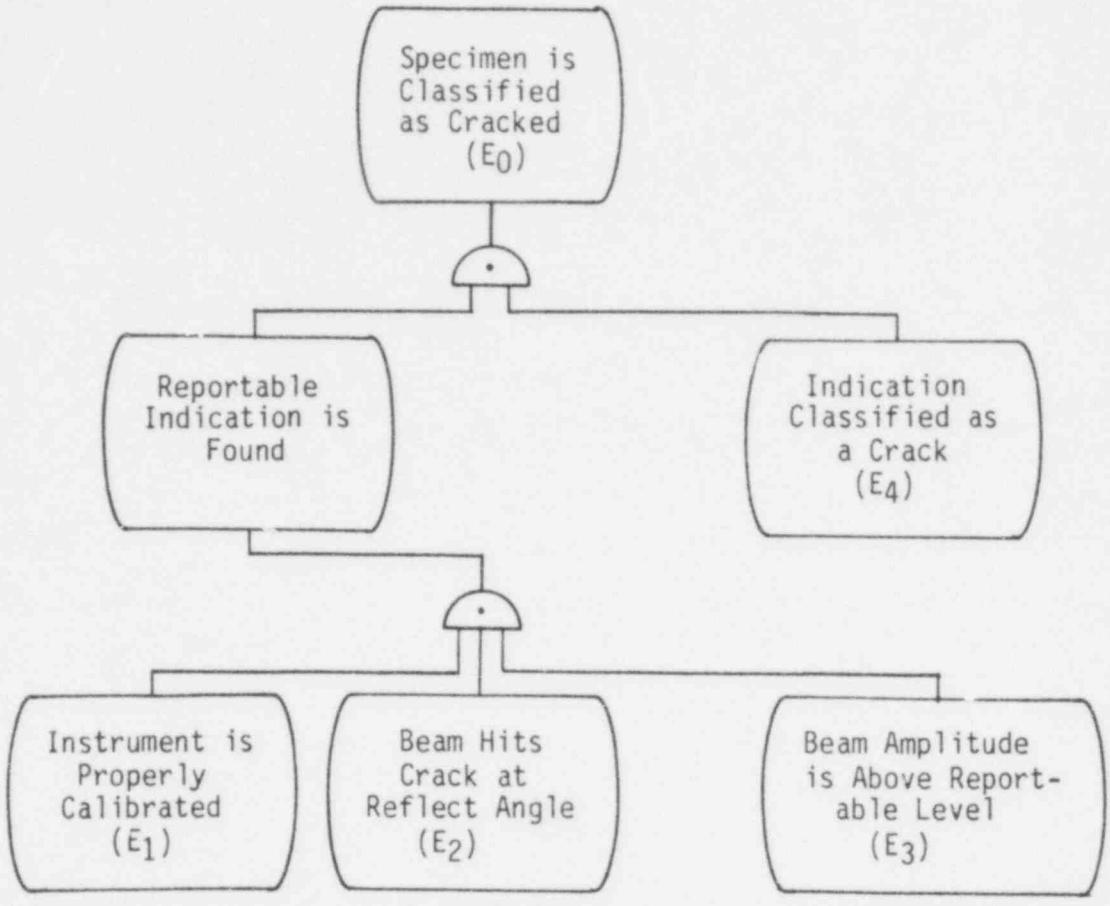

The probability that E_0 occurs is related to the other probabilities of occurrence by the formula:

$$P_0 = P_1 P_2 P_3 P_4 \qquad (1)$$

where

$P_0 = P(E_0)$ = Probability of classifying specimen as cracked.

$P_1 = P(E_1)$ = Probability of properly calibrating the instrument.

$P_2 = P(E_2/E_2.E_1)$ = Probability of hitting the crack at a reflectable angle (assuming all previous steps in the inspection have been correctly performed).

$P_3 = P(E_3/E_2.E_1)$ = Probability of obtaining a reflected signal above the reportable level (assuming all previous steps in the inspection have been correctly performed).

$P_4 = P(E_4/E_3.E_2.E_1)$ = Probability that a reportable indication is classified as a crack (assuming all previous steps in the inspection have been correctly performed).

An experiment concerned with the measurement of probability of detection (P_0) will select several different sets of conditions (treatments) under which this probability is to be measured. Each treatment can be represented by an nth multiple that lists the independent variable settings (factor levels) in the treatment. For example, an experiment might consider the factors: flaw depth, ID geometry, viewing position, inspection team.

Each different treatment that would occur in the experiment could be described by the 4 multiple;

$$I = (i_1, i_2, i_3, i_4)$$

where

i_1 = level at which flaw depth is set (10%, 25%, etc.)

i_2 = level at which ID geometry is set (optimum counterbore, angled counterbore)

i_3 = level at which viewing position is set (near side, far side of weld)

i_4 = number of the inspection team that was used.

Associated with each different treatment 1 is a probability of detection which can be represented by $P_0(I)$. The formula (1) can be used to decompose $P_0(I)$ into:

$$P_0(I) = P_1(I)\ P_2(I)\ P_3(I)\ P_4(I) \tag{2}$$

The direct estimate for $P_0(1)$ is calculated by counting the number of inspections made under treatment 1 that detected the crack and dividing this number by the total number of inspections performed under treatment 1. That is:

$$\hat{P}_0(I) = \frac{\text{number positive inspections performed under treatment 1}}{\text{total number inspections performed under treatment 1}} \tag{3}$$

Formula 2 provides an alternative way of estimating $P_0(I)$. Estimates $P_1(I)...P_4(I)$ can be calculated and these estimates can be combined using formula 2 to obtain an estimate for $P_0(I)$. That is

$$\hat{P}_0(I) = \hat{P}_1(I)\ \hat{P}_2(I)\ \hat{P}_3(I)\ \hat{P}_4(I) \tag{4}$$

(4) has certain advantages over Equation (3), if the functions $P_1(I)...P_4(I)$ happen to be simple. If the functions $P_1(I)...P_4(I)$ do not depend on all the factors in I, Equation (4) will provide a better estimate for $P_0(I)$. (When the functions $P_1(I)\ P_4(I)$ each depend on all the factors in I, the estimates calculated by Equations (3) and (4) will be the same.) For example, it may be reasonable to suppose that:

$P_1(I)$ = $P_1(i_4)$ - P_1 depends only on the inspection team

$P_2(I)$ = $P_2(i_2, i_3, i_4)$ - P_2 depends only on ID geometry, viewing position, inspection team

$P_3(I)$ = $P_3(I)$ - P_3 depends on everything

$P_4(I)$ = team $P_4(i_2, i_4)$ - P_4 depends on ID geometry, inspection.

Both methods of estimating $P_0(I)$ require an experiment with the same basic design, and inspections must be performed under each of the possible treatments. Because of this, one need not choose between these two alternative methods before the experiment is run. The methods can be compared afterwards. The calculation of estimates using Equation (4) does impose an added burden that must be dealt with before the experiment is run, however. Since Equation (4) requires that estimates Of $P_1(I)...P_4(I)$ be calculated, one must plan on collecting data necessary for these calculations. The following results must be recorded for each inspection:

1. Was the instrument properly calibrated?
2. Did the inspection team ever hit the crack at a reflectable angle?
3. Was the reflection above the reportable level?
4. Was the reportable indication classified as a crack?

The results of the experiment can be represented abstractly in the following manner:

let

$$X_j(I,m) = \begin{cases} 1 \text{ if answer to question j was yes for the m'th inspection performed under treatment 1;} \\ 0 \text{ otherwise} \end{cases}$$

N_I = total number of inspections performed under treatment 1

$$X_j(I,+) = \sum_{m=1}^{N} X_j(I,m)$$

Then the direct estimate for $P_0(I)$ is given by

$$\hat{P}_0(I) = \frac{X_4(I,+)}{N_I} \tag{5}$$

And estimates for $P_1(I)...P_4(I)$ (assuming these probabilities depend on all arguments in I) are given by

$$\hat{P}_1(I) = \frac{X_1(I,+)}{N_I} \tag{6}$$

$$\hat{P}_2(I) = \frac{X_2(I,+)}{X_1(I,+)} \tag{7}$$

$$\hat{P}_3(I) = \frac{X_3(I,+)}{X_2(I,+)} \tag{8}$$

$$\hat{P}_4(I) = \frac{X_4(I,+)}{X_3(I,+)} \tag{9}$$

Notice that $\hat{P}_0(I) = \hat{P}_1(I)\ \hat{P}_2(I)\ \hat{P}_3(I)\ \hat{P}_4(I)$. If $P_1(I) = P_1(i_4)$, (P_1 depends only on (i_4) then we can construct the estimate

$$\hat{P}_1(I) = \frac{X_1(+,+,+,I_4,+)}{N(+,+,+,i_4)} \tag{10}$$

And if $P(I) = P(i_2, i_4)$ then we can construct the estimate;

$$\hat{P}_4(I) = \frac{X_4(+,i_2,+,i_4,+)}{X_3(+,i_2,+,i_4,+)} \tag{11}$$

Notice the difference between the estimates calculated in Equations (10) and (6). If one assumes that P_1 depends only on the inspection team, all other factors in the experiment can be ignored during the calculation of $\hat{P}_1$. Equation (10) provides an estimate for $\hat{P}_1(i_4)$ for each different inspection team by counting the total number of times the team performed a correct instrument calibration and dividing it by the total number of calibrations that the team performed. Equation 10 pools many more observations together than Equation 6 and, if such pooling is justified, the estimates calculated from Equation (10) will be more precise than those of Equation (6).

Miscellaneous Comments Concerning Procedure

- The estimates $\hat{P}_1(I)...\hat{P}_4(I)$ are of interest in their own right, not merely because of any role they would play in the calculation of $\hat{P}_0(I)$.
- Most experiments that evaluate probability of detection have a repeated-measures structure. In order to limit expenses, the same cracked specimens are measured repeatedly. This introduces correlations in the measurements that are difficult to deal with. These problems have not been confronted here.
- The strategy that is being considered for the Phase 1 experiments, that of characterizing oscilloscope response and then using the log-normal distribution to calculate probability of detection, is much different in spirit than the approach outlined above. If the event-tree approach were reasonable, one would not expect the log-normal model to adequately describe probability of detection. The log-normal model may adequately describe $P_3(I)$ (probability a beam reflected from the crack is above the reportable level); that is, it may be reasonable to assume

$$P_3(I) = \int_{\ln(c)}^{\infty} \frac{1}{\sqrt{2\pi}\sigma} e^{-\frac{1}{2}\left(\frac{r-\mu(I)}{\sigma}\right)^2} dr$$

where

r = response measured in log (% DAC)

$\mu(I)$ = mean response under Treatment 1 measured in log (% DAC).

- Using the event-tree approach probably will not favorably affect the sample size requirements. An event-tree approach would require about 10 to 30 observations on each treatment. This contrasts with the log-normal approach, which, if appropriate, would not require as many observations.

791202

NUREG/CR-0855
PNL-3040-1
R 1,3,4,5

DISTRIBUTION

No. of Copies

OFFSITE

A. A. Churm
DOE Chicago Patent Group
9800 S. Cass Avenue
Argonne, IL 60439

457 Basic Distribution Under NRC 1, 3, 4 & 5

2 DOE Technical Information Center

25 National Technical Information Center

17 Reactor Safety Research Division
Nuclear Regulatory Commission
Washington, DC 20555

R. F. Abbey, Jr.
S. Fabric
D. A. Hoatson
W. V. Johnston
J. Muscara (10)
R. D. Schamberger
H. H. Scott
R. Van Houton

M. A. Wolf
Department of Atmospheric Sciences
Oregon State University
Corvallis, OR 97330

No. of Copies

2 Electric Power Research Institute
3212 Hillview Avenue
P.O. Box 10412
Palo Alto, CA 94304

L. Agee
B. R. Sehgal

F. Shakir
Department of Metallurgy
Association of American Railroads
3140 S. Federal
Chicago, IL 60616

SM-ALC/MMET
Attn: Capt. John Rodgers
McClellan AFB, CA 95652

Dr. Sotirios, J. Vahaviolos
Western Electric, ERC
P.O. Box 900
Princeton, NJ 08540

Mr. Jerry Whittaker
Union Carbide Company
Oak Ridge National Laboratories
Y-12
Oak Ridge, TN 37830

Mr. L. J. Anderson, B2402
Dow Chemical Company
Texas Division
P.O. Drawer K
Freeport, TX 77541

791203

No. of
Copies

Mr. M. C. Jon
Western Electric, ERC
P.O. Box 900
Princeton, NJ 08540

P. Caussin
Vincotte
1640 Rhode-Saint-Genese
Belgium

ACE Sinclair
Research Division
Berkeley Nuclear Laboratories
Berkeley
Gloucestershire, GL 13 9 PB
U. K.

143 U. S. Acoustic Emission Working Group Membership - list attached

Don Birchon
Admiralty Materials Laboratory
Holton Health Poole
Dorser, England
020-122-2711

W. L. Pearl
Nuclear WAter & Waste Technology
P.O. Box 6406
San Jose, CA 95150

ONSITE

DOE Richland Operations Office

H. E. Ransom

50 Pacific Northwest Laboratory

J. M. Alzheimer
M. C. Bamptom
F. L. Becker
T. D. Chikalla
R. A. Clark
E. L. Courtright
J. M. Cuta
J. F. Dawson

No. of
Copies

Pacific Northwest Laboratory
(Contd)

R. L. Dillon
J. E. Garnier
R. K. Hadlock
C. R. Hann (3)
A. J. Haverfield
J. L. Hooper
T. W. Horst
P. H. Hutton (3)
J. M. Kelly
R. J. Kurtz
P. T. Landsiedel
D. D. Lanning
R. P. Marshall
C. L. Mohr
W. C. Morgan
C. J. Morris
R. D. Nelson
P. W. Nicola
T. W. Patten
L. T. Pedersen
G. J. Posakony
E. B. Schwenk (2)
C. L. Simpson
J. R. Skorpik
A. M. Sutey
S. J. Thompson
M. J. Thurgood
G. L. Tingey
D. S. Trent (3)
C. L. Wheeler
Technical Information (3)
Publishing Coordination (2)
ME

791204